UNIVERSITY OF CALIFORNIA,
IRVINE

Projecting the evolution of Totten Glacier, East Antarctica, over the 21st century using ice-ocean coupled models

DISSERTATION

submitted in partial satisfaction of the requirements
for the degree of

DOCTOR OF PHILOSOPHY

in Earth System Science

by

Tyler Pelle

Dissertation Committee:
Associate Professor Mathieu Morlighem, Chair
Professor Eric Rignot
Professor Francois Primeau

2021

DEDICATION

I dedicate this dissertation to my family, to which I am forever indebted for the endless love, care, and support they have given me throughout my life.

TABLE OF CONTENTS

LIST OF FIGURES

LIST OF TABLES

ACKNOWLEDGMENTS

First and foremost, I would like to thank my gracious advisor, Dr. Mathieu Morlighem. I joined Mathieu's research group in 2016 with no experience in ice sheet modeling. Mathieu was patient with me throughout the learning process, guided my research, and opened many doors that allowed me to flourish and come into my own as a graduate student researcher.

In addition, the research presented in this dissertation would not have been possible if it were not for the help of my wonderful coauthors. I would like to thank Dr. Johannes Bondzio, Dr. Felicity S. McCormack, Dr. Yoshihiro Nakayama, and Dr. Helene Seroussi for their contributions to the research presented in this dissertation. I would also like to thank Dr. Eric Rignot and Dr. Francois Primeau, who served on my Ph.D. committee and provided me with invaluable advice throughout the later stages of my graduate studies. Lastly, I would like to show my appreciation for my research group members, Dr. Youngmin Choi, Dr. Thiago Dias dos Santos, and Shivani Ehrenfeucht as well as the rest of the cryosphere group at UCI for their constructive advice throughout the Ph.D. process.

In addition, without the support of my loving friends and family, none of this work would have been possible. I am eternally grateful for the unwavering support they have given me over not only the last five years, but through my entire life.

I would like to acknowledge the World Climate Research Programme, which, through its Working Group on Coupled Modelling, coordinated and promoted CMIP5 and CMIP6. I thank the climate modeling groups for producing and making available their model output (used in chapter 3), the Earth System Grid Federation (ESGF) for archiving the CMIP data and providing access, the University at Buffalo for ISMIP6 data distribution and upload, and the multiple funding agencies who support CMIP5, CMIP6, and ESGF. I also would like to thank the ISMIP6 steering committee, the ISMIP6 model selection group, and the ISMIP6 dataset preparation group for their continuous engagement in defining ISMIP6. In addition, we would like to acknowledge the NASA Advanced Supercomputing (NAS) Division at the Ames Research Center, who provided the high-end computing resources needed to run our ice flow models.

This work was performed at the University of California, Irvine under a contract with the U.S. National Science Foundation (NSF), U.K. Natural Environment Research Council's (NERC) PROPHET program (#1739031), and under a contract with the National Aeronautics and Space Administration, Cryospheric Sciences Program (#NNX15AD55G).

Portions of chapter 2 are reprinted from a publication in *The-Cryosphere* with permission from Copernicus Publications and all coauthors. Chapter 3 is reprinted from a publication in *Geophysical Research Letters* with permission from John Wiley and Sons. Lastly, chapter 4 has been submitted to *Geophysical Research Letters* and is currently pending publication.

VITA

Education

University of California, Irvine — Irvine, CA
Ph.D. in Earth System Science — 2018–Present

- Dissertation: "Projecting the evolution of Totten Glacier, East Antarctica, over the 21st century using ice-ocean coupled models"

University of California, Irvine — Irvine, CA
M.Sc. in Earth System Science, GPA: 4.00/4.00 — 2016–2018

- Specialization: Ice sheet modeling

State University of New York, College at Oswego — Oswego, NY
B.Sc. in Meteorology, GPA: 3.98/4.00 — 2012–2016
B.Sc. in Applied Mathematics, GPA: 3.96/4.00

- Thesis: "Analysis of the sensitivity of SUNY Oswego's local WRF to simulated lake ice cover"
- Thesis: "A mathematical analysis of sea ice inertial oscillations and drift kinematics within the Beaufort Gyre region of the Arctic Ocean"

Publications

1. **Pelle, T.**, Morlighem, M., Nakayama, Y. and Seroussi, H. Widespread grounding line retreat of Totten Glacier, East Antarctica, over the 21st century. Submitted to *Geophysical Research Letters*

2. Edwards, T. and **ISMIP6 Team** (2020). Quantifying uncertainties in the land ice contribution to sea level rise this century. Submitted to *Nature*

3. Payne, T. and **ISMIP6 Team** (2020). Contrasting contributions to future sea level under CMIP5 and CMIP6 scenarios from the Greenland and Antarctic ice sheets. Submitted to *Geophysical Research Letters*

4. McCormack, F. S., Roberts, J. L., Gwyther, D. E., Morlighem, M., **Pelle, T.**, and Galton-Fenzi, B. K. The impact of variable ocean temperatures on Totten Glacier stability and discharge. *Geophysical Research Letters*, 48, e2020GL091790. https://doi.org/10.1029/2020GL091790

5. **Pelle, T.**, Morlighem, M., and McCormack, F. S. (2020). Aurora Basin, the weak underbelly of East Antarctica. *Geophysical Research Letters*, 47, e2019GL086821. https://doi.org/10.1029/2019GL086821

6. Seroussi, H. and **ISMIP6 Team** (2020). ISMIP6 Antarctica: a multi-model ensemble of the Antarctic ice sheet evolution over the 21st century, *The Cryosphere*, 14, 3033–3070. https://doi.org/10.5194/tc-14-3033-2020

7. **Pelle, T.**, Morlighem, M., and Bondzio, J. H. (2019). Brief communication: PICOP, a new ocean melt parameterization under ice shelves combining PICO and a plume model, *The Cryosphere*, 13, 1043–1049, https://doi.org/10.5194/tc-13-1043-2019

Conference Presentations

- **American Geophysical Union Fall Meeting**
  - 2020: "The coupled response of Totten Glacier, East Antarctica, to 21st century ocean forcing" — Virtual Poster
  - 2020: "The development of East Antarctic ocean simulation with a focus on the Totten Glacier" — Virtual Oral
  - 2019: "Aurora Basin, the weak underbelly of East Antarctica" — Poster
  - 2019: "Stability of Totten Glacier under present-day forcing" — Poster
  - 2019: "Projections of Antarctic ice sheet evolution over the 21st century from the Ice Sheet Model Intercomparison for CMIP6 (ISMIP6)" — Poster
  - 2018: "Modeling the future evolution of the East Antarctic Ice Sheet under enhanced oceanic thermal forcing using newly combined melt rate parameterizations" — Poster
  - 2017: "Sensitivity of Totten Glacier Ice Shelf extent and grounding line to oceanic forcing" — Poster
- **European Geophysical Union Annual Meeting**
  - 2020: "Aurora Basin, the weak underbelly of East Antarctica" — Virtual Oral
- **SCAR 2020 Online**
  - 2020: "Aurora Basin, the weak underbelly of East Antarctica" — Virtual Poster

Research Experience

University of California, Irvine — Irvine, CA
Ice Sheet Model Intercomparison Project for CMIP6 (ISMIP6) — 2018–2019

- UCI-JPL Team Researcher
- Collaborated with 60 international scientists to compose an ensemble of Antarctic mass balance projections. I implemented new melting parameterizations, led the higher-order model simulations, validated the model output, and prepared the final model submissions.

Massachusetts Institute of Technology, Haystack Observatory — Westford, MA
Research Experience for Undergraduates (REU) Program — Summer 2015

- Research Affiliate
- Analyzed the relationship between changes in wind field curl rate and sea surface height within the Beaufort Gyre region of the Arctic Ocean

State University of New York, College at Oswego — Oswego, NY
Ontario Winter Lake-effect Systems (OWLeS) research campaign — Winter 2014

- Field Researcher
- Launched rawinsondes in the field of study to better understand the atmospheric evolution during lake effect snow storms, drafted research reports, lead and planned daily team missions.

Teaching and Leadership

- **In-class Teacher** at the University of California, Irvine — Spring 2019
  - Data Analysis: Time series decomposition & model fitting

- **Presentation Coordinator** for the Cryosphere Group at UCI 2018–Present
  - Scheduled and led weekly in-person and online (Zoom) meetings
- **Private Tutor** with TutorNerds 2017–Present
  - Subjects: Mathematics, Earth Science, Physics, & Coding
- **In-class Teacher** with CLEAN Education Winter 2017
  - Changes to the Cryosphere (Elementary education)
- **Student Teaching Assistant** at the University of California, Irvine 2017–2020
  - Classes: Oceanography, Data Analysis, Climate Change, Cryosphere Change, & Air Pollution

Scholarships and Awards

- NASA Group Achievement Award 2019
- SUNY Chancellor's Award for Student Excellence 2016
- Lewis R. DeRitter Award in Upper Division Mathematics 2013, 2014, & 2015
- Emmet Stopher Calculus Award 2012

ABSTRACT OF THE DISSERTATION

Projecting the evolution of Totten Glacier, East Antarctica, over the 21st century using ice-ocean coupled models

By

Tyler Pelle

Doctor of Philosophy in Earth System Science

University of California, Irvine, 2021

Associate Professor Mathieu Morlighem, Chair

Totten Glacier, the primary ice discharger of the East Antarctic Ice Sheet (EAIS), contains 3.85 m sea level rise equivalent ice mass (SLRe) and has displayed dynamic change driven by interaction of its ice shelf with the Southern Ocean. To project Totten Glacier's evolution, it is critical that sub-shelf ocean processes are properly resolved in dynamic ice sheet models. First, we combine an ocean box model with a buoyant plume parameterization to create PICOP, a novel melt parameterization that resolves sub-shelf vertical overturning and produces melt rates that are in excellent agreement with observations. We then use this parameterization to make century-scale mass balance projections of the EAIS, forced by surface mass balance and ocean thermal anomalies from ten global climate models. Although increased snowfall offsets ice discharge in high emission scenarios and results in ∼10 mm SLRe gain by 2100, significant grounded ice thinning (1.15 m/yr) and mass loss (∼6 mm SLRe) from Totten Glacier is projected. To investigate whether PICOP misses important processes, such as the advection of warm water into the ice shelf cavity, we develop a fully coupled ice-ocean model and find that warm water is able to access Totten Glacier's sub-shelf cavity through topographic depressions along the central and eastern calving front. By mid-century in high emission scenarios, warm water intrusions become strong enough to overcome topographic barriers and dislodge Totten Glacier's southern grounding line, triggering abrupt accelera-

tion in ice discharge (+185%). Overall, the timing and extent of Totten Glacier's retreat is predominately controlled by the sub-shelf ocean circulation, highlighting the importance of studying dynamic glaciers in fully coupled ice-ocean models.

Chapter 1

Introduction

1.1 Climate change and global sea level rise

Anthropogenic emissions of greenhouse gasses have increased since the pre-industrial era, leading to atmospheric concentrations of carbon dioxide, methane, and nitrous oxide that are unprecedented in at least the last 800,000 years (Pachauri et al., 2014). According to the Intergovernmental Panel on Climate Change's Fifth Assessment Report, it is extremely likely that these anthropogenic drivers are the dominant cause of the observed warming trend of 0.85°C over the period of 1880–2012 (Pachauri et al., 2014). These abrupt increases in tropospheric temperature have driven change in nearly all Earth System components; however, changes to the Earth's cryosphere are being amplified due to positive feedback loops (e.g. the ice-albedo feedback) that amplify warming in these regions. One of the primary consequences of a changing cryosphere is the threat of global sea level rise, putting coastal communities and infrastructure at risk of being inundated if warming continues unabated.

Between 2006 and 2015, the combination of ice sheet and glacier contributions has, for the first time, overtaken thermal expansion as the primary source of global sea level rise (1.7

mm/yr, IPCC, 2019). In fact, ice mass loss from the Greenland and Antarctic ice sheets has doubled and tripled, respectively, over the time period of 2007–2016 relative to 1997–2006. Together, the Greenland and Antarctic ice sheets contain 64 m of global sea level equivalent ice mass (SLRe) and are projected to lose between 0.43 and 0.84 m of this ice mass by the end of the century, relative to 1986–2005 (Morlighem et al., 2020, 2017; IPCC, 2019). This large degree of uncertainty in future projections of global sea level stems primarily from a lack of knowledge of the Antarctic Ice Sheet (AIS). Specifically, sparse observations, inadequate model representation of physical processes, and limited understanding of the complex interactions between the AIS and other Earth System components complicates projections of the future dynamic evolution of this ice mass. In order to reduce these uncertainties and provide policy makers with timely and reliable sea level estimates, it is critical we better understand the physical processes that are driving dynamic change of the AIS.

1.2 Forcing of the Antarctic Ice Sheet

The AIS, spanning an area that is equivalent to the United States and Mexico combined, is completely surrounded by the Southern Ocean (figure 1.1). Unlike the Greenland ice sheet, in which 50% of its mass loss is due to surface melting (van den Broeke et al., 2016), surface air temperatures over the AIS rarely exceed freezing due primarily to the lack of neighboring land masses as well as the zonal flow of the Southern Ocean. This impedes surface melting across the ice sheet, which means that the majority of mass loss from the AIS occurs as ice discharge in regions of fast flowing glaciers that we call "ice streams" (Pritchard et al., 2012). The point at which these ice screams lose contact with the underlying bedrock and begin to float over the ocean is called the grounding line, and these floating extensions are called ice shelves. Ice shelves along the periphery of the AIS buttress the ice streams feeding them, acting to impede the flow of grounded ice into the ocean and hinder sea level rise (De Angelis

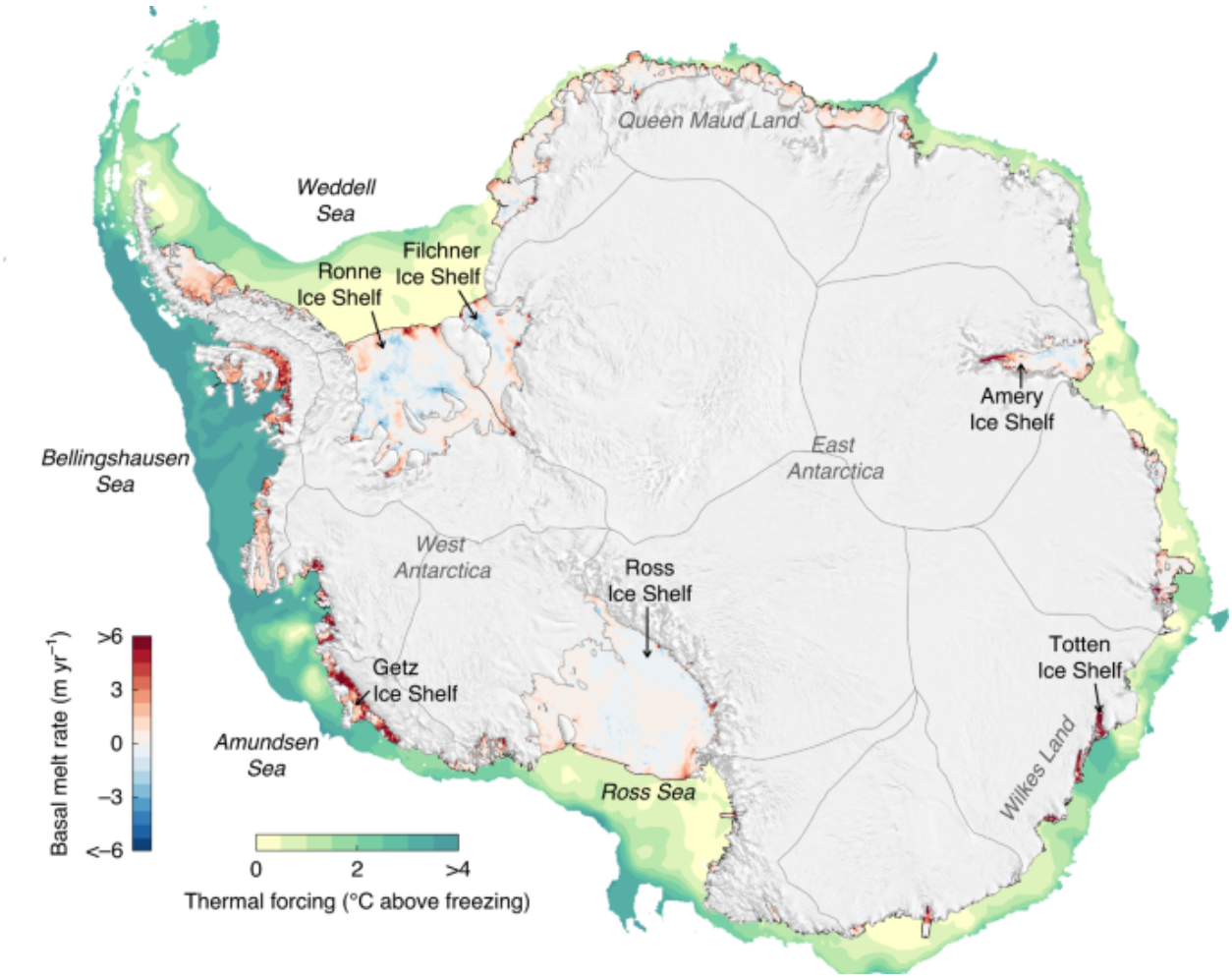

Figure 1.1: The Antarctic Ice Sheet is displayed with satellite inferred basal melting rates shaded over floating ice shelves, averaged between 2010–2018. Ocean thermal forcing, defined as the ocean water temperature above the in situ freezing point of seawater, is shaded for water depths less than 1.5 km. Drainage basins from Rignot et al. (2011) are delineated with gray lines over grounded ice. The East and West Antarctic ice sheets are named, as well as major outlet glaciers and seas off the Antarctic coast. This figure was taken from Adusumilli et al. (2020).

and Skvarca, 2003; Gudmundsson, 2013). Thus, as ice shelves lose mass, their buttressing potential decreases and the flow of upstream grounded ice accelerates. It is important to note that ice shelf mass loss does not directly contribute to global sea level rise, as the floating ice is already in hydrostatic equilibrium. Rather, it is the resultant acceleration of grounded ice discharge across the grounding line the contributes to sea level rise.

Recently, melting at the base of these ice shelves by warm ocean water (hereon referred to as "basal melting" in units of meters of ice shelf thinning per year) has overtaken iceberg calving (the process in which slabs of ice at the downstream portion of the ice shelf break off and are discharged into the ocean) as the primary process that drives ice shelf mass loss (Rignot et al., 2013). Ice shelf basal melting is theorized to occur by three main processes: (1) the circulation of cold, High-Salinity Shelf Water (HSSW) to the grounding line where it is above the in situ freezing point and induces melt, (2) the circulation of Antarctic Surface Water (AASW) beneath ice shelves, and (3) the spreading of warm, modified Circumpolar Deep Water (mCDW) into the sub-ice shelf ocean cavity (Dinniman et al., 2016). In the last case, warm water spreads along the continental shelf and flows into a glacier's sub-ice shelf cavity through local depressions and troughs in bed topography, where it can upwell against the grounding line. Melting at the grounding line results in an input of cold, fresh melt water into the ocean, producing a buoyancy driven melt water plume that travels along the base of the ice shelf from the grounding line to the ice front (or to the point at which the plume loses buoyancy, see figure 1.2). As such, basal melting tends to be highest near the grounding line and decrease with proximity to the ice front, as the warm ocean water loses heat to the cold melt water. Melting and/or refreezing along the trajectory of this plume is sensitive to the temperature of the ocean water, as well as the velocity at which the water travels (faster ocean flow drives higher melting rates).

Antarctic ice shelves are largely classified as "warm water" or "cold water", depending on whether the deep waters adjacent to the ice shelf are dominated by colder HSSW or warmer

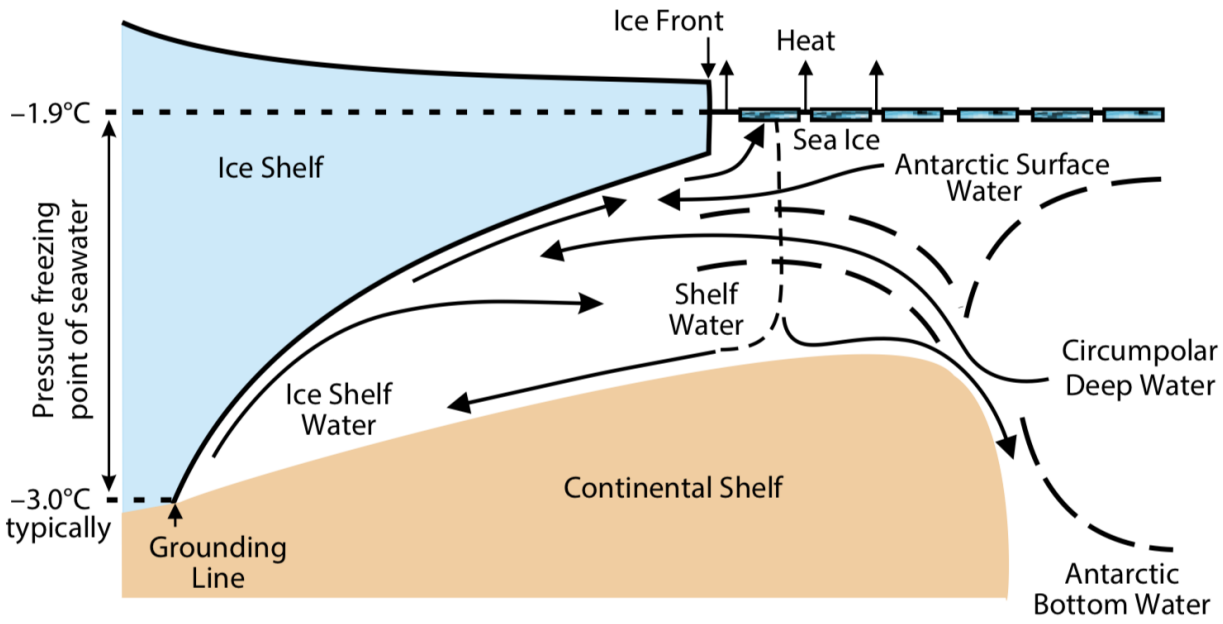

Figure 1.2: Schematic diagram showing the water masses (shelf water, Antarctic bottom water, circumpolar deep water, and ice shelf water) and the general flow of these water masses within the sub-ice shelf cavity. The grounding line and ice front are labeled, and the sea surface height is denoted by the black dashed line. Ice is shaded in blue and bed topography is shaded in tan. The approximate pressure freezing point of seawater is displayed on the y-axis of the figure. This figure was adapted from Dinniman et al. (2016)

mCDW (Petty et al., 2013). Along the western Ross and Weddell Seas, strong sea ice formation produces cold HSSW that reduces basal melting rates to 0.1–1 m/yr. In contrast, intrusions of mCDW have been observed to drive rapid basal melting of glaciers within the Amundsen Sea sector of the West Antarctic Ice Sheet, where melt rates exceed 100 m/yr (Adusumilli et al., 2020). Melting of these ice shelves is so intense that the fresh melt water that is ejected into the ocean along the continental shelf has been observed to influence downstream ocean dynamics as far west as Ross Sea (Jacobs and Giulivi, 2010). In addition, while the majority of ice shelves along the East Antarctic coast experience cold sub-ice shelf conditions, there are a few ice shelves that display rapid basal melting that is indicative of the presence of mCDW (see figure 1.1, Rintoul et al., 2016; Roquet et al., 2018). As one can see, oceanic forcing of glaciers along the Antarctic Coast is a product of various complex processes that are coupled to other Earth System components. The range of resultant basal melting rates spans four orders of magnitude, includes both positive (melting) and negative (refreezing) values, and is highly heterogeneous across short spatial distances.

1.3 Ice sheet modeling

In order to accurately project the future sea level rise contribution of the AIS, it is key that we better understand the processes that drive the observed rapid basal melting of Antarctic ice shelves. Obtaining direct observations of the ocean near and beneath ice shelves, however, is logistically challenging and dangerous. As such, scientists have turned to numerical modeling. Over the past two decades, ice sheet modeling has undergone a renaissance through the development and validation of several state-of-the-art ice flow models (e.g. PISM, CISM, MALI, SICOPOLIS, ISSM, IMAUICE, etc.), allowing scientists to understand and extend the sparse oceanographic measurements that exist near ice shelves; however, many key aspects, such as sub-ice shelf ocean circulation and ice shelf basal melting, remain poorly un-

derstood due to the difficulty of obtaining direct observations (for a more detailed overview of ice flow modeling, see appendix A). As the AIS is primarily forced by the Southern Ocean, resolving ice-ocean processes in stand-alone and coupled ice sheet models is necessary in order to deliver timely and reliable sea level estimates. At present, there are two ways to simulate ice-ocean interactions in ice sheet models: **(1)** through the use of simplified sub-ice shelf basal melting rate parameterizations, and **(2)** through coupling of the ice sheet model to an ocean general circulation model that is capable of simulating ocean flow within sub-ice shelf cavities. Below, we summarize the state of the science for both methods.

1.3.1 Basal melting rate parameterizations

In order to make century- and continental-scale ice sheet projections, it is not computationally feasible to couple an ice sheet model to a numerical ocean model to simulate ice shelf basal melting (due to the comparatively small time step the ocean model needs to reach convergence). These large-scale projections are necessary in order to simulate the total sea level contribution of the AIS, project the evolution of the AIS through past epochs (e.g. the Last Interglacial, ∼130–115 ka), or to extend sea level projections beyond 2100. As such, it is necessary to derive simplified approximations of the ice-ocean processes governing ice shelf basal melting that can be run within standalone ice sheet models; these modules are called "basal melting rate parameterizations."

The first models of ice shelf-ocean interactions that emerged were derived as one-dimensional plume models, which represent the steady-state ocean current as a buoyant melt-water plume in one spatial dimension (Jenkins, 1991). Despite their simplicity, these plume parameterizations offered significant insight into the processes that control melting and refreezing of ice shelves. Parameterizations of basal melt evolved to be based on the local flux of heat at the ice-ocean interface (DeConto and Pollard, 2016; Beckmann and Goosse, 2003; Jourdain

et al., in review), basal slopes (Little et al., 2012), and the thickness of the water column beneath the ice shelf (depth dependent parameterizations, Asay-Davis et al., 2016). While computationally inexpensive and relatively easy to implement in transient ice sheet models, these parameterizations are typically derived with numerous tuning factors and are unable to resolve the complex spatial pattern of melt rates observed across the AIS. More recently, basal meting rate parameterizations have evolved to be able to capture the buoyancy-driven overturning circulation within the sub-ice shelf cavity. Reese et al. (2018) are able to resolve the magnitude of observed melt rates across the AIS through the implementation of a sub-ice shelf ocean box model, which solves for the transport of heat and salt along the ice-ocean interface (see section 2.1). In addition, Lazeroms et al. (2018) derived a basal melt rate parameterization that is based on the physics of buoyant melt water plums that travel along the base of ice shelves. This plume parameterization takes into account the sub-ice shelf geometry while capturing the evolution of the plume through its traverse from the grounding line to the ice front (see section 2.2).

While contemporary basal melting rate parameterizations have come a long way, there are still many outstanding bottlenecks that impede large-scale AIS projections. Early basal melting rate parameterizations fail to capture the impact of ocean circulation and the interaction of ocean circulation with ice shelf cavity geometry, both of which have been cited as primary controls on basal melting (Jenkins, 1991; Little et al., 2009). Limitations of Reese et al. (2018) and Lazeroms et al. (2018) will be discussed in chapter 2.

1.3.2 Ice-ocean model coupling

Two way ice-ocean model coupling is the most accurate way to simulate ice-ocean interactions in numerical ice sheet models, as the ocean model is able to solve for the full three-dimensional sub-ice shelf ocean circulation. However, due to its large computational cost, coupled model

simulations are limited to the decadal- and basin-scale. There exist several ocean general circulation models that are capable of simulating the full three-dimensional ocean circulation with sub-ice shelf cavities (e.g. MITgcm, MOM6, MPAS-Ocean, etc.); however, there exist a limited number of publications that feature coupled, dynamic ice sheet/ocean models in a realistic configuration (as opposed to the use of idealized ice shelf cavity geometry and bathymetry to study ice-ocean interaction at the process level).

At present, coupled ice-ocean models are run asynchronously, in which the ocean model is run forward after changes in ice geometry have been updated at each coupling interval. For instance, Seroussi et al. (2017) asynchronously coupled the Ice-sheet and Sea-level System Model (ISSM) to the ocean component of the Massachusetts Institute of Technology general circulation model (MITgcm) to make 50-year projections of Thwaites Glacier and found that ice-ocean interactions that were missing in the uncoupled simulations led to overestimated retreat. This suggests that at the basin-scale, ice-ocean model coupling is the most accurate way to simulate the dynamic evolution of a glacial system; however, the technical challenges and computational limitations of two way ice-ocean model coupling presents the scientific community with steep barriers. Furthermore, while glaciers along the West Antarctic coast have been studied in this framework, Totten Glacier and other dynamic glaciers along the East Antarctic coast that have displayed sensitivity to enhanced oceanic thermal forcing but have yet to be studied.

1.4 Observations of the East Antarctic Ice Sheet and Totten Glacier

While the majority of scientific focus has been aimed at Weat Antarctic Ice Sheet (WAIS) due to its observed dynamic state, low-lying sectors of East Antarctic Ice Sheet (EAIS)

have been shown to be vulnerable to warmer-than-present temperatures during the Last Interglacial and Pliocene epoch (Cook et al., 2013; Aitken et al., 2016; DeConto and Pollard, 2016). During these warm periods, glacial margins retreated several hundreds of kilometers inland over the Wilkes and Aurora Subglacial Basins, caused by elevated Southern Ocean temperatures (figure 1.3, Cook et al., 2013). Additionally, large-scale advance and retreat patterns of EAIS within the Aurora Subglacial Basin have been inferred from spatial-patterns of inland bed erosion, leading to over a four meter loss of sea level rise equivalent ice volume from this region during the Pliocene epoch (Aitken et al., 2016). Recent observations show that EAIS contains ∼52 m SLRe and has lost 51 ± 13 Gt/yr of ice between 2009 and 2017, comprising 20% of the total mass loss of Antarctica during this period (Morlighem et al., 2019; Rignot et al., 2019). This mass loss and acceleration is a dynamic response of the ice sheet to enhanced oceanic thermal forcing at glacial margins (Rignot et al., 2019).

Totten Glacier, the largest ice discharger of the East Antarctic Ice Sheet, has recently gained notoriety for its possible sensitivity to changes in climate forcing. Most of Totten Glacier's drainage basin is grounded well below sea level, with the deepest region grounded nearly 2000 m below sea level and located just upstream of Totten Glacier's retreating grounding line (Morlighem et al., 2020; Li et al., 2015). This configuration presents the threat of significant grounded ice loss in the future if the grounding line were to continue retreating. Presently, Totten Glacier holds a sea level potential of 3.85 m and has lost, on average, 7.3 Gt/yr of ice mass between 2003–2017, increasing in flux by 10% relative to 1979-2003 (Morlighem et al., 2020; Rignot et al., 2019).

Contemporary observations reveal that Totten Glacier is undergoing complex patterns of change, forced primarily by changes in sub-ice shelf ocean conditions. Seasonal intrusions of warm, modified Circumpolar Deep Water (mCDW) have been found to encroach onto the continental shelf through topographic depressions at the shelf break (Roberts et al., 2018; Rintoul et al., 2016; Morlighem et al., 2020; Gwyther et al., 2018). Warm water (-1 –

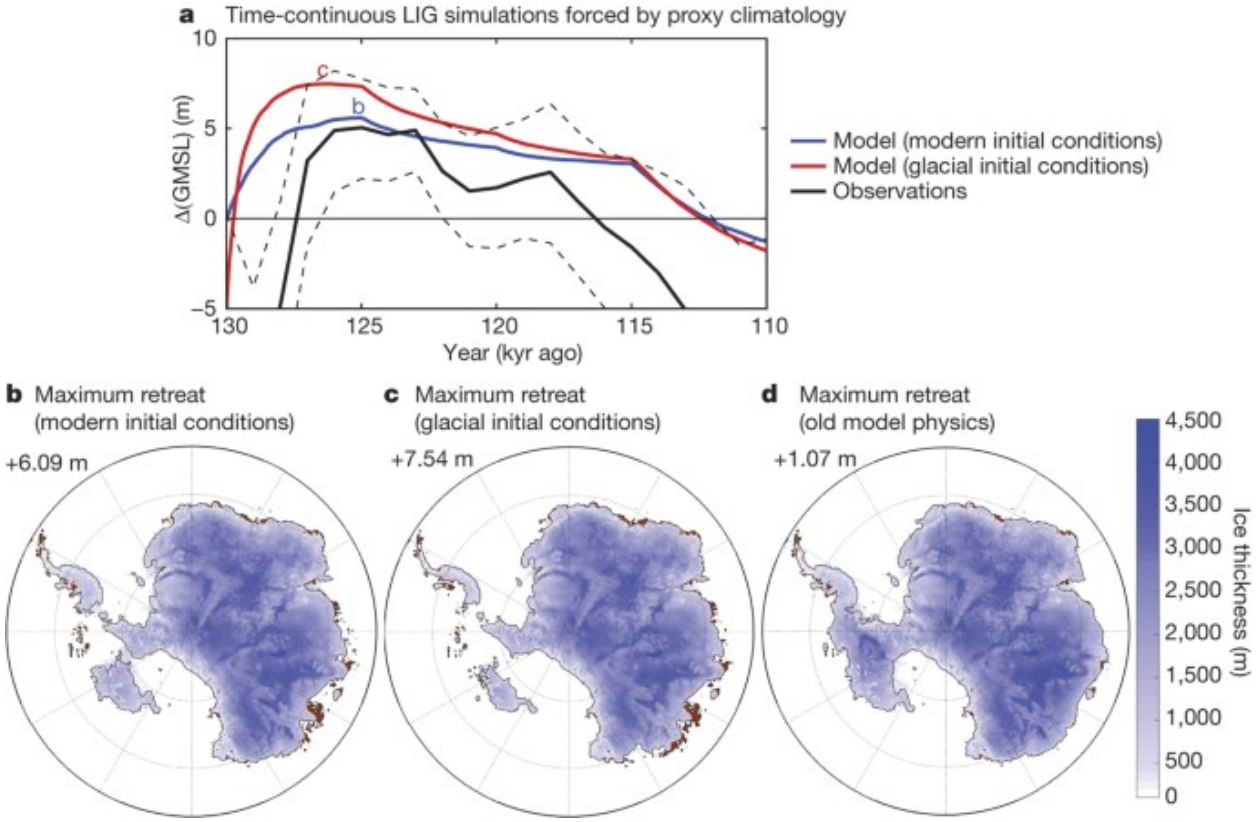

Figure 1.3: (a) Change in global mean sea level (GMSL) over the Last Interglacial (LIG, 130-110 ka) forced by proxy climatology with initial conditions indicative of the present day (blue) and the onset of the LIG (red). A probabilistic reconstruction of Antarctica's contribution to GMSL denoted by the black line, with the associated uncertainties (16^{th} and 84^{th} percentiles) given by the dashed black lines. (b-d) Ice sheet thickness during the time of maximum retreat during the LIG using modern initial conditions (b), LIG initial conditions (c), and modern initial conditions without use of new model physics that accounts for Marine Ice Cliff Instability (d). Note the significant retreat simulated over the Aurora Subglacial Basin in (b) and (c). This figure was taken from DeConto and Pollard (2016).

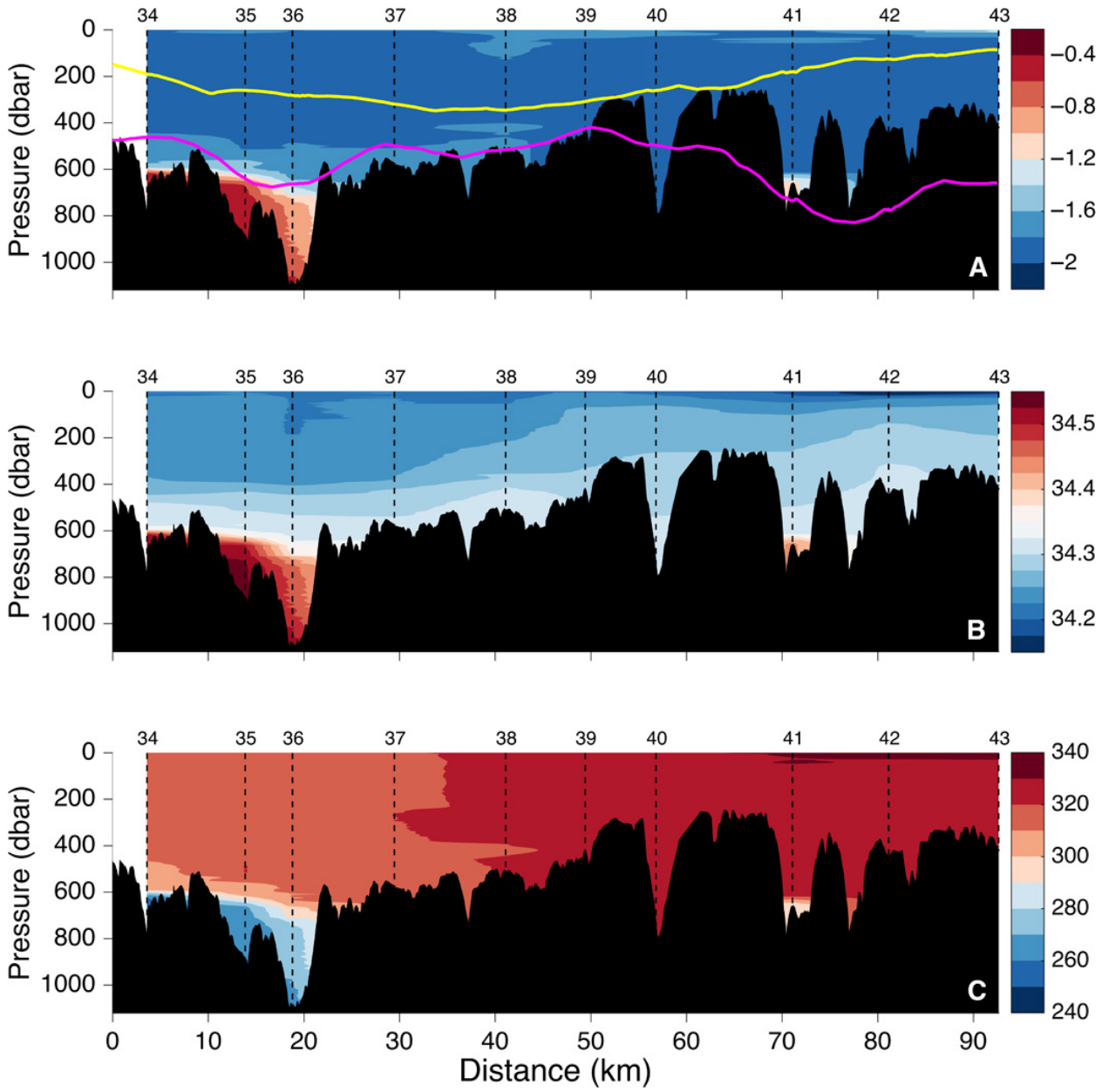

Figure 1.4: Observations of (a) potential temperature in units of °C, (b) salinity in units on the Practical Salinity Scale, and (c) oxygen in units of μM taken along Totten Glacier's ice front running from west (left) to east (right). The yellow and magenta lines in panel-a denote the depth of the bed topography taken from Fretwell et al. (2013) and Greenbaum et al. (2015), respectively. Note the presence of mCDW near measurement sites 36 and 41. This figure was taken from Rintoul et al. (2016).

0°C) has been observed at Totten Glacier's ice front at depths below 500 m (Rintoul et al., 2016), supplying the forcing necessary to induce rapid basal melting if it can intrude into Totten Glacier's sub-ice shelf cavity. The resultant ice shelf thinning reduces back-stress that this floating extension exerts on the upstream glacier, leading to accelerations in grounded ice speed and enhanced ice discharge (Rignot and Jacobs, 2002; Dupont and Alley, 2005, 2006). Li et al. (2016) observed grounded ice velocity accelerations to be synchronous with these warm water intrusions, suggesting that ocean forced ice shelf thinning may already be taking place. Thinning was greatest along a weakly grounded "ice plain" that is located within the first 5 km upstream of Totten Glacier's southern grounding line (Li et al., 2015). This ice plain acts as an important pinning point of Totten Glacier, in which a 1–3 km retreat of Totten Glacier's grounding line was observed between 1996–2013 (Li et al., 2015). Significant thinning (0.6 m/yr between 2017–2100) has also been observed along Totten Glacier's eastern grounding zone, where updated maps of bed topography reveal a gentle sloping bed that might be conducive to grounding line retreat (Pritchard et al., 2012; Li et al., 2015; Morlighem et al., 2020).

Recent modeling studies have found that changes in sub-shelf ocean conditions are the primary driver of the observed dynamic changes Totten Glacier has been experiencing over the past two decades (Roberts et al., 2018; Gwyther et al., 2018). These studies, however, do not capture the full impact of changing sub-shelf ocean conditions on the system due to their use of simplified parameterizations of sub-ice shelf basal melt and/or fixed ice sheet geometry. As the primary driver of future variability of Totten Glacier, it is essential we properly resolve the sub-ice shelf ocean circulation in a coupled ice-ocean model framework if we seek to constrain the future evolution of this vulnerable glacier (Seroussi et al., 2017).

1.5 Objectives of this dissertation

In this dissertation, we seek to make projections of Totten Glacier through the 21st century using a hierarchy of ice-ocean coupled models with the following primary objectives:

1. Constrain the century-scale projected sea level contribution of Totten Glacier
2. Accurately simulate Totten Glacier's dynamic evolution, including future grounding line retreat, regions of grounded ice thinning, and changes in the glacier's ice velocity.
3. Identify possible tipping-points and/or thresholds of forcing that would lead to destabilization of Totten Glacier.
4. Understand how projected changes in ocean forcing will impact the future evolution of Totten Glacier.

In chapter 1, we provided background information on the current state of the Antarctic Ice Sheet, ice sheet modeling, how ice-ocean interactions are simulated in standalone and coupled ice sheet models, as well as the current state of the East Antarctic Ice Sheet and Totten Glacier. In chapter 2, we develop a new parameterization of ice shelf basal melting that resolves sub-ice shelf ocean circulation and requires only a single temperature and salinity value (per basin) as inputs. The complete derivation of this parameterization has been published in *The-Cryosphere* (Pelle et al., 2019; Reese et al., 2018; Lazeroms et al., 2018). In chapter 3, we use this new melt rate parameterization to make century-scale protections of dynamic EAIS basins, forced by surface mass balance and ocean thermal anomalies from global climate model output. This work was published in *Geophysical Research Letters* (Pelle et al., 2020). In chapter 4, we make fully coupled ice-ocean projections of Totten Glacier through 2100 to investigate this glacier's dynamic response to realistic changes in ocean forcing. This work has recently been submitted to *Geophysical Research Letters* and

is currently pending publication. Lastly, the projected century-scale evolution of Totten Glacier is summarized in chapter 5, as well as the associated scientific implications and future outlooks of the research presented in this dissertation. Appendix A presents a brief overview of the mechanical equations underpinning ice flow in dynamic ice sheet models.

Chapter 2

Development of PICOP basal melting rate parameterization

In this chapter, we detail the derivation of a new basal melting rate parameterizations that can be used to accurately and efficiently simulate ice-ocean interactions in standalone numerical ice sheet models. As discussed in section 1.3.1, the development of basal melting rate parameterizations has come a long way, as contemporary parameterizations are beginning to resolve the large-scale ocean processes that govern ice shelf-ocean interactions. In particular, two of the most recently published melt parameterizations that resolve sub-shelf ocean circulation are the **P**otsdam **I**ce-shelf **C**avity m**O**del (PICO, Reese et al., 2018) and one based on the physics of buoyant melt water plumes (plume model, Lazeroms et al., 2018). Although both parameterizations are novel in their own regards, melt rates calculated by PICO suffer from unrealistic "banding" as a product of its box model approach and remain too low near grounding lines. As forcing at a glacier's grounding line modifies the entire stress regime of the system, it is critical to accurately simulate the spatial distribution and magnitude of melting in these regions. In addition, the plume model requires complete sub-shelf ocean temperature and salinity fields as inputs, and has not been adapted to use in transient model

runs. We overcome these limitations by combining both PICO and the plume model to form PICOP: we rely on PICO's box model to reconstruct the temperature and salinity fields beneath ice shelves based on far field ocean properties and then use this reconstruction to drive the plume model, which calculates the basal melt rate field. Below, we describe the physics used to derive PICOP and compare melt rates produced by PICO and PICOP to observations by Rignot et al. (2013) in three basins of varying oceanic conditions and geometry. Note that the derivations of PICO (section 2.1) and the plume model (section 2.2) are adapted from Reese et al. (2018) and Lazeroms et al. (2018), respectively. All constants and external parameters used in the derivations of both parameterizations are summarized in table 2.1.

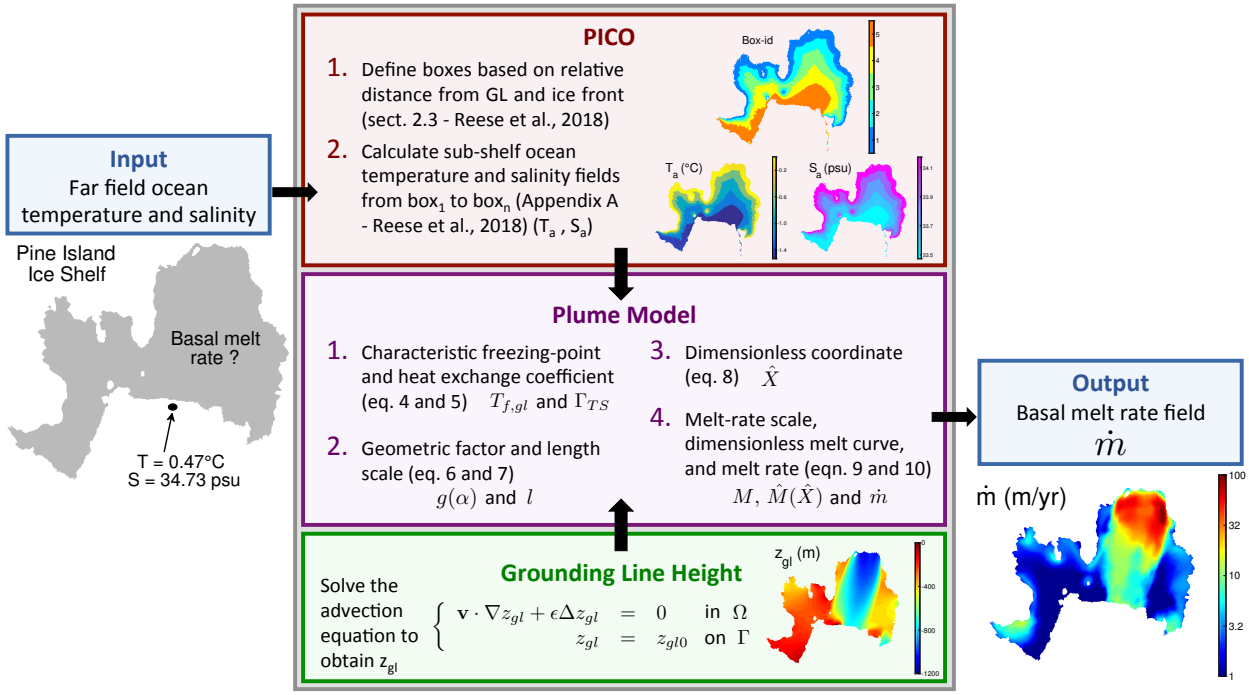

Figure 2.1: Schematic diagram of PICOP with example data displayed for the Pine Island ice shelf of West Antarctica. The inputs into the parameterization are the basin averaged ocean temperature (°C) and salinity (units on the Practical Salinity Scale), which are first fed into PICO (red box). PICO uses these inputs to calculate the sub-shelf ambient ocean temperature and salinity fields, which are then used in the plume model (purple box). In addition, the grounding line height is calculated at this time by solving the advection problem defined in the green box. Once these three fields are fed into the plume model, the basal melt rate field is computed according to the steps outlined in the purple box.

External Quantity	**Symbol**	**Source**	**Unit**
Far-field ocean temperature	T	Reese et al. (2018)	°C
Far-field ocean salinity	S	Reese et al. (2018)	PSU
Local depth of ice shelf base	z_b	Morlighem et al. (2020)	m
Local slope angle	ξ	Morlighem et al. (2020)	-
Grounding line depth	z_{gl}	Solve advection problem	m
Ambient ocean temperature	T_a	PICO	°C
Ambient ocean salinity	S_a	PICO	psu
Basal melt rate	$\dot{m}$	Plume model	m/yr
Common Constant Parameters	**Symbol**	**Value**	**Unit**
Gravitational acceleration	g	9.8	m s^{-2}
Density of ice	ρ_i	910	kg m^{-3}
Density of sea water	ρ_w	1028	kg m^{-3}
Latent heat of fusion	L	3.34×10^5	J kg^{-1}
Heat capacity of sea water	c_p	3974	J kg^{-1} °C
Unique Constant Parameters	**Symbol**	**Value**	**Unit**
Overturning strength	C	1×10^6	m^6 $s^{-1}kg^{-1}$
Salinity coefficient of freezing	a	-0.0572	°C PSU^{-1}
Constant coefficient of freezing	b	-0.0788	°C
Pressure coefficient of freezing	c	7.77×10^{-8}	°C Pa^{-1}
Thermal expansion coefficient in EOS	α	7.5×10^{-5}	$°C^{-1}$
Salt contraction coefficient in EOS	β	7.7×10^{-4}	PSU^{-1}
Reference density in EOS	ρ_*	1033	kg m^{-3}
Effective heat exchange velocity	γ_T^*	2×10^{-5}	m s^{-1}
Entrainment coefficient	E_0	3.6×10^{-2}	-
Drag coefficient	C_d	2.5×10^{-3}	-
Turbulent heat exchange coefficient	$C_d^{1/2}\Gamma_T$	1.1×10^{-3}	-
Freezing point-salinity coefficient	λ_1	-5.73×10^{-2}	°C
Freezing point offset	λ_2	8.32×10^{-2}	°C
Freezing point-depth coefficient	λ_3	7.61×10^{-4}	°C m^{-1}
Melt-rate parameter	M_0	10	m yr^{-1} $°C^{-2}$
Heat exchange parameter	$C_d^{1/2}\Gamma_{TS_0}$	6.0×10^{-4}	-
Heat exchange parameter	γ_1	0.545	-
Heat exchange parameter	γ_2	3.5×10^{-5}	m^{-1}
Dimensionless scaling factor	x_0	0.56	-
Epsilon	ϵ	10^{-14}	-

Table 2.1: Constant parameters and external quantities referenced in this chapter. Common parameters are those used in the derivation of both PICO and the plume model. Unique parameters are those that are not shared in the derivation of PICO and the plume model. See Reese et al. (2018) and Lazeroms et al. (2018) for a full list of constants used to derive PICOP.

2.1 PICO

PICO is a two-dimensional sub-shelf melt rate parameterization that simulates vertical overturning within sub-shelf cavities and is used here to produce complete sub-shelf ocean temperature and salinity fields (Reese et al., 2018). Inputs for PICO are the ocean temperature T and salinity S that are averaged for each basin along the base of the continental shelf just downstream of the basin's ice shelves. The sub-shelf ocean circulation is driven by the *ice pump* mechanism (Lewis and Perkin, 1986), in which melting at the base of the ice shelf near the grounding lines reduces the salinity of the ocean water, which then gains buoyancy. As such, the ocean water rises against the base of the ice shelf and is transported to the ice front, drawing ambient ocean water into the sub-ice shelf cavity to complete the haline-driven circulation. The transport of heat and salt through the sub-ice shelf cavity via this circulation is broken down through the implementation of an ocean box model.

2.1.1 Computing box numbers

To begin, individual mesh elements or grid cells within the model domain are assigned a box number based on their relative distance from both the grounding line and the ice front. For a given ice shelf D, we can determine the number of ocean boxes n_D by interpolating between 1 and n_{max}, where n_{max} is the user defined maximum number of boxes for the model domain (for a typical Antarctic setup, 5 boxes is sufficient). We compute the number of boxes n_D for each individual ice shelf D as follows:

$$n_D = 1 + rd\left(\sqrt{\frac{d_{GL}(D)}{d_{max}}} \times (n_{max} - 1)\right), \tag{2.1}$$

where $rd()$ rounds to the nearest integer, $d_{GL}(D)$ is the local distance to the grounding line from a given mesh element or grid cell in ice shelf D, and d_{max} is the maximum distance to

the grounding line in the model domain.

Now that we solved for the maximum number of boxes in each basin, we can define the boxes by assigning specific box-ids based on a grid cell's or mesh element's relative distance to the grounding line, r. We compute r with the following:

$$r = \frac{d_{GL}}{d_{GL} + d_{IF}}, \tag{2.2}$$

where d_{IF} is the local distance to the ice front from a given mesh element or grid cell. We now assign all grid cells or mesh elements with horizontal coordinates $(x, y) \in D$ to box B_k if the following condition is met:

$$1 - \sqrt{\frac{(n_D - k + 1)}{n_D}} \leq r\,(x, y) \leq 1 - \sqrt{\left(\frac{(n_D - k)}{n_D}\right)}. \tag{2.3}$$

This condition forces boxes beneath a given ice shelf to have comparable areas (see figure 2.1). Once box numbers have been defined across the model domain, we are able to solve for the sub-ice shelf ocean temperature and salinity fields.

2.1.2 Computing the sub-ice shelf temperature and salinity fields

After simplification and assuming steady state conditions, the balance of heat and salt in all boxes along the base of the ice shelf can be written as:

$$\begin{aligned} q\,(T_{k-1} - T_k) - A_k\,\nu\,\lambda m_k &= 0 \\ q\,(S_{k-1} - S_k) - A_k\,m_k\,S_k &= 0, \end{aligned} \tag{2.4}$$

where $\nu = \rho_i/\rho_w$, $\lambda = L/c_p$, salinity S_k and temperature T_k in box $\mathrm{B_k}$ are a function of

the local pressure p_k, the box area A_k, and the temperature T_{k-1} and salinity S_{k-1} of the upstream box B_{k-1}. Using the simplified formulation of the 3-equation melt model by Holland and Jenkins (1999), we replace the salinity in the ice-ocean boundary layer with the salinity of the ambient ocean water:

$$m_k = -\frac{\gamma_T^*}{\nu\lambda}\left(aS_k + b - cp_k - T_k\right), \tag{2.5}$$

where p_k is the overburden pressure computed as static-fluid pressure given by the weight of ice above, γ_T^* is between 2.2×10^{-5} and 3.2×10^{-5} ms^{-1} (see Reese et al. (2018) section 3.1 for a full explanation on the choice and validation of γ_T^*). Substituting in the simplified formulation of m_k into equation 2.5, we get:

$$\begin{aligned} q\left(T_{k-1} - T_k\right) + A_k\frac{\gamma_T^*}{\nu\lambda}\left(aS_k + b - cp_k - T_k\right)\nu\lambda &= 0 \\ q\left(S_{k-1} - S_k\right) + A_k\frac{\gamma_T^*}{\nu\lambda}\left(aS_k + b - cp_k - T_k\right)S_k &= 0. \end{aligned} \tag{2.6}$$

Now by replacing $x = T_{k-1} - T_k$, $y = S_{k-1} - S_k$, $T^* = aS_{k-1} + b - cp_k - T_{k-1}$, $g_1 = A_k\gamma_T^*$, and $g_2 = g_1/\nu\lambda$, we obtain:

$$\begin{aligned} qx + g_1\left(T^* + x - ay\right) &= 0 \\ qy + g_2\left(S_{k-1} - y\right)\left(T^* + x - ay\right) &= 0. \end{aligned} \tag{2.7}$$

We rewrite the first equation of equation 2.7 as

$$\left(T^* + x - ay\right) = \frac{-qx}{g_1}, \tag{2.8}$$

and substitute it into the second equation of equation 2.7 to get:

$$\begin{aligned} & qy + g_2 \left(S_{k-1} - y\right) \left(\tfrac{-qx}{g_1}\right) = qy - qx \tfrac{S_{k-1}-y}{\nu\lambda} = 0 \\ \iff & \nu\lambda y - S_{k-1}x + xy = 0 \\ \iff & \left(\nu\lambda + x\right) y - S_{k-1}x = 0 \\ \iff & y = \frac{S_{k-1}x}{\nu\lambda + x}. \end{aligned} \tag{2.9}$$

Note that we divided by q after the first step in equation 2.9, which is acceptable because we assumed $q > 0$. Now $x = T_{k-1} - T_k \ll \nu\lambda$, so we can ignore x in the denominator of the last equation in equation 2.9 to get:

$$y = \frac{S_{k-1}x}{\nu\lambda}. \tag{2.10}$$

With this approximation, it is now possible to solve the complete system of equations. Note that in box B_1 (the box adjacent to the grounding line), we must also solve for the strength of the overturning circulation, q, which is calculated once per time-step in box B_1 from the density difference between the far field and grounding line water masses:

$$q = C\rho_* \left(\beta \left(S_0 - S_1\right) - \alpha \left(T_0 - T_1\right)\right). \tag{2.11}$$

Note that the ocean water densities are computed assuming a linear approximation to the equation of state. The temperature of the water along the base of the continental shelf is typically close to the pressure freezing point of sea water. As such, density differences between far-field and grounding line water masses will primarily result from freshening via the fresh melt water flux from the ice shelf into the ocean (rather than by temperature

differences). Substituting this equation into equation 2.7 yields:

$$\begin{aligned} \alpha x^2 - \beta xy - \frac{g_1}{C\rho_*}\left(T^* + x - ay\right) &= 0 \\ -\beta y^2 + \alpha xy - \frac{g_2}{C\rho_*}\left(S_0 - y\right)\left(T^* + x - ay\right) &= 0. \end{aligned} \tag{2.12}$$

Now by inserting the approximation from equation 2.10 into the first expression of equation 2.12, we obtain a quadratic equation for x:

$$\left(\beta s - \alpha\right) x^2 + \frac{g_1}{C\rho_*}\left(T^* + x\left(1 - as\right)\right) = 0, \tag{2.13}$$

where $s = S_0/\nu\lambda$. Because $as = -0.057 \times S_0/74.76 = -0.000762 \times S_0 \ll 1$, we can exclude $(1 - as)$ in equation 2.13 to get:

$$\left(\beta s - \alpha\right) x^2 + \frac{g_1}{C\rho_*}\left(T^* + x\right) = 0. \tag{2.14}$$

By rearranging equation 2.14, we obtain the solution:

$$x = -\frac{g_1}{2C\rho_*\left(\beta s - \alpha\right)} \pm \sqrt{\left(\frac{g_1}{2C\rho_*\left(\beta s - \alpha\right)}\right)^2 - \frac{g_1 T^*}{2C\rho_*\left(\beta s - \alpha\right)}}. \tag{2.15}$$

Note that the first term in equation 2.15 is negative, so the negative solution can be excluded. From here, we use $T_1 = T_0 + x$ and $y = xS_0/\left(\nu\lambda\right)$ to solve for T_1, S_1, and q (equation 2.11).

Now that we have solved for the temperature, salinity, and overturning strength in box B_1, we can derive the solution for boxes B_K where $k > 1$. To do so, we substitute the approximation made in equation 2.10 into the first equation of equation 2.7 and solve for x

as follows:

$$\begin{aligned} & qx + g_1\left(T^* + x - a\tfrac{S_{k-1}x}{\nu\lambda}\right) = 0 \\ \iff\ & qx + g_1T^* + g_1x - g_2aS_{k-1}x = 0 \\ \iff\ & -g_1T^* = x\left(q + g_1 - g_2S_{k-1}a\right) \\ \iff\ & x = \frac{-g_1T^*}{q + g_1 - g_2S_{k-1}a}. \end{aligned} \tag{2.16}$$

This equation can now be solved for T_k ($T_k = T_{k-1} + x$), which can then be used to solve for S_k using equation 2.10. Once this is complete, we have fully solved for the sub-shelf temperature and salinity fields, which will be used as input into the plume model to solve for the sub-ice shelf basal melting rate field (fig. 2.1).

2.2 Plume model

The plume model is a basal melt rate parameterization based on the theory of buoyant melt water plumes that travel upward along the base of the ice shelf from the grounding line to the location where the plume loses buoyancy. The two-dimensional formulation from Lazeroms et al. (2018) is adapted from the one-dimensional plume model developed by Jenkins (1991) for a plume traveling in direction X in an ocean with ambient temperature T_a and salinity S_a (provided by PICO). We begin by defining the grounding line depth, z_{gl}, over the entire ice shelf, as it is necessary to determine where individual plumes originate in order to employ this parameterization. As a first approximation, we solve an advection equation:

$$\begin{cases} \mathbf{v}\cdot\nabla z_{gl} + \epsilon\Delta z_{gl} = 0 & \text{in } \Omega \\ z_{gl} = z_{gl0} & \text{on } \Gamma \end{cases} \tag{2.17}$$

where z_{gl0} is the grounding line height defined at the grounding line Γ, Ω is the ice shelf, and as a first approximation, $\mathbf{v}$ is the modeled, depth-averaged ice velocity. Note that ϵ is a small diffusion coefficient introduced to minimize noise and to provide numerical stability. We attempted using other advection schemes, for example based on basal slopes, but the level of noise made these approaches unpractical. As such, we make the assumption that the source of individual melt water plumes coincides with the direction of ice velocity. That is, for any given point x on the base of an ice shelf, the grounding line height $z_{gl}(x)$ (i.e. the depth at which the plume originates) associated with that point can be found by following an ice flowline upstream of x to Γ. Note that this does not specify the path the plume takes from $z_{gl}(x)$ to x. The path the plume traverses is a product of the ice-shelf basal slopes, which is acted on by changes in ice shelf thickness along the plume's trajectory. If areas of ice convergence and divergence on a shelf are neglected, we generally expect ice-shelf thickness to decrease as we move from the grounding line to the ice front. Since melt water plumes are driven by buoyancy, it is then reasonable to assume that for small ice shelves, the average trajectory of a plume would be from the grounding line to the ice front. As such, using the ice velocity in the advection scheme to approximate the depth at which the plume originates is not an unreasonable assumption as a first approximation. For larger ice shelves however, sub-shelf flow is impacted by different mechanisms that cannot be captured by a simplified parameterization, such as tides and polynya variability.

In a second step, we correct z_{gl} such that, if z_{gl} is greater than the height of the base of the ice shelf, z_b, then we set $z_{gl} = z_b$. Compared to the algorithm used to determine z_{gl} in Lazeroms et al. (2018), advecting grounding line heights is computationally more efficient for higher resolution model runs because we do not have to search for multiple possible plume sources at every point within a given ice shelf.

Now that z_{gl} is defined, we continue by computing both the characteristic freezing point $T_{f,gl}$

and the effective heat exchange coefficient Γ_{TS} as follows:

$$T_{f,gl} = \lambda_1 S_a + \lambda_2 + \lambda_3 z_{gl} \tag{2.18}$$

$$\Gamma_{TS} = \Gamma_T \left(\gamma_1 + \gamma_2 \, \frac{T_a - T_{f,gl}}{\lambda_3} \times \frac{E_0 \sin\xi}{C_d^{1/2}\Gamma_{TS_0} + E_0 \sin\xi} \right). \tag{2.19}$$

A geometric scaling factor $g(\xi)$ and length scale l are defined in order to give the plume model the proper geometry dependence and scaling according to the distance traveled along the plume path. The scaling factor and length scale are computed as follows:

$$g(\xi) = \left(\frac{\sin\xi}{C_d + E_0 \sin\xi} \right)^{1/2} \left(\frac{E_0 \sin\xi}{C_d^{1/2}\Gamma_{TS} + E_0 \sin\xi} \right)^{1/2} \left(\frac{E_0 \sin\xi}{C_d^{1/2}\Gamma_{TS} + E_0 \sin\xi} \right) \tag{2.20}$$

$$l = \frac{T_a - T_{f,gl}}{\lambda_3} \times \frac{x_0 C_d^{1/2}\Gamma_{TS} + E_0 \sin\xi}{x_0 \left(C_d^{1/2}\Gamma_{TS} + E_0 \sin\xi \right)}. \tag{2.21}$$

The dimensionless scale factor x_0 used in the second term of l defines the transition-point between melting and refreezing and is constant for all model results. For a complete explanation of the individual terms that make up these two factors, see section 2.2 of Lazeroms et al. (2018).

The length scale is then used in the computation of the dimensionless coordinate, $\hat{X}$:

$$\hat{X} = \frac{z_b - z_{gl}}{l}. \tag{2.22}$$

Note that $\hat{X} = 0$ corresponds to the position of the grounding line and $\hat{X} = 0.56$ is the aforementioned transition point, but $\hat{X} = 1$ does not necessarily correspond to the position of the calving front due to the dependence of $\hat{X}$ on l. In order to ensure valid values of $\hat{X}$, we set a lower bound for the ambient ocean temperature: $T_a \geq \lambda_1 S_a + \lambda_2$. The melt rate $\dot{m}$

is then calculated as

$$\dot{m} = \hat{M}(\hat{X}) \times M, \tag{2.23}$$

where $\hat{M}(\hat{X})$ is a dimensionless melt curve expressed as an eleventh-degree polynomial function

$$\hat{M}(\hat{X}) = \sum_{k=0}^{11} p_k \hat{X}^k. \tag{2.24}$$

The values of p_k where $k \in [0\ 11]$ are given in table 2.2 below. Lastly, in order to compute $\dot{m}$ in equation 2.23, we define M as

$$M = M_0 \times g(\xi) \times \left(T_a - T_f\left(S_a, z_{gl}\right)\right)^2. \tag{2.25}$$

For a full derivation of the buoyant plume model used in PICOP, see Lazeroms et al. (2018).

p_{11}	$6.387953795485420 \times 10^{4}$
p_{10}	$-3.520598035764990 \times 10^{5}$
p_9	$8.466870335320488 \times 10^{5}$
p_8	$-1.166290429178556 \times 10^{6}$
p_7	$1.015475347943186 \times 10^{6}$
p_6	$-5.820015295669482 \times 10^{5}$
p_5	$2.218596970948727 \times 10^{5}$
p_4	$-5.563863123811898 \times 10^{4}$
p_3	$8.927093637594877 \times 10^{3}$
p_2	$-8.951812433987858 \times 10^{2}$
p_1	$5.527656234709359 \times 10^{1}$
p_0	$1.371330075095435 \times 10^{-1}$

Table 2.2: Coefficients of the dimensionless melt curve $\hat{M}$, taken from Lazeroms et al. (2018)

.

2.3 Evaluation of melt rates computed with PICOP

We evaluate PICOP using geometry from Bedmap2 (Fretwell et al., 2013) and far field ocean temperature and salinity values averaged at the depth of the continental shelf between 1975 to 2012 (Reese et al., 2018; Schmidtko et al., 2014). Here, we compare the modeled basal melt rates calculated by PICO and PICOP to melt rates inferred from conservation of mass and satellite interferometry (Rignot et al., 2013), that we refer to as "observations". Additionally, we compare the modeled basal melt rate field of select ice shelves to in situ observations and regional modeling studies. We focus on three regions: the Amundsen Sea sector of WAIS, the Totten and Moscow University ice shelves of EAIS, and the Filchner-Ronne Ice Shelf (FRIS). Model inputs for these basins are (0.47°C, 34.73 psu), (−0.73°C, 34.73 psu), and (−1.76°C, 34.82 psu), respectively.

The spatial distribution of melt rates produced by PICOP is in significantly better agreement with observations compared to PICO, especially in the vicinity of the grounding line where accurate melt rates are needed in order to correctly capture the glacier's grounding line dynamics. In figure 2.2, we see that modeled melt rates produced by PICOP reach approximately 100 m/yr and 70 m/yr near the grounding line of Pine Island and Thwaites Glaciers, respectively, as compared to approximately 30 m/yr by PICO. These high melt rates are a product of the deeply entrenched bed that both Pine Island and Thwaites Glaciers are grounded to. These bed depths are advected with the modeled ice velocity when z_{gl} is solved for, resulting in high melt rates that better match observations. Melt rates modeled by Dutrieux et al. (2013), constrained by high resolution satellite and airborne observations of ice surface velocity and elevation, show melt rates on the order of 100 m/yr near Pine Island Glacier's grounding line and 30 m/yr a short 20 km downstream. This sharp gradient in the melt rate field was reproduced by PICOP.

A similar situation occurs under Totten Glacier's ice shelf; melt rates modeled by PICOP

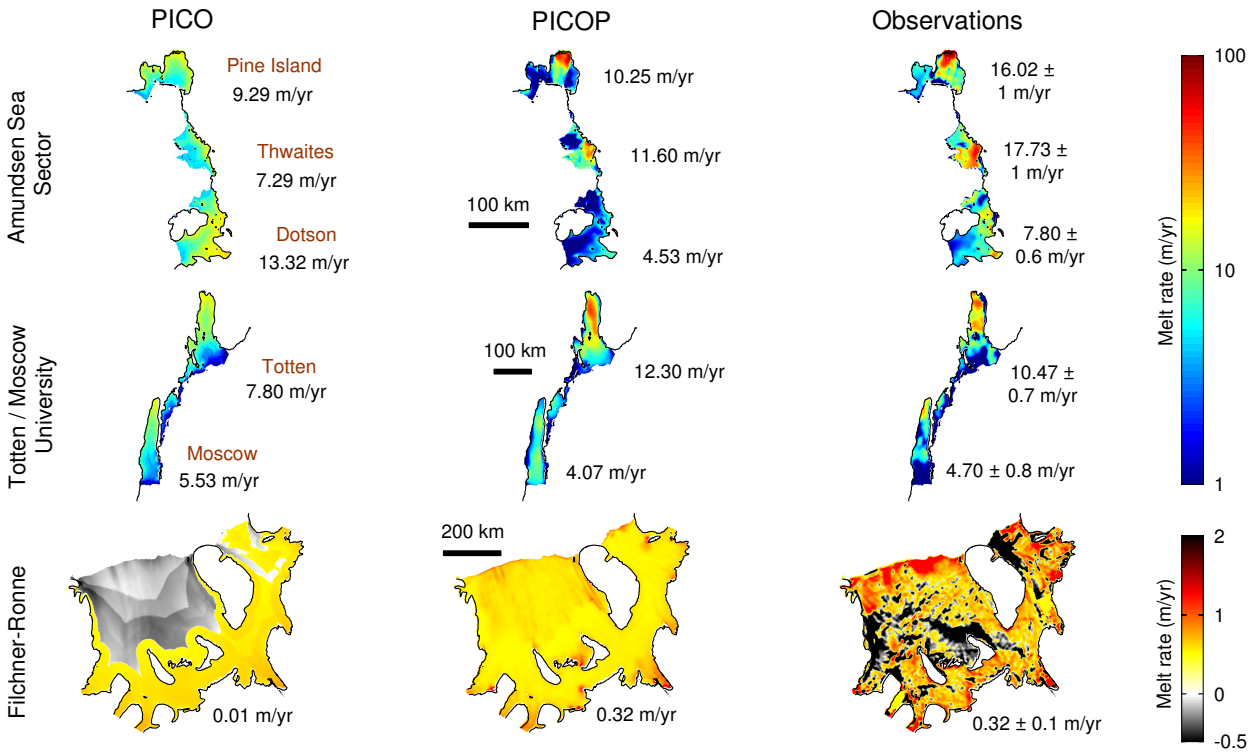

Figure 2.2: Modeled (PICO and PICOP) and observed (Rignot et al., 2013) melt rates (m/yr) are displayed for the Amundsen Sea sector of West Antarctica (including Pine Island, Thwaites, and Dotson ice shelves), Totten and Moscow University ice shelves of East Antarctica, and the FRIS. Note that the upper colorbar (Amundsen Sea sector, Totten, and Moscow University) is in log-form while the lower colorbar (FRIS) is linear. Numerical values under PICO and PICOP are area weighted mean melt rates. The observed annual mean melt rate is displayed under the observed melt rate panel.

reach a maximum of 50 m/yr, while those computed by PICO reach a maximum of approximately 20 m/yr. Simulated melt rates by Gwyther et al. (2014) show a similar pattern of melt, with basal melt rates of approximately 50 m/yr computed near the southern-most portion of both Totten and Moscow University Glacier's grounding lines. Resolving the spatial distribution of melt along this portion of Totten Glacier's grounding line is especially important, as complex patterns of retreat have been observed over the past 17 years and have been found to be sensitive to fluctuations in ocean forcing (Li et al., 2015). Over the FRIS, the inherent geometry dependence of PICOP reduced the "banding" that modeled melt rates from PICO displayed. This is a significant improvement because, as can be seen in figure 2.2, there is a sharp gradient in the simulated melt rate field computed by PICO over the FRIS

that would lead to unrealistic ice shelf dynamics in transient model runs. PICOP produces a smooth transition from high to low melt rates that better matches observations. Basal melting rate fields simulated by coupled ice shelf-ocean models (e.g., Timmermann et al., 2012) show maximum melting (4.5–7 m/yr) near the deepest sectors of the grounding line of Ronne Glacier, agreeing well with PICOP. Site specific observations (e.g., Jenkins et al., 2010) show a decrease in basal melting to less than 1 m/yr near the Kroff ice rise, which is also reproduced by PICOP.

In all three basins, area-weighted mean melt rates calculated with PICOP show better agreement with Rignot et al. (2013). The values reported in figure 2.2 corresponding to PICO differ from those used in figure 5 of Reese et al. (2018) because we model these basins using a significantly higher mesh resolution (minimum element size of 500 m, maximum of 10 km). By modeling Totten, Pine Island, and Thwaites ice shelves with a coarse mesh, only two boxes were defined for these smaller shelves in Reese et al. (2018), and thus, a larger proportion of the ice shelf was modeled as the grounding line box. PICO derived melt rates computed in the grounding line box are the strongest across the ice shelf because the ocean water has not yet lost heat from the influx of cold, ice shelf melt water, leading to higher mean melt rates in Reese et al. (2018) when compared to those displayed in figure 2. By using a finer mesh to evaluate PICOP, we are able to capture the fine details of the melt pattern, which are key in predicting the dynamic evolution of a glacial system, as well as maintain shelf-averaged melt rates that are in relatively good agreement with observations. The mean melt rates for Pine Island and Thwaites ice shelves are underestimated (10.25 m/yr and 11.60 m/yr, respectively), as calculated melt rates are too low away from the plume of strongest melting. In addition, the mean melt rate for Totten ice shelf is slightly overestimated (12.30 m/yr) when modeled with PICOP due to the strong grounding line advection used to compute z_{gl} in this region. Over the FRIS, PICOP models a shelf-mean melt rate that is in better agreement with observations than PICO, because PICOP produces melt further downstream of the grounding line as a result of its geometry dependence. In

this sector of the ice shelf, PICO primarily computes refreezing ($\dot{m} < 0$), which drives the mean melt rate down to 0.01 m/yr.

While PICOP resolves many of the issues displayed in contemporary sub-shelf melt rate parameterizations, it is limited by the assumptions that were made when both PICO and the plume model were originally derived (see Reese et al. (2018) and Lazeroms et al. (2018)). In addition, when computing z_{gl}, we assumed that the depth of the plume origin at any point on an ice shelf could be found by following the flow of velocity upstream to the grounding line. Although a good first approximation, we expect this assumption to fail in zones of complex basal geometry (i.e. areas of convergent and divergent ice flow) that would lead melt-water plumes to follow more convoluted paths. We also expect this assumption to fail in large sub-shelf cavities, such as under the FRIS or Ross ice shelf, where plume paths are influenced by processes not captured by this parameterization (i.e. sea ice and polynya variability, the Coriolis Effect that produces a clockwise sub-shelf ocean circulation, horizontal ocean flow, and tides). Finally, PICOP does not model refreezing well in cold basins due to the lower limit imposed on the ambient ocean temperature. The ocean temperature output from PICO in cold basins (i.e. the FRIS and Ross ice shelf) falls below this lower bound, especially in the vicinity of the ice front, where the coldest ocean temperatures are modeled. As such, melt rates computed in the coldest cavities might be over estimated and cannot be further improved unless this constraint is relaxed, as discussed in Appendix A of Lazeroms et al. (2018). This is exemplified in the modeled basal melt rates produced by PICOP in figure 2.2. Observations show patches of refreezing under the FRIS that are not resolved by PICOP as a result of this lower temperature bound. Yet, PICOP remains an accurate and computationally efficient melt rate parameterization that can be easily implemented into high resolution, transient ice sheet numerical models.

2.4 Summary

Here, we presented a new basal melt rate parameterization that is a combination of both PICO and a plume model. By utilizing PICO to resolve the sub-shelf ocean circulation and produce ambient ocean temperature and salinity fields, we reduce model inputs to only basin-averaged values. Additionally, the spatial distribution and magnitude of melt rates computed with PICOP show improved agreement with observations as a result of the inherent geometry dependence of the plume model. Ocean induced melting has been cited as a major driver of change of Antarctic glaciers and over the coming century, enhanced spreading of mCDW onto the continental shelf is expected as Southern Ocean conditions are projected to change (Dinniman et al., 2012). As such, the improvements to the spatial distribution and magnitude of modeled melt rates produced by PICOP, as well as the computational efficiency of this parameterization, offer a valuable tool to ice sheet modelers seeking to make large scale projections and reconstructions of the Antarctic Ice Sheet.

Chapter 3

ISSM-PICOP coupled simulations of Totten Glacier and the EAIS

In this chapter, we use the newly developed basal melting rate parameterization derived and validated in chapter 2 to make century-scale mass balance projections of dynamic drainage basins in EAIS, including Totten Glacier. Ice sheet mass balance is a major component of the global sea level budget. Fluctuations in mass of the AIS that drive changes in global sea level depend on the balance between mass gain (surface mass balance comprised mainly of inland snowfall) and mass loss (glacial discharge promoted by sub-ice shelf basal melting), the latter of which is primarily driven by interactions of the Southern Ocean with the periphery of the ice sheet. In order to make accurate mass balance projections, it is key to resolve the governing fluxes of ice sheet mass input and output in a dynamic ice sheet model.

To resolve the surface mass balance (SMB), ice sheet modelers generally rely on prescribed SMB inputs, which are typically output fields of Regional Climate Models or Atmosphere-Ocean coupled Global Climate Models (AOGCMs). Resolving Antarctic glacial discharge, however, is challenging because it is largely forced by changes in oceanic heat flux (Rignot

et al., 2013). As such, it is necessary to translate changes in ocean heat content at the bottom of ice shelves to basal melt rates. This remains an active field of study in the ice sheet modeling community and, while ice-ocean model coupling remains the best way to address this question, it is not yet computationally feasible at the scale of EAIS (see chapter 1, Seroussi et al., 2017). Thus, we rely on basal melt parameterizations to simulate ice-ocean interactions in our ice sheet model.

Here, we aim to model mass balance changes of EAIS by 2100 and determine what controls the evolution of its most dynamic catchment. We model six basins in EAIS (hereafter referred to as EAIS_{SUB}) using ISSM (Larour et al., 2012) and three newly developed basal melt rate parameterizations: a non-local quadratic melt parameterization (non-local, Jourdain et al., 2020), the **P**otsdam **I**ce-shelf **C**avity m**O**del (PICO, Reese et al., 2018), and PICO coupled to a buoyant plume model (PICOP, Pelle et al., 2019). We force our model with cumulative anomalies in both SMB and oceanic thermal forcing (TF), taken from six AOGCMs within the Climate Model Intercomparison Project 5 (CMIP5) model ensemble and four AOGCMs from the Climate Model Intercomparison Project 6 (CMIP6) model ensemble. We investigate the modeled response of EAIS_{SUB} mass balance to these given forcings and perform a refined analysis on Totten Glacier, the primary source of mass loss in EAIS_{SUB}. We establish plausible bounds on the contribution of EAIS_{SUB} to global sea level rise by the end of the century and determine the main controls on Totten's mass loss.

3.1 Data and methods

Contemporary EAIS mass loss has been dominated by the signal from the ASB, which contains several marine terminating outlet glaciers (Shepherd et al., 2018). In contrast, Victoria Land, Queen Maud Land, and Amery Ice Shelf have displayed little change over the observational period (Lovell et al., 2017; Rignot et al., 2019). We partition a large sector

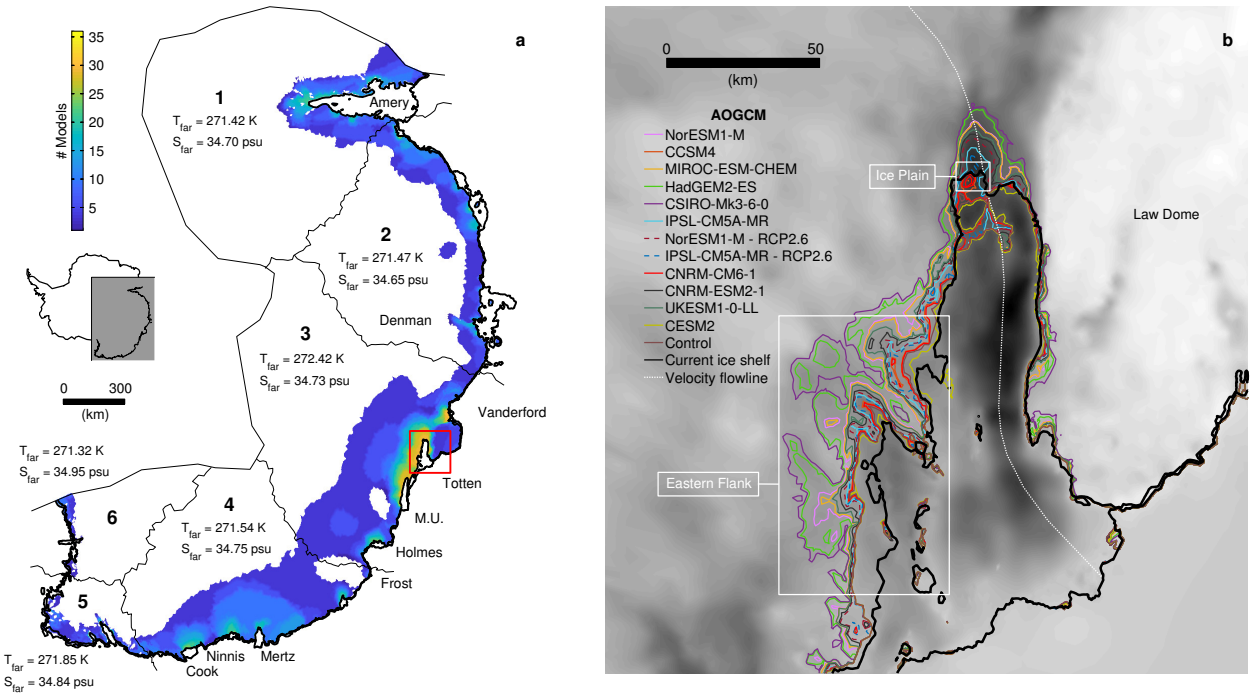

Figure 3.1: (a) $EAIS_{SUB}$ domain showing the number of models (total 36) that predict at least 1 m grounded ice thinning by 2100. Basin outlines are included and the associated far ocean temperature and salinity (used by PICO and PICOP) are displayed for each basin. The red box around Totten Glacier shows the domain of figure 3.1b. The present day grounding line and ice front are overlaid in black (Morlighem et al., 2019). (b) Bed topography (Morlighem et al., 2019) of Totten Glacier with modeled 2100 grounding lines from the forced PICOP projections as well as the control and present day grounding lines. The "eastern flank" and "ice plain" regions are boxed in white and the velocity flowline used in figure 3.8 is included as the white dotted line.

of EAIS into six basins based on Zwally et al. (2012), containing Amery Ice Shelf (basin-1), Queen Mary Land (basin-2), ASB (basin-3), WSB (basin-4), Oates Land (basin-5), and Victoria Land (basin-6, figures 3.1a and 3.2). We exclude the Filchner-Ronne Ice Shelf, Queen Maud Land, and the Ross Ice Shelf from our study due to their current stability (Rignot et al., 2019) and to partition computational resources to more dynamic basins.

We rely on three basal melting rate parameterizations to simulate ice-ocean interactions in our model: non-local quadratic, PICO, and PICOP. The non-local quadratic parameterization aims to resolve the positive feedback between sub-shelf ocean circulation speed and basal melting (Jourdain et al., 2020), capturing both local melt and sub-shelf cavity-

integrated melt (Jourdain et al., 2017). This feedback is crudely represented by multiplying the basin-averaged TF by the local TF, forming a quadratic dependence of the computed melting rate on the TF at the ice-ocean interface. Basin-scale temperature corrections were computed as to minimize the error between parameterized melt rates and those from Rignot et al. (2013). PICO is a two-dimensional box model that was derived to simulate vertical overturning in the sub-shelf cavity, solving the transport of heat and salt between boxes by assuming steady state (Little et al., 2009; Reese et al., 2018). Ocean water, with a given basin averaged temperature and salinity, is entrained into the sub-shelf cavity and melts the ice shelf. The melt water produced is fresh and buoyant, rising along the base of the ice shelf and inducing the strongest melt near the grounding line (see chapter 2.1). Pelle et al. (2019) coupled PICO to a buoyant plume parameterization developed by Lazeroms et al. (2018), forming PICOP. Here, the sub-shelf temperature and salinity fields computed by PICO are used as inputs in the plume emulator, along with the full grounding line depth field. We use the best-fit overturning strength and effective turbulent heat exchange velocity parameters from Reese et al. (2018) in both PICO and PICOP. Overall, these parameterizations were chosen as to vary in complexity and maximize the diversity of resolved sub-shelf ocean processes.

3.1.1 Numerical ice sheet model description

Our ice sheet model of choice is ISSM, a finite element, highly parallelized, thermo-mechanical numerical model of ice flow that is capable of producing high-resolution simulations at the large spatial scale of this study (Larour et al., 2012). We rely on the two-dimensional Shelfy-Stream Approximation for stress balance (SSA, MacAyeal, 1989). A triangular anisotropic mesh with a minimum edge length of 1 km, maximum edge length of 40 km, and comprising 101,700 elements is used to discretize the $\mathrm{EAIS_{SUB}}$ domain (see figure 3.2). We spatially refine the mesh to model Totten Glacier, with a minimum edge length of 500 m, maximum

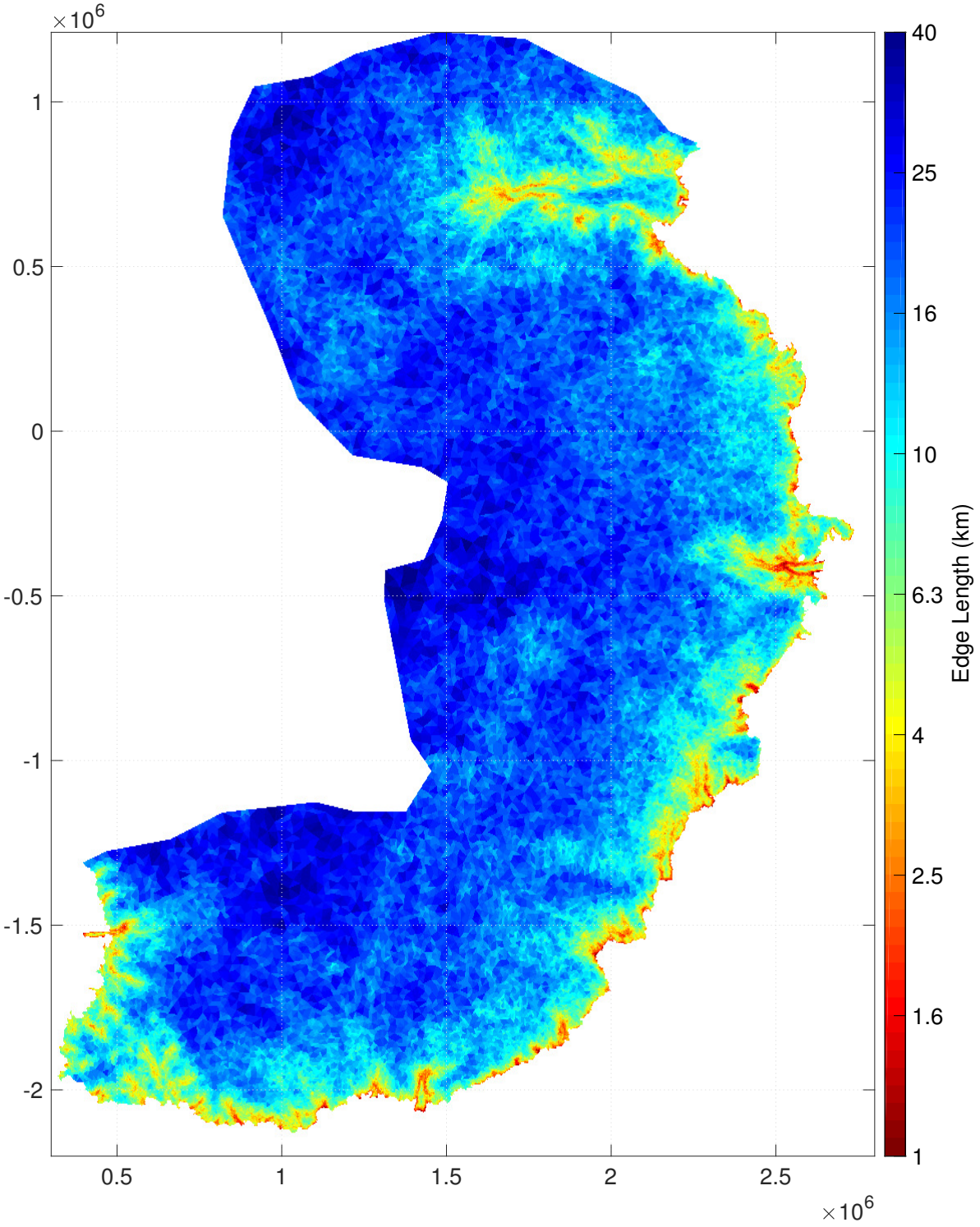

Figure 3.2: Mean edge length (km) of mesh elements within the EAIS_{SUB} domain.

edge length of 10 km, and 132,200 total elements. A two-week time step is used in both the EAIS_{SUB} and Totten Glacier projections. We apply water pressure at the ice-ocean interface. Inflow boundaries are constrained with interferometric synthetic aperture radar (InSAR)-derived surface ice velocities from 2017 (Mouginot et al., 2019b). Thermal boundary conditions are composed of the geothermal heat flux from Maule et al. (2005) and surface temperatures from Lenaerts et al. (2012). We invert for basal friction assuming a Budd friction law (Budd et al., 1979) under grounded ice, and invert for ice viscosity under floating ice using InSAR-derived surface ice velocities (Morlighem et al., 2013; Cuffey and Paterson, 2010; Mouginot et al., 2019b). These fields remain unchanged throughout the duration of the projections. We estimate land ice viscosity by computing ice temperatures based on thermal steady state with 15 vertical layers (Seroussi et al., 2013), using three-dimensional higher-order stress balance equations (Blatter, 1995; Pattyn, 2003), observations of surface ice velocities (Mouginot et al., 2019b), and basal friction inferred from surface elevations (Morlighem et al., 2013). Steady-state ice temperatures are vertically averaged, used as inputs in the ice flow law, and held constant over time. Bed topography is taken from BedMachine Antarctica (Morlighem et al., 2020).

The location of the grounding line is free to evolve in time and is determined through a flotation criterion. A sub-element parameterization is used to track the position of the grounding line within individual elements (SEP2 in Seroussi et al., 2014). In the EAIS_{SUB} projections, the basal friction and basal melting rate fields are scaled by the fractional area of floating ice within partially floating elements, following the SEM1 parameterization from Seroussi and Morlighem (2018). This deviates from the recommendation of this paper due to the coarse spatial resolution of the EAIS_{SUB} mesh, as partially floating elements can extend several kilometers downstream into a given ice shelf. In the finer-resolution projections of Totten Glacier, however, we do not apply basal melting on partially floating elements, as recommended in Seroussi and Morlighem (2018). The ice front is held fixed in all projections, as we are not accounting for ice front dynamics in our model.

3.1.2 Selection of AOGCMs

We force our ice sheet model with yearly output of SMB and TF from six AOGCMs in the CMIP5 model ensemble (CCSM4, MIROC-ESM-CHEM, NorESM1-M, CSIRO-Mk3-6-0, HadGEM2_ES, and IPSL-CM5A-MR) and four AOGCMs in the CMIP6 model ensemble (CNRM-CM6-1, CNRM-ESM2-1, UKESM-0-LL, and CESM2). These datasets were prepared for the Ice Sheet Model Intercomparison Project for CMIP6 (ISMIP6, Nowicki et al., 2016). The AOGCMs chosen to force our ice sheet model incorporate scenarios that range from low to high risk in terms of sea level rise potential, allowing us to develop a diverse range of potential $\mathrm{EAIS_{SUB}}$ mass change scenarios. We force our ice sheet model with yearly output of SMB and TF from six AOGCMs in the CMIP5 model ensemble and four AOGCMs in the CMIP6 model ensemble. In the selection process of Barthel et al. (2019), 33 climate models are rated on their ability to reproduce monthly observations of 850 hPa air temperature, annual precipitable water, annual sea level pressure, summer sea surface temperature, winter sea ice extent, volume averaged ocean temperature, and peak westerly jet strength over the historical period (1979–2005). These atmosphere and surface ocean observations are taken from the European Centre for Medium-Range Weather forecasts "Interim" re-analysis (Dee et al., 2011). Sub-surface ocean observations are taken from a combination of three data sets: the 2018 World Ocean Atlas (Locarnini et al., 2019), the EN4 ocean climatology (Good et al., 2013), and temperature profiles collected by seals (Roquet et al., 2018).

The top six CMIP5 AOGCMs that meet these aforementioned metrics are CCSM4, MIROC-ESM-CHEM, NorESM1-M, CSIRO-Mk3-6-0, HadGEM2_ES, and IPSL-CM5A-MR. The first three AOGCMs represent those models that minimized total bias while maximizing diversity in the given forcing fields. The latter three are chosen as to further increase the diversity in projected forcing (i.e. they represent the spread in the AOGCM results). In addition, four AOGCMs within the CMIP6 model ensemble are selected using the same process: CNRM-CM6-1, CNRM-ESM2-1, UKESM-0-LL, and CESM2. Note that CNRM-ESM2-1

is based on the physical core of CNRM-CM6-1 but additionally includes representations of the global carbon cycle, atmospheric chemistry, and aerosols. For a complete description of the AOGCM selection process, see Barthel et al. (2019).

Model Name	**Atmosphere**	**Ocean**
CCSM4	CAM4	Modified POP2
	$0.9° \times 1.25°$	$0.27 - 0.64° \times 1.125°$
CSIRO-Mk3.6.0	Included	Modified MOM2.2
	$1.875° \times 1.875°$	$0.90° \times 1.875°$
HadGEM2-ES	HadGAM2	Included
	$1.25° \times 1.875°$	$1° \times 1°$
IPSL-CM5A-MR	LMDZ5	Included
	$1.25° \times 2.5°$	$2° \times 0.5 - 2°$
MIROC-ESM-CHEM	MIROC-AGCM	COCO3.4
	$2.8125° \times 2.8125°$	$1.4° \times 0.5 - 1.4°$
NorESM1-M	CAM4-Oslo	NorESM-Ocean
	$1.9° \times 2.5°$	$1.125° \times 1.125°$
CESM2*	CAM6	POP2
	$0.9° \times 1.25°$	$0.27 - 0.64° \times 1.125°$
CNRM-CM6-1*	ARPEGE-Climat	NEMO
	$1° \times 1°$	$1° \times 1°$
CNRM-ESM2-1*	ARPEGE-Climat	NEMO
	$1° \times 1°$	$1° \times 1°$
UKESM-0-LL*	MetUM	NEMO
	$1.15° \times 1.5°$	$1° \times 1°$

Table 3.1: Features of the AOGCMs used in this study. We include the model name, atmospheric component, oceanic component, and the resolution of each respective component. The first six models are from CMIP5, and the last four models denoted with an asterisk are from CMIP6. This table was adapted from Pachauri et al. (2014)

3.1.3 Forcing field anomalies

We force our ice sheet model with anomalies in surface mass balance and oceanic thermal forcing. In general, the computation of forcing field X is dictated by the following:

$$X(x,y,t) = X_{\text{REF}}(x,y) + \left(X_{\text{AOGCM}}(x,y,t) - X_{\text{AOGCM-CLIM}}(x,y)\right) \tag{3.1}$$

Where X_{REF} is the reference forcing field that the anomalies are added to, X_{AOGCM} is the yearly forcing field from a given AOGCM between 2015 and 2100, and $X_{\mathrm{AOGCM\text{-}CLIM}}$ is the mean value of all X_{AOGCM} over the period spanning January 1995 to December 2014.

When computing the SMB forcing field, SMB_{REF} is the present day SMB field from the Regional Atmospheric Climate Model-2 (RACMO 2.3, van Wessem et al., 2014). When computing the TF field, the choice of TF_{REF} is dependent on the basal melting rate parameterization used. For experiments using the non-local parameterization, $TF_{\mathrm{REF}}(x, y)$ is the climatology derived from the three observational ocean data-sets described in section 2.2.2 of Barthel et al. (2019). When using PICO or PICOP, however, the TF field must be simplified to yearly basin-averaged values. As such, $TF_{\mathrm{AOGCM}}(x, t)$ and $TF_{\mathrm{AOGCM\text{-}CLIM}}(x)$ are reduced to area-weighted mean TF values, while $TF_{\mathrm{AOGCM}}(x)$ is composed of the far-field ocean temperatures for basins 6 through 11 in figure 2 of Reese et al. (2018). Note that we hold salinity constant at the values given in Reese et al. (2018) when using PICO and PICOP, as we find it has a negligible impact on the modeled basal melting rates when compared to changes in ocean temperature.

3.1.4 Simulations

Our simulations span the period from January 2015 to December 2100. We force our model with anomalies in SMB and TF, taken from the AOGCMs listed above under the RCP8.5 (CMIP5, Taylor et al., 2012) and SSP585 (CMIP6, Eyring et al., 2016) emission scenarios. We run two additional experiments using forcing fields from NorESM1-M and IPSL-CM5A-MR under RCP2.6 to evaluate the response of our model to lower emission scenarios. We first perform three control runs over $\mathrm{EAIS}_{\mathrm{SUB}}$ for the duration of the aforementioned experimental period to evaluate model drift. One control run is completed for each melting rate parameterization and a ten-year model-relaxation period precedes the start of all simula-

tions, as to allow the model to adjust to initial conditions. For the duration of the relaxation period and control runs, SMB and TF fields are held constant at their respective reference climatology fields. In addition to the $EAIS_{SUB}$ forced simulations, we repeat the experiments on our regional model of Totten catchment using a refined mesh (∼500 m in the grounding zone) to study the response of this glacier's grounding line and ice dynamics to the applied forcings. Mass balance changes are reported relative to the control experiments (i.e. results should be interpreted as the system's response to additional climate forcing compared to the system under forcings representative the period spanning January 1995 to December 2014).

3.2 EAIS simulation results

We observe a varied response of $EAIS_{SUB}$ mass balance through 2100 (figure 3.3). Overall, our CMIP5 RCP8.5 and RCP2.6 projections show that $EAIS_{SUB}$ will gain 9.73 ± 10.05 mm SLRe and lose 1.30 ± 3.35 mm SLRe by the end of the century, respectively. For the CMIP5 forced projections, the standard deviation in $EAIS_{SUB}$ mass balance change associated with choice of AOGCM forcing and melting rate parameterization is 10.29 mm SLRe and 2.37 mm SLRe, respectively. As such, variance in our projections of total mass balance is primarily attributed to the range of AOGCM forcings applied. The standard deviation associated with glacial discharge and total SMB between all CMIP5 experiments is 3.82 mm SLRe and 10.05 mm SLRe, respectively, revealing that significant differences in SMB accumulation between AOGCMs are responsible for the large spread in our projections. Meanwhile, the CMIP6 SSP585 forced models project a mean mass gain of 13.76 ± 5.89 mm SLRe by 2100. The standard deviation in applied SMB and glacial discharge is 5.17 mm SLRe and 2.44 mm SLRe, respectively.

The SMB contribution dominates the total mass balance signal in our model when forced by MIROC-ESM-CHEM, CCSM4, CSIRO-Mk3-6-0, IPSL-CM5A-MR RCP8.5, and all CMIP6

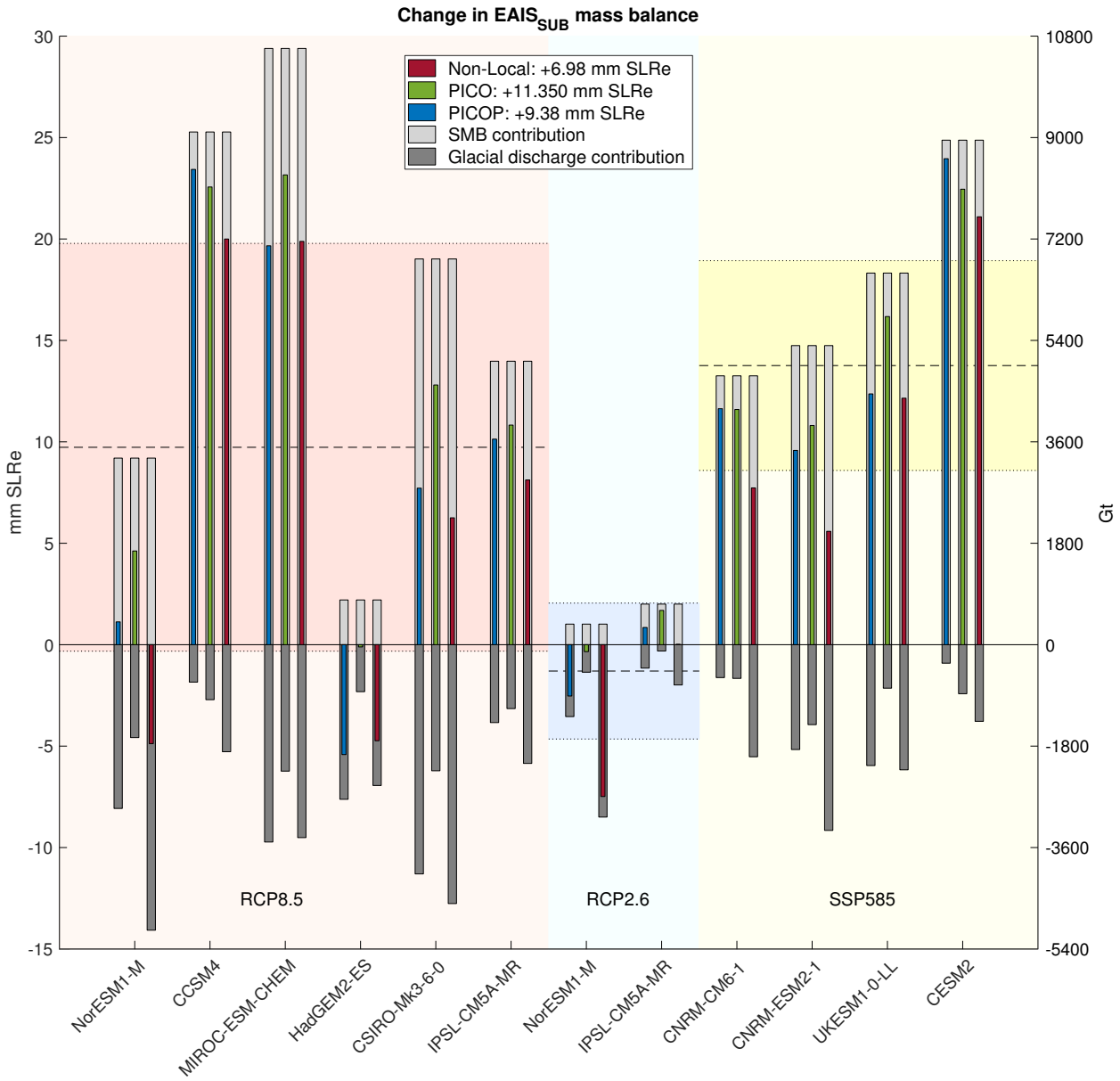

Figure 3.3: Change in total mass balance (blue, green, red bars), SMB (light gray bars), and glacial discharge (dark gray bars) for all 36 simulations in both mm SLRe and Gt (positive-upwards bars indicate $\mathrm{EAIS_{SUB}}$ mass gain, negative-downwards bars indicate $\mathrm{EAIS_{SUB}}$ mass loss). Bars are grouped by AOGCM forcing and color coded by the melting rate parameterization used. Emission scenarios are indicated by background shading: CMIP5 RCP8.5 (red shading, left), CMIP5 RCP2.6 (blue shading, center), and CMIP6 SSP585 (yellow shading, right). Means are plotted for each scenario as a black dashed line and the standard deviation ($\pm 1\sigma$) is visualized as the background shading within the dotted lines. The mean mass balance change per melting rate parameterization is displayed in the legend.

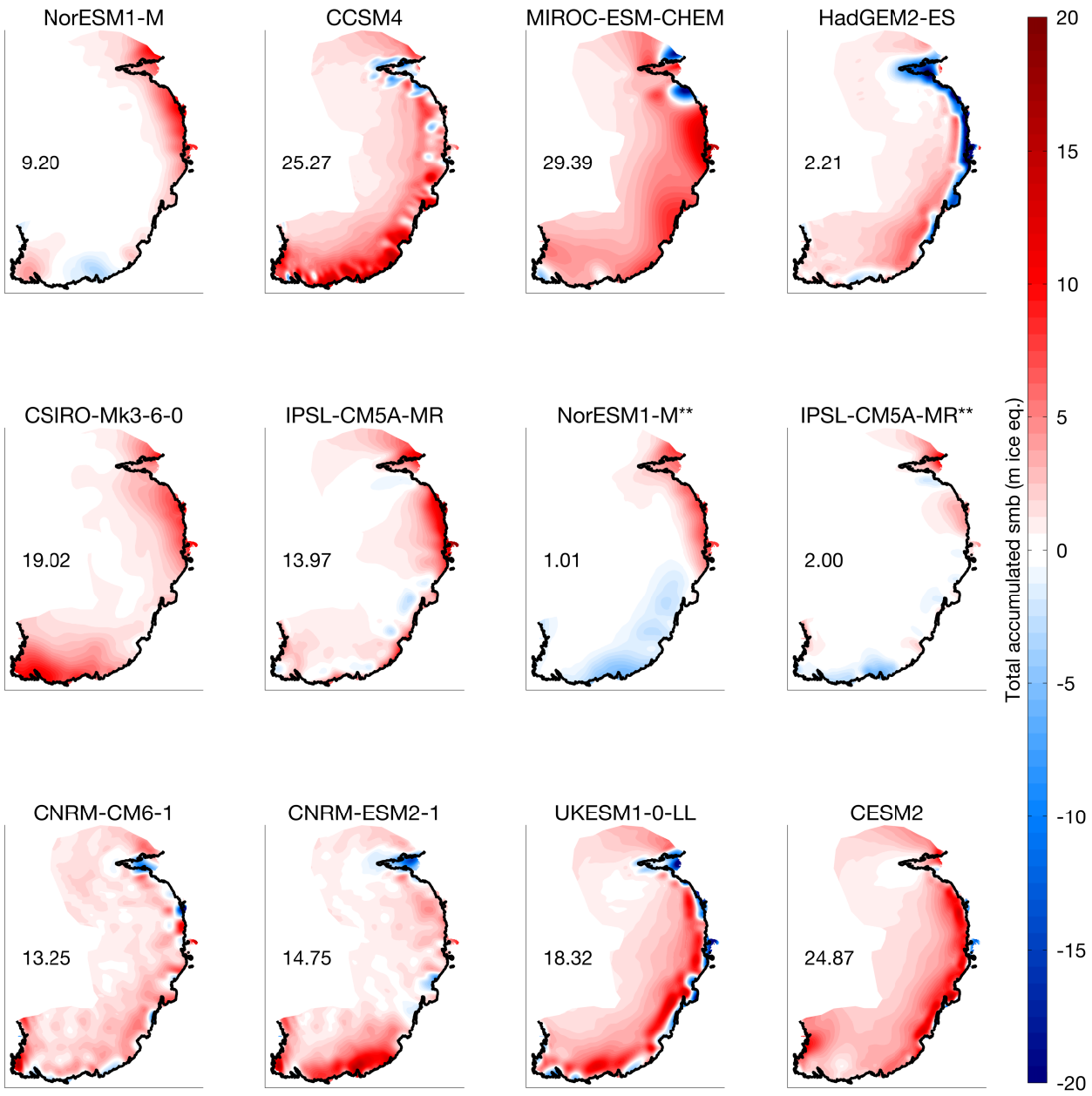

Figure 3.4: Each panel shows the SMB field projected by the given AOGCM summed over the period spanning Jan. 2015 to Dec. 2099, in units of meters ice equivalent. Positive values correspond to SMB gain (red shading), and negative values SMB loss (blue shading). The number in each panel gives the corresponding SMB gain in units of mm SLRe (these are the values that correspond to the light grey bars in figure 2). AOGCM names ending with "**" are under emission scenario RCP2.6.

AOGCMs, leading to substantial mass gains for all melt parameterizations used (figure 3.3). These climate models project between 2.5–3.35°C atmospheric warming over Antarctica by 2100, resulting in significant increases in SMB that are concentrated near coastal sectors (figure 3.4, Barthel et al., 2019). When using forcings from MIROC-ESM-CHEM, CCSM4, and CESM2, the SMB signal is over four times greater than that of the glacial discharge signal and mass gains exceed 20 mm SLRe by the end of the century. When forced by CSIRO-Mk3-6-0, IPSL-CM5A-MR RCP8.5, CNRM-CM6-1, CNRM-ESM2-1, and UKESM-0-LL, total ice mass gains are on average 10 mm SLRe, resulting from the reduced but still significant SMB contribution. In contrast, for the AOGCMs that project less snowfall across $EAIS_{SUB}$ (NorESM1-M, HadGEM2_ES, and IPSL-CM5A-MR RCP2.6), total mass balance changes are largely negative or near-zero and become more dependent on glacial discharge. Our model predicts mass loss when using forcing fields from NorESM1-M RCP2.6 and HadGEM2_ES. Although HadGEM2_ES projects 2.9 K atmospheric warming over Antarctica by 2100 (similar to IPSL-CM5A-MR), reductions in SMB along the coast between Amery and Totten Glaciers offset interior increases, resulting in only 2.21 mm SLRe SMB gain by 2100 (figure 3.4, Barthel et al., 2019). In addition to differences that arise from the applied SMB forcing, we see variation in discharge that arises from the choice of basal melting rate parameterization. When considering the RCP8.5 and SSP585 forced simulations, we find that the use of the non-local parameterization, PICOP, and PICO leads to -7.90 mm SLRe, -5.61 mm SLRe, and -3.54 mm SLRe mean discharge by 2100, respectively (figure 3.3).

A majority of the projected mass loss is isolated to the ASB (basin-3, figure 3.5), while the rest of $EAIS_{SUB}$ either gains mass or remains in near mass balance by the end of the century. In particular, grounded ice thinning is most substantial along the periphery of Totten Glacier's grounding line, with almost all projections showing at least 1 m grounded ice thinning by 2100 (figure 3.1a). Significant mass loss from Totten is observed when forced by NorESM1-M (RCP8.5 and RCP2.6), CSIRO-Mk3-6-0, and HadGEM2_ES. By 2100, these AOGCMs project a shelf-wide mean ocean warming of +0.86°C, +0.23°C, +1.09°C, and

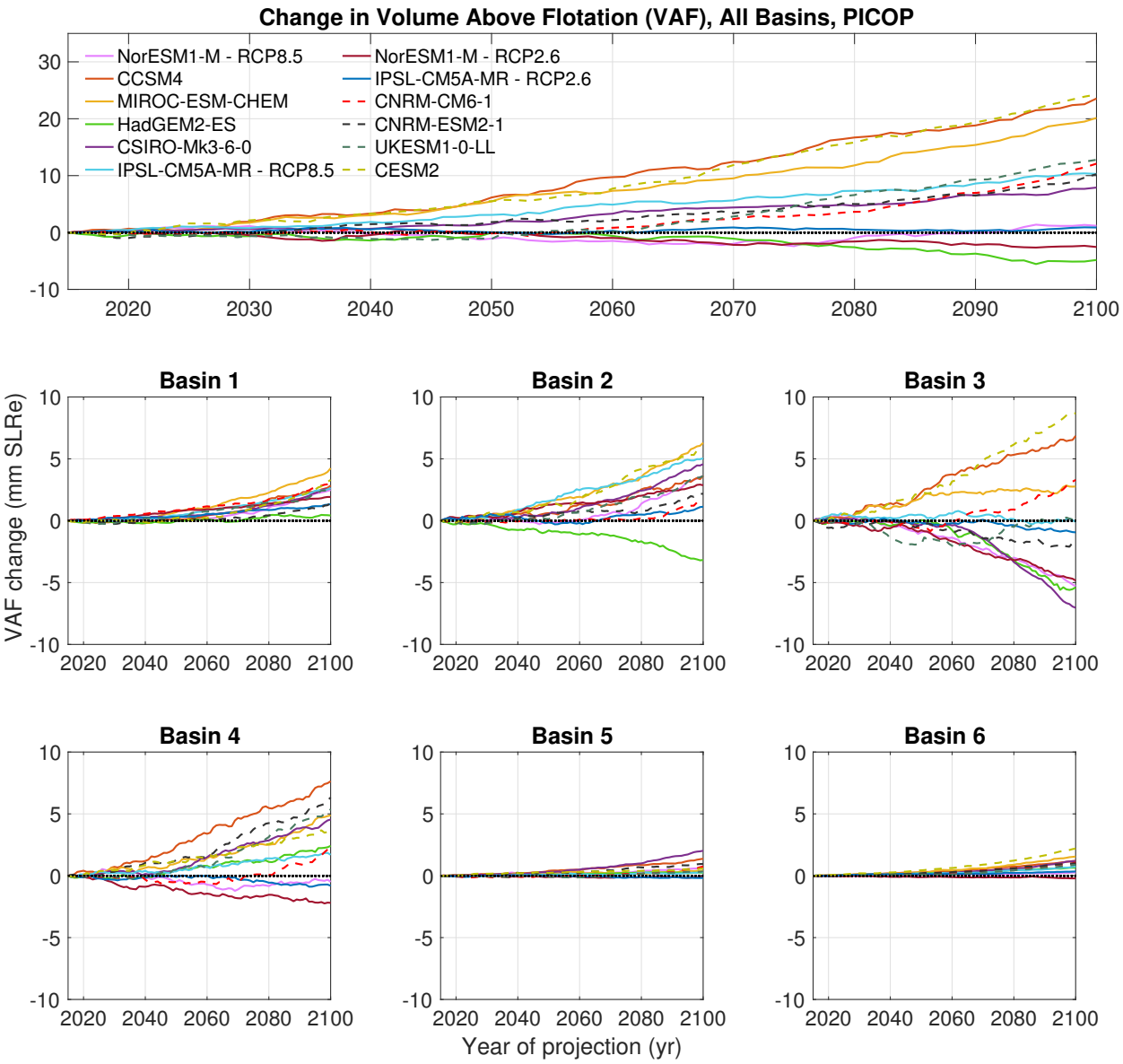

Figure 3.5: (Top) Volume above flotation (VAF) time series in mm SLRe integrated across the entire EAIS_{SUB} domain using the PICOP melting rate parameterization for all AOGCMs. All other subplots show the VAF time series integrated across the individual basins outlined in figure 3.1

+0.86°C, respectively, over the present day average ocean temperature of 272.42 K (figure 3.8m, Reese et al., 2018). While the mean ocean warming projected by NorESM1-M RCP2.6 is minimal relative to other AOGCMs, ice discharge increases significantly after 2040 by an abrupt 0.4°C increase in mean ocean temperature between 2030 and 2040, with minimal projected SMB accumulation to offset the subsequent mass loss (figure 3.8m). Glacial discharge remains constant after 2060 at a rate of approximately 18 Gt/yr, as the sub-shelf ocean temperature remains nearly constant at 272.60 K through 2100 (figure 3.5). Significant ocean warming is also projected by MIROC-ESM-CHEM (+0.86°C with a temporal pattern almost identical to that of NorESM1-M RCP8.5, figure 3.8m); however, large SMB accumulations outweigh the glacial discharge excited by this ocean warming. Our model forced by IPSL-CM5A-MR RCP8.5 and RCP2.6 project Totten to remain in near mass balance through 2100. In the RCP8.5 scenario, we see a significant mean ocean warming of +0.47°C that only results in approximately 1.5 mm SLRe mass loss. This significant ocean warming is projected to occur after 2070, which does not leave enough time for Totten Glacier's upstream grounded ice to fully respond to the subsequent ice shelf thinning. As such, we expect that glacial discharge would accelerate in response to this late ocean temperature increase if we extend our projections beyond 2100.

3.3 Totten Glacier simulation results

We replicated the experiments with a spatially refined mesh (minimum edge length 500 m in and upstream of the grounding zone) on a domain that only contains Totten Glacier to investigate controls on its glacial discharge. We rely on PICOP to compute basal melt rates in these experiments because the spatial distribution and magnitude of computed melt rates matches best with observations (see chapter 2). The ocean temperature is initially set to 272.42 K and evolves in time with anomalies taken from each of the AOGCMs (figure 3.8m).

In figure 3.1b, we observe grounding line retreat along two main sectors of Totten Glacier's grounding line: the eastern flank and southernmost portion ("ice plain"). Retreat along the eastern flank is ubiquitous across all experiments with a maximum inland distance of ∼50 km by 2100. While the distance of upstream grounding line retreat in this sector depends on the ocean temperature applied, the initiation of retreat is temporally uniform and begins immediately in all simulations. The grounding line stabilizes through 2100 along specific topographic highs in this region; however, regions of low-lying bed topography adjacent to these topographic highs are susceptible to melting and allow for ongoing retreat in our simulations under present-day ocean conditions beyond 2100 (figure 3.1b and 3.7, Morlighem et al., 2019).

In contrast, the timing of the initiation of grounding line retreat along the ice plain is dependent on the applied ocean forcing. Figure 3.1b shows that Totten Glacier's grounding line dislodges from this ice plain in every forcing scenario except CCSM4, IPSL-CM5A-MR RCP2.6 (the ice plain only partially dislodges in this projection), CNRM-CM6-1, and CESM2. In all other projections, this region dislodges at various times, occurring as early as 2050 when using forcing fields from HadGEM2_ES. In figure 3.8, yearly velocity profiles are extracted along the flowline from figure 3.1b and are plotted against distance from Totten's ice front. Significant increases in surface ice velocity coincides with the timing of the dislodging of Totten Glacier's upstream ice plain. These velocity increases approach 70% of the initial velocity along the flowline when forced by CSIRO-Mk3-6-0 and extend ∼50 km upstream of the grounding line, caused by the extreme ocean warming projected by this AOGCM (figure 3.8e and 3.8m). The greatest velocity increases are located right along and just downstream of this grounded ice plain, approximately 100 to 150 km upstream from Totten Glacier's ice front. Velocity increases are minimal in both IPSL-CM5A-MR RCP8.5 and NorESM1-M RCP2.6 (figures 3.8f and 3.8g), as the grounding line did not dislodge from the ice plain until approximately 2090, leaving only ten years for upstream, grounded ice to respond. In the projections in which the ice plain did not dislodge, we observe velocity

increases of less than 20% of the initial ice velocity and no distinct period of acceleration.

To test if Totten Glacier's grounding line in the vicinity of the ice plain is susceptible to irreversible retreat via Marine Ice Sheet Instability (MISI, Weertman, 1974; Schoof, 2007), we extend our simulation forced by HadGEM2_ES out to 2140 and set the far ocean temperature to the present-day value of 272.42 K after 2100. We extend the HadGEM2_ES forced projection because Totten Glacier experienced significant ice velocity accelerations under the associated TF profile. We see in figure 3.7 that the grounding line in this projection dislodged around 2070 and by 2100, retreated approximately 25 km upstream. After reducing the ocean temperature at 2100, the grounding line begins to advance slowly downstream as ice shelf thickening begins to take place. As a result, the average percent increase in ice velocity along the flowline decreases from 45% to 34% between 2100 and 2140 (figure 3.6). A majority of this deceleration occurs just downstream of Totten Glacier's ice plain within the first 10 years beyond 2100, highlighting this system's rapid response and sensitivity to decreased TF.

3.4 Discussion

Our projections of future $\mathrm{EAIS_{SUB}}$ mass balance highlight the large degree of uncertainty that exists in projected climate forcings, parameterized physical processes, and the resulting mass balance of this sector over the coming century. The recent IMBIE-2 multisensor assessment found that between 1992 and 2017, EAIS gained 5 ± 46 Gt/yr of ice mass (1.2 ± 11 mm SLRe by 2100 if this trend remains constant, Shepherd et al., 2018). The high degree of uncertainty was primarily attributed to errors in the observed SMB over the observational period. In contrast, Rignot et al. (2019) reported a mass loss of -57 ± 2 Gt/yr (-13.6 ± 0.5 mm SLRe by 2100) from EAIS over the same period using updated regional SMB models. Outlet glaciers in the ASB dominated mass loss in this assessment (e.g. Totten Glacier, which contributes

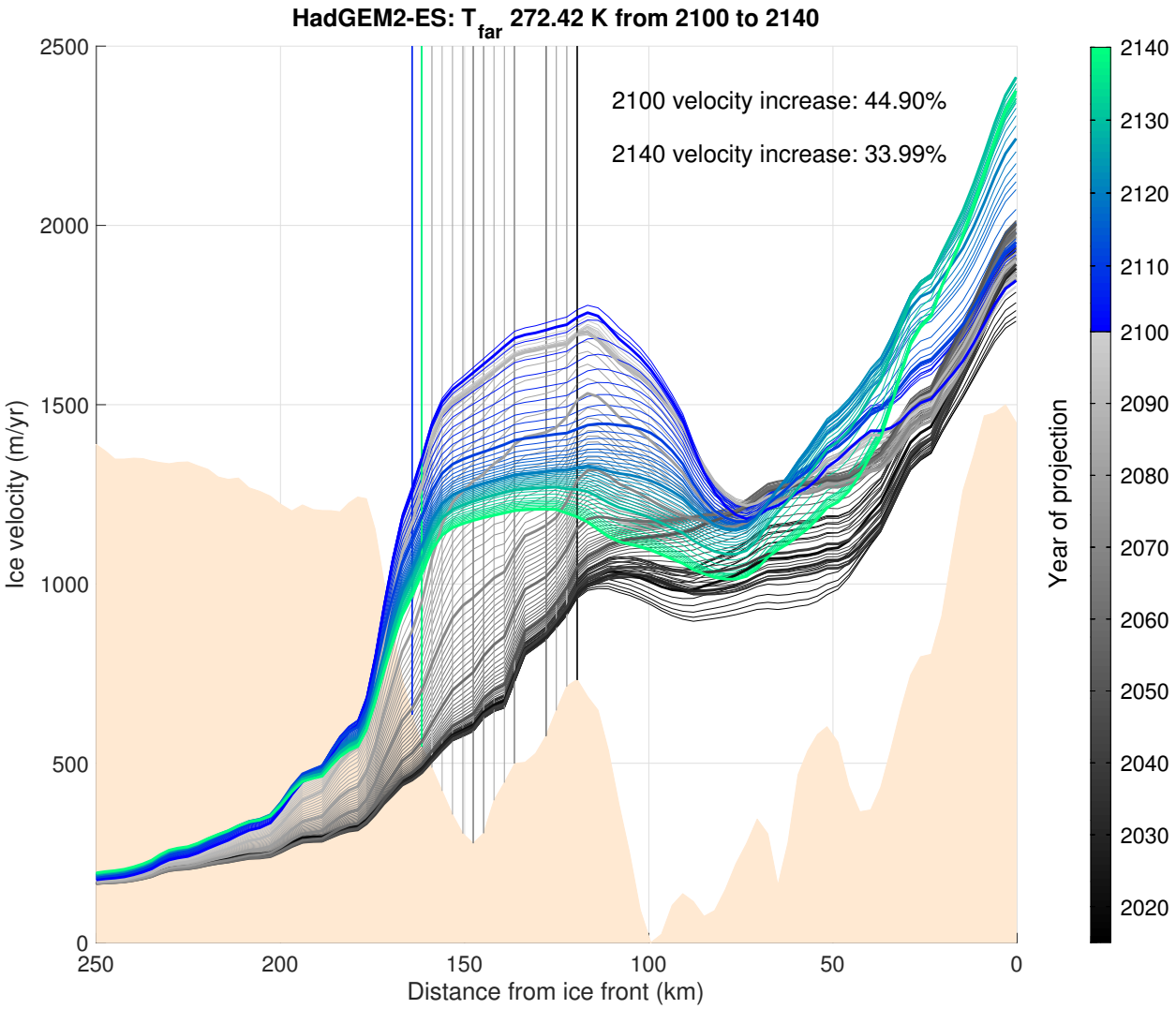

Figure 3.6: Yearly velocity profiles plotted as in figure 3.8 for HadGEM2-ES projected out to 2140. At year 2100, the ocean temperature is decreased to 272.42 K and the model is run forward for an additional 40 years. Velocity profiles from 2015 to 2100 are displayed in gray-scale, while those from 2100 to 2140 are shown in color. The bed topography along the flowline is scaled to the ice velocity and shaded at the bottom of the figure Morlighem et al. (2020).

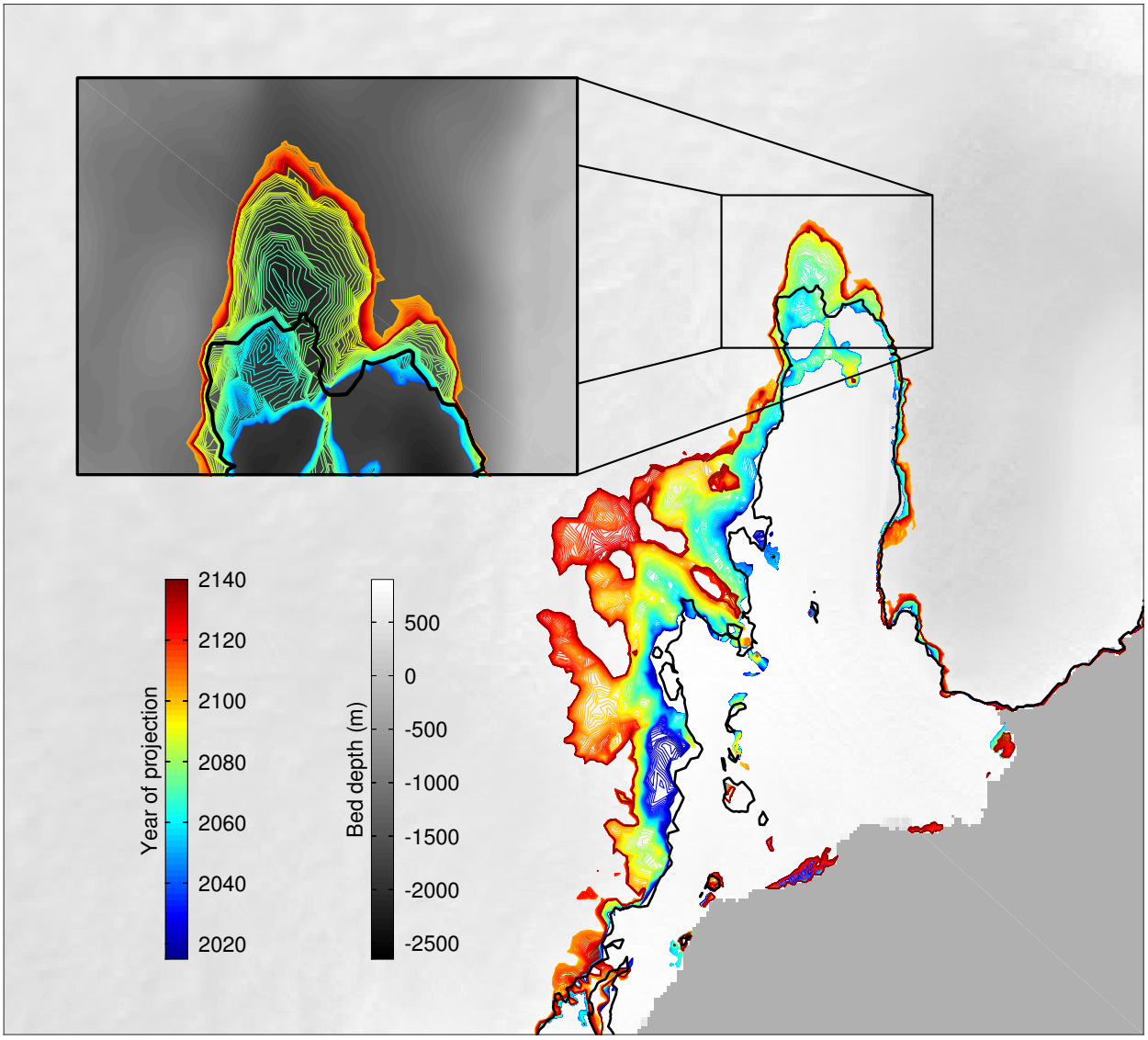

Figure 3.7: Grounding lines plotted each year of the projection for HadGEM2-ES from 2015 to 2140 with the ocean conditions described in figure 3.6. An inset that is zoomed into the ice-plain region of Totten Glacier is displayed in the upper left corner to show grounding line advance in this region. Grounding lines are overlaid onto the bed topography from BedMachine Antarctica Morlighem et al. (2020) in the inset, and over a MODIS satellite image in the main figure.

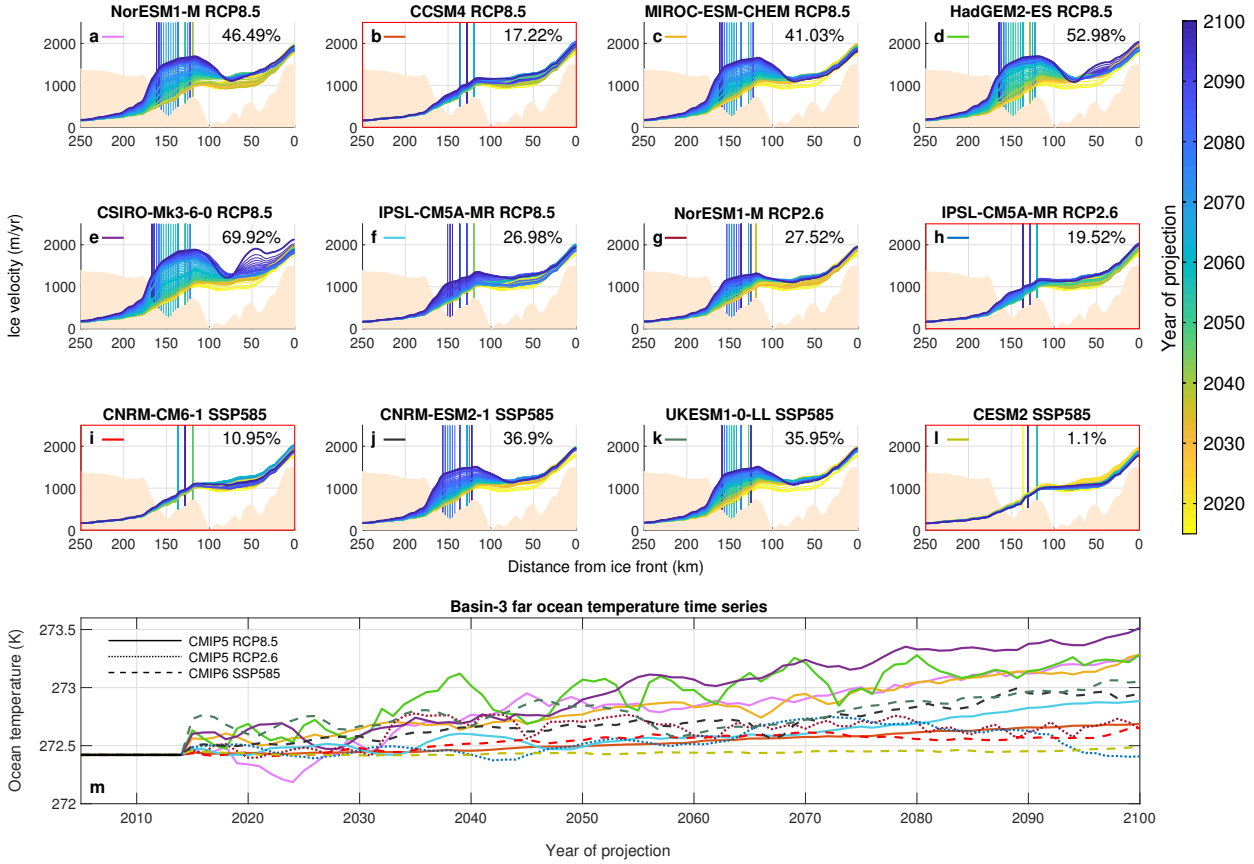

Figure 3.8: (a–l) Velocity profiles (m/yr) taken along the flowline in figure 3.1b are plotted yearly against distance from the ice front (km), with the color of the line coinciding with the year of the projection. Vertical lines correspond to the position of the grounding line along the flowline. The percent velocity increase along this flowline is printed in the top-right corner of each panel. Panels outlined in red display the velocity profiles for projections where Totten Glacier's ice plain did not dislodge. (m) Far ocean temperature time series used as input for PICOP in projections of Totten Glacier. The model relaxation period spans the period from January 2005 to December 2014, in which the far ocean temperature was held fixed at 272.42 K Reese et al. (2018).

approximately 7.3 Gt/yr between 2003–2017, Rignot et al., 2019). Assuming these trends remain constant through 2100, our projections forced by NorESM1-M, CSIRO-Mk3-6-0, HadGEM2_ES, IPSL-CM5A-MR, CNRM-CM6-1, and CNRM-ESM2-1 fall within the error of the IMBIE-2 assessment. In contrast, none of our projections fall within the error bounds of Rignot et al. (2019) due to the overwhelming SMB signal and limited dynamical response of outlet glaciers in both CMIP5 and CMIP6 forced simulations.

Antarctic surface air temperatures are projected to increase by the end of the century in each of the selected CMIP5 and CMIP6 AOGCMs. As such, continent-wide snowfall is expected to increase across Antarctica, as warmer air can hold exponentially more water vapor. Accordingly, projections of Antarctic SMB to 2100 show that if no dynamical ice response is assumed, snowfall is expected to increase by 6–16%, translating to a 20–43 mm drop in global sea level (Ligtenberg et al., 2013). While this response is integrated over the entire AIS, it highlights that significant increases in SMB are a distinct possibility across $EAIS_{SUB}$ by the end of the century. This rationale also clarifies why our model forced by CMIP5 RCP8.5 scenarios gain significantly more mass than when forced with the respective RCP2.6 scenarios, regardless of the melt parameterization used (figure 3.3). Air temperatures increase, on average, $\sim$4°C more in the RCP8.5 scenarios when compared to their respective RCP2.6 scenarios, resulting in an approximate 100% increase in the water vapor capacity of the air. Meanwhile, basin-averaged ocean temperatures increase, on average, $\sim$0.40°C more in the RCP8.5 scenarios, resulting in an approximate 45.5% increase in total integrated basal mass balance when using PICOP. Although both atmospheric and oceanic temperature increases are significant, the ice dynamic response to this enhanced thermal forcing is minimal while the impact of the atmosphere is substantial. As such, it is plausible that, aside from select glaciers in the ASB, large scale $EAIS_{SUB}$ ice dynamics are not particularly sensitive to the increases in sub-shelf ocean temperatures that are projected at the time-scale of this study. Rather, short-term atmospheric changes will govern $EAIS_{SUB}$ mass balance to 2100. Although counter intuitive, this means that lower emission scenarios (RCP2.6) will lead to

greater $EAIS_{SUB}$ mass loss than higher emission scenarios (RCP8.5 and SSP585) by 2100.

In comparing how $EAIS_{SUB}$ mass change varies between projections forced with the same AOGCM output using different melting rate parameterizations, we find that the non-local quadratic melting parameterization generally produces the greatest amount of glacial discharge by 2100, followed by PICOP and PICO. Basal melting rates computed by the non-local parameterization depend on the local and basin-averaged thermal forcing, whereas PICOP takes into account the sub-ice shelf geometry (i.e. the depth of the grounding line and basal slopes). These additional dependencies limit the magnitude of basal melting produced by PICOP beneath ice shelves that are simulated to have high melt rates using the non-local parameterization (figure 3.9). In addition, the spatial distribution of the computed melt rate fields are impacted by these dependencies, driving differences in the modeled patterns of grounding line retreat. In general, melt rates computed by the non-local parameterization are more spatially uniform while those computed by PICOP are channelized, with high melt rates along the plume path and low melt rates elsewhere. These two parameterizations project comparable amounts of total integrated basal mass balance within warm basins. This is exemplified in the NorESM1-M RCP8.5 forced simulation of Totten (figure 3.9), where the non-local parameterization produces high melt across the ice shelf and grounding line that leads to large-scale retreat of the eastern flank. When modeled with PICOP, however, simulated melt rates are high along the interior of the ice shelf, leading to ice-shelf thinning that propagates upstream and dislodges the ice plain. In colder basins where simulated sub-shelf melt rates are low, upstream propagation of this interior ice shelf thinning is slow and does not impact grounding line dynamics as readily as melt applied directly at the grounding line. As such, melt rates produced by the non-local parameterization generally lead to higher amounts of glacial discharge within the time-scale of our study.

In our projections of Totten Glacier, the magnitude of present-day melt rates computed by PICOP agrees well with Gwyther et al. (2014) and Greene et al. (2018), who model

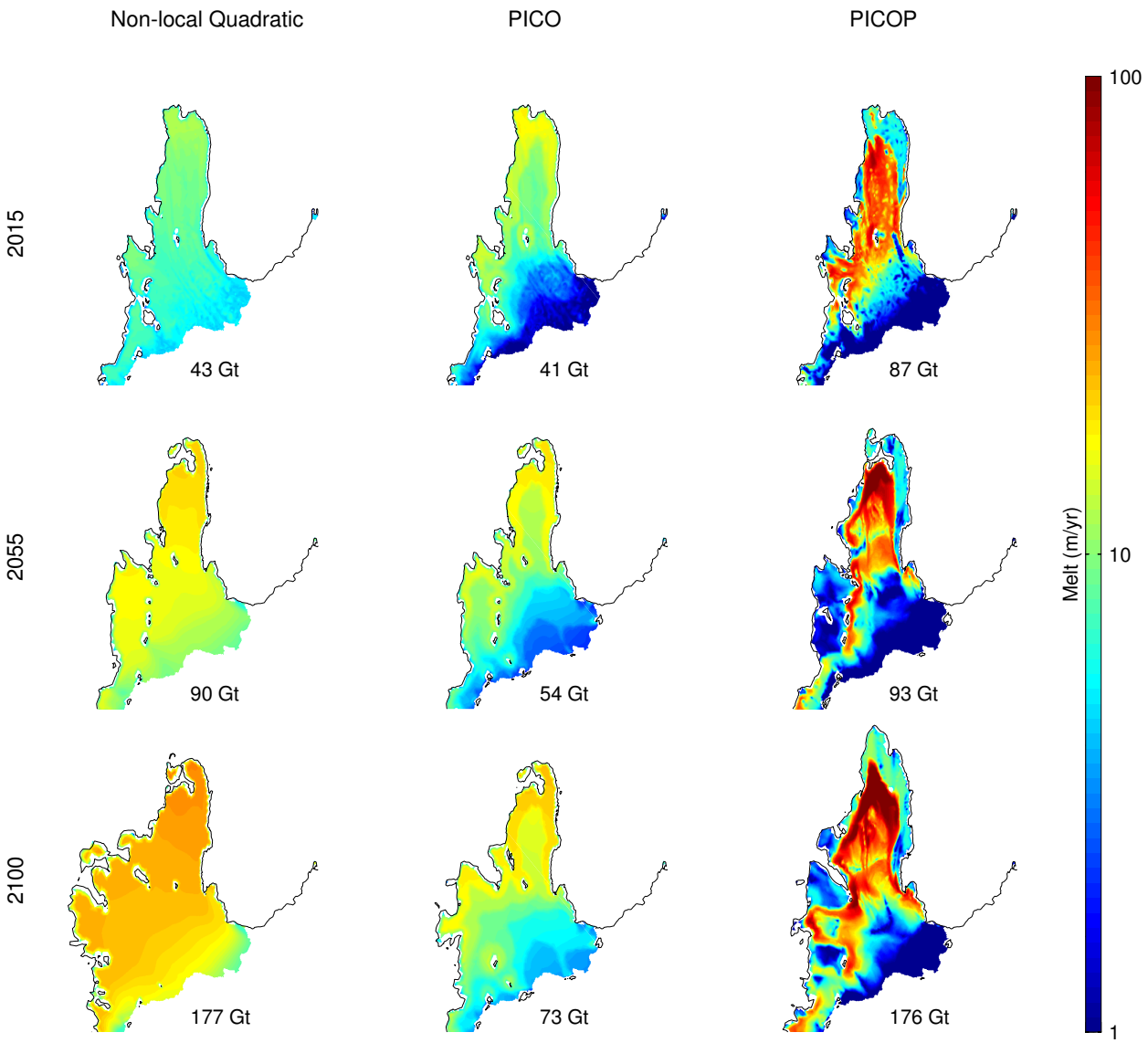

Figure 3.9: Basal melting rate patterns over Totten ice shelf for the non-local quadratic melting rate parameterization, PICO, and PICOP taken at year 2015, 2055, and 2100 of our NorESM1-M RCP8.5 forced simulation. The total integrated basal mass balance (Gt) is displayed in the bottom right corner of each panel for the associated time-stamp.

maximum basal melting rates of 60 to 80 m/yr both along and down stream of the ice plain. Grounded ice thinning along this ice plain varies with the projected magnitude of sub-shelf ocean temperature increase. We observe maximum thinning rates of 2.35 m/yr under the strongest ocean warming scenario (CSIRO-Mk3-6-0), 0.46 m/yr under the weakest ocean warming scenario (CESM2), and a mean thinning rate of approximately 1.15 m/yr that is representative of moderate ocean warming. This mean projection is consistent with Flament and Remy (2012), who observed dynamic thinning near Totten Glacier's grounding line on the order of 1.2 ± 0.6 m/yr, between 2002 and 2010. Our results also agree with ICESat observations between 2003–2008, which measured thinning rates of 1.7 ± 0.2 m/yr in this region (Paolo et al., 2015). Li et al. (2015) observed average thinning rates of 0.7 ± 0.1 m/yr in this region between 1996 and 2013, resulting in a 1–3 km grounding line retreat approaching Totten Glacier's ice plain. Immediately following this retreat, a $10 \pm 5\%$ increase in surface ice velocity was observed along Totten Glacier's main ice stream (Li et al., 2016), agreeing with our findings that this ice plain acts as an important control on ice dynamics. The observed pattern of grounding line retreat in this study is consistent with the findings of Sun et al. (2016), who demarcated widespread retreat over the eastern flank and minimal retreat along Totten Glacier's southern sector, due to the coastal-sloping bed in this region.

In projections with minimal ocean warming (CCSM4, IPSL-CM5A-MR RCP8.5, CNRM-CM6-1, and CESM2), we model grounding line advance downstream of the ice plain, as basal melting rates are too low in this region due to PICOP's plume parameterization (< 10 m/yr compared to 80 m/yr in Greene et al. (2018), figure 3.1b). In the other projections, short term increases in sub-shelf ocean temperature were sufficient to initiate grounding line retreat along Totten Glacier's ice plain (figure 3.1). This is exemplified in the projection forced by NorESM1-M RCP2.6, in which Totten Glacier's ice plain dislodged after ten years of ocean temperatures increased 0.4°C above the present day value of 272.42 K (figure 3.8a, Reese et al., 2018). This present day mean sub-shelf ocean temperature acts as a threshold in our model; warm ocean water intrusion at temperatures above this results in grounding line

retreat past Totten Glacier's ice plain, and temperatures below this result in stabilization. The ability of Totten Glacier's grounding line to readvance during cold water intrusions highlights that at present (i.e. within the plausible ocean temperature range to 2100), Totten Glacier is not susceptible to MISI. During these events, Totten Glacier's grounding line readvances downstream over a 50 km prograde portion of bed topography; however, upstream of this, the bed becomes retrograde towards a deep marine basin adjacent to Law Dome, posing a much more significant threat for MISI. As the ice plain sector drains the majority of Totten Glacier's ice mass, small changes in grounding line position can induce large changes in the rate of grounded ice discharge. Due to the control that this portion of Totten Glacier's grounding line has on the discharge of grounded ice, its inherent sensitivity to brief increases in ocean temperature, and its multi-meter sea level rise potential, scientific focus should remain on this sector of $\mathrm{EAIS_{SUB}}$ through the turn of the century.

In terms of model limitations, the mesh used in our projections of $\mathrm{EAIS_{SUB}}$ is relatively coarse and may not fully resolve grounding line dynamics, which is an important control on glacial discharge (figure 3.2). The spatial scale of this study also requires us to use the two-dimensional Shelfy-Stream stress balance approximation to save computational resources, whereas a three-dimensional model would potentially give us a better approximation of grounding line evolution. For that same reason, we opted to use basal melt rate parameterizations rather than full ice-ocean model coupling to compute sub-shelf basal melting rates. As both the spatial pattern and magnitude of these melt rates have been found to be important to the response of grounded ice discharge, having a more accurate representation of this field would benefit our projections. In addition, the spatial resolution of the AOGCM thermal forcing data is far coarser than most of the ice shelves we are modeling in $\mathrm{EAIS_{SUB}}$ (minimum resolution of 0.90°) and does not include ocean temperature data below ice shelves. Ocean temperatures must be extrapolated into sub shelf cavities, resulting in errors that propagate to the computed basal melting rate fields. We also assume a fixed ice front, whereas ice velocity accelerations have been corroborated with ice shelf destabi-

lization over Cook, Frost/Holmes, Conger/Glenzer, Shackleton, and West glaciers (Rignot et al., 2019). Errors in bed topography, especially in the vicinity of Totten Glacier, may alter our results of the projected timing and extent of grounding line retreat. This would, in turn, impact subsequent projections of future mass balance.

Overall, the projections presented here display a wide range of plausible contributions of $EAIS_{SUB}$ to global sea level rise and target Totten Glacier as the main source of future grounded ice mass loss. Determining which glacier(s) will control future changes in mass loss from such a spatially large region of the Antarctic Ice Sheet is key in steering scientific focus to the most dynamic sectors.

3.5 Summary

In this study, we quantified changes in mass balance of the most dynamic catchments in EAIS in response to a range of oceanic TF and SMB scenarios from both CMIP5 and CMIP6. We employ three different basal melting rate parameterizations to represent ice-ocean interactions in our ice sheet model. Differences in the projected SMB fields lead to a wide range of possible contributions of $EAIS_{SUB}$ to global sea level rise, with an average volume gain of approximately 10 mm SLRe by 2100. Projected increases in SMB dominate the mass balance signal to 2100, leading to $EAIS_{SUB}$ losing more mass under low carbon emission scenarios. All basins within the domain are either in near mass balance or are projected to gain mass by 2100, except the ASB, where the majority of grounded ice thinning occurs within 50 km upstream of Totten Glacier's grounding line. The extent and timing of grounding line retreat along Totten Glacier's ice plain is sensitive to brief changes in ocean temperature. This ice plain acts as an important control of Totten Glacier's glacial discharge. In simulations where this ice plain ungrounds, we observe mean ice velocity increases in excess of 70% of the original velocity profile, compared to less than 20% in the projections

for which this region does not unground. We find that this sector of Totten Glacier is not susceptible to MISI in its current configuration, as the grounding line readvances and velocity profile stabilizes when ocean temperatures are reduced to near present-day values. However, the inherent sensitivity of Totten Glacier's grounding line to short-lived changes in ocean temperature, its control on ice dynamics, and its significant sea level rise potential render observing this glacier a future scientific priority. As approximately 40% of the global population lives within 100 km of the coastline, resolving plausible bounds on the future contribution of EAIS to global sea level within the coming century and discerning which outlet glaciers are most vulnerable is vital in preparing for the impacts of global climate change.

Chapter 4

ISSM-MITgcm coupled projections of Totten Glacier

In the previous chapter, we presented spatially refined, century-scale projections of Totten Glacier using the Ice Sheet and Sea-level System Model coupled to the basal melting rate parameterization PICOP. While PICOP remains one of the most accurate parameterizations of basal melting that can be used in transient ice sheet models, it is unable to resolve many key ice-ocean processes that govern the spatial distribution and magnitude of observed basal melting. For example, the horizontal scale of the water column underlying Antarctic ice shelves is orders of magnitude greater than the vertical scale; yet, PICOP can only resolve the magnitude of the sub-shelf vertical overturning circulation. The horizontal circulation of ocean water beneath an ice shelf dictates the location of vertical overturning and the trajectory of mCDW around topographic barriers and through the sub-shelf cavity, both of which are primary controls on the spatial distribution of ice shelf basal melting. Furthermore, PICOP was forced with yearly anomalies in oceanic thermal forcing that was obtained from averaging the output of select CMIP5 and CMIP6 AOGCMs in front of Totten Glacier's ice shelf. Averaging the thermal forcing over the period of a year smooths over seasonal

variations in oceanic thermal forcing. In addition, the grid resolution of the AOGCMs (typically 50-100 km) in which forcing fields were taken from is too coarse to resolve most Antarctic ice shelf cavities and cannot resolve smaller-scale circulation features that transport mCDW onto the continental shelf (i.e. flow around complex bathymetry). As such, if we seek to make detailed projections of the future dynamic evolution of Totten Glacier and pinpoint the main sources of dynamic change (rather than make mass balance projections), we need to have a more complete representation of the Southern Ocean in our ice sheet model.

In this chapter, we model the dynamic response of Totten Glacier and surrounding glaciers (Moscow University and Vanderford, figure 4.1) to realistic 21st century ocean forcing. We couple the finite element Ice-sheet and Sea-level System Model (ISSM, Larour et al., 2012) to a regional East Antarctic configuration of the Massachusetts Institute of Technology general circulation model (MITgcm, Marshall and Clarke, 1997; Nakayama et al., submitted) and run projections through 2100. We force the ocean model at its boundaries with anomalies in ocean temperature, salinity, and velocity, taken from four CMIP6 global climate models under high and low emission scenarios (Eyring et al., 2016). We first describe the set-up of ISSM, MITgcm, and the methodology used to couple these models. We then detail the experimental setup and discuss results pertaining to both the short-term and long-term dynamic response of Totten Glacier.

4.1 Data and Methods

4.1.1 Numerical ice sheet model description

The ice sheet model domain spans the region from Moscow University Glacier (M.U.) to Underwood Glacier and extends inland to the ice-divide (figure 4.1). We use an anisotropic mesh to discretize the domain, consisting of 82,418 horizontal elements that vary in size

between 1 km in fast-flowing regions to 20 km in regions of stagnant flow. A two-week time-step is used to satisfy the Courant-Friedrichs-Lewy condition.

We implement the two-dimensional Shelfy-Stream stress balance approximation of the Stokes equations (MacAyeal, 1989). Static inversions of interferometric synthetic aperture radar (InSAR) derived surface ice velocities from 2017 are performed to initialize our model with basal friction under grounded ice and ice viscosity for floating ice (Mouginot et al., 2019b; Morlighem et al., 2013). Basal friction is solved for assuming a Budd sliding law (Budd et al., 1979) and grounded ice viscosity is computed assuming an ice temperature of -10°C using the table provided by Cuffey and Paterson (2010). Both fields remain fixed throughout the projections. We apply water pressure at the ice-ocean interface, a stress-free boundary condition at the ice-air interface, and constrain inflow boundaries with InSAR-derived surface velocities (Mouginot et al., 2019b). Bed topography is taken from BedMachine Antarctica (Morlighem et al., 2020) and the present-day surface mass balance field is from the Regional Atmospheric Climate Model-2.3 (RACMO 2.3, van den Broeke, 2019).

We use a flotation criterion to determine the position of the grounding line in our model simulations. The precise location of the grounding line within individual elements is tracked using the "SEP2" sub-element grounding line migration parameterization, in which basal friction is integrated only over the grounded portion of an element (Seroussi et al., 2014). Basal melting is applied only to elements that are completely floating, as to follow the recommendations of Seroussi and Morlighem (2018). The ice front remains fixed in all projections.

4.1.2 Numerical ocean model description

We use a regional East Antarctic configuration of the MITgcm, developed by Nakayama et al. (submitted), to provide ocean forcing to our ice sheet model. The ocean model domain

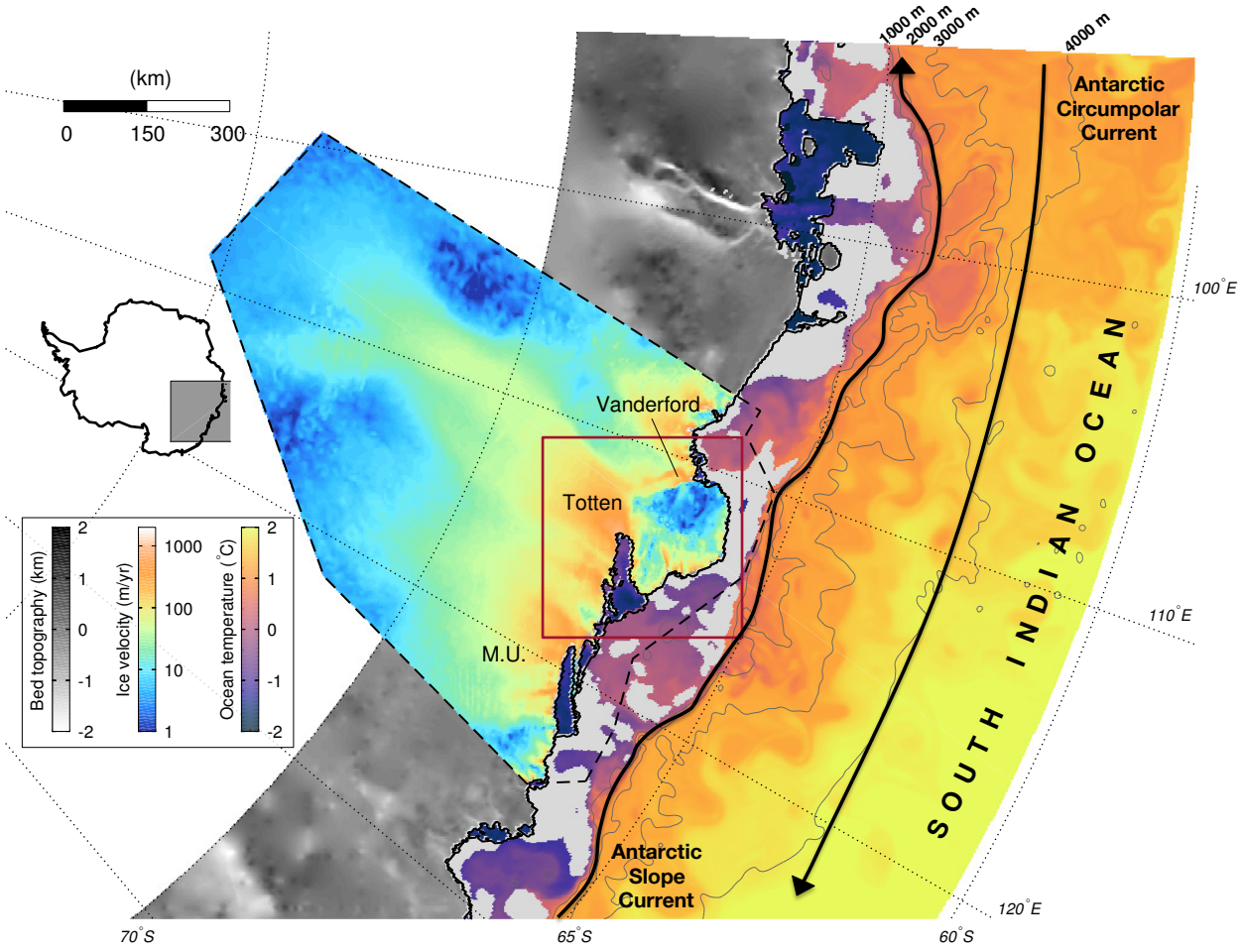

Figure 4.1: Domains for the ocean and ice sheet models (the ocean model domain extends to 150°E). The simulated 490 m ocean potential temperature (°C) on January 1, 2017 is plotted in the ocean model domain over open ocean (gray shading are oceanic regions above 490 m). Beneath ice shelves, the ocean temperature of the grid cell immediately below the ice is plotted. Bathymetric contours of 1000, 2000, 3000, and 4000 m are overlaid in gray. Black arrows denote approximate locations of the Antarctic Slope Current and Antarctic Circumpolar Current. Surface ice velocity (m/s) is plotted in the ice sheet model domain over grounded ice (outlined in the dashed black line, Mouginot et al., 2019a). Bed topography is shaded in gray-scale over grounded ice outside the ice sheet model domain (Morlighem et al., 2020). The red box around Totten Glacier outlines the domain of figure 4.7.

spans 90–150°E in longitude, 60–70°S in latitude, has horizontal grid spacing of 3–4 km, and contains 70 vertical levels. The Antarctic Circumpolar Current is located in the deep waters carrying mCDW eastward, while the Antarctic Slope Current (ASC) flows westward along the continental slope following the isobaths of ∼500–1500 m (figure 4.1). Sea ice is resolved with the use of a dynamic/thermodynamic sea ice model (Losch et al., 2010) and sub-ice shelf basal melting is parameterized as a function of thermal driving stress and friction velocity at the ice-ocean interface (Losch, 2008; Hellmer and Olber, 1989; Holland and Jenkins, 1999; Jenkins, 1991). Bathymetry below floating ice is taken from Morlighem et al. (2020) and from ETOPO1 over open ocean (National Geophysical Data Center, NESDIS, NOAA, U.S. Department of Commerce, 2011), with recent updates of more accurate bathymetry for the region on the continental shelf off Totten Glacier's ice shelf from Rintoul et al. (2016). Model parameters are taken from Nakayama et al. (submitted), unless noted table 4.1.

Oceanic and atmospheric boundary conditions are derived from the climatology of the ECCO LLC270 project (Zhang et al., 2018) and ERA-Interim (Dee et al., 2011), respectively, between 1992–2016. Ocean model initial conditions are generated from a 25-year spin-up (1992–2016), which was initialized from a rest-state with temperature and salinity datasets from the World Ocean Atlas at January 2009 (Locarnini et al., 2010; Antonov et al., 2010). As multi-year variability was evident in the melt rates produced in the spin-up run, we repeat the full 25-year forcing in the coupled projections.

Parameter	Value
Air/sea ice drag coefficient	0.00075
Ice/ocean drag coefficient	0.0035
Lead closing (m)	1.5

Table 4.1: Ocean model parameters that are used in this study that are different from (Nakayama et al., submitted).

4.1.3 Coupling scheme

We couple ISSM and MITgcm asynchronously through a MATLAB interface following the methodology of Seroussi et al. (2017). We first run the MITgcm forward for two weeks to obtain the time-averaged basal melting rate field, which we use to force ISSM. ISSM is then run for two weeks and provides the MITgcm with an updated ice shelf draft. In areas where the grounding line and/or ice shelf retreated and new ocean grid cells are created, both the temperature and salinity profiles of the nearest cell are extrapolated into the newly opened cells. All other fields from the previous integration remain unchanged and are used to initialize the next two-week model run. Note that because we operate the ice sheet model and ocean model on different grids, information is bilinearly interpolated between the two models in the MATLAB interface.

4.1.4 Experimental description

We force the MITgcm at the northern, eastern, and western boundary with changes in salinity, temperature, and velocity following low and high emission scenarios from four CMIP6 global climate models: CNRM-CM6-1, CNRM-ESM2-1, UKESM1-0-LL, and MIROC-ES2L (selected following ISMIP6 model selection protocol, Nowicki et al., 2020). At each grid cell along a given boundary, we compute the linear rate-of-change of the selected field through time for each of the four CMIP6 models. We then take the CMIP6-model mean of these rate-of-change fields along each boundary, resulting in averaged fields that we refer to as "anomalies" (figures 4.2–4.5). The climatology of the ECCO-derived ocean boundary conditions serve as the base-field upon which these anomalies are applied, constructing our experiments.

We perform three coupled experiments: **1.** CTRL: no change applied to the ocean boundaries, **2.** SSP126: low emission anomalies applied to ocean boundaries, and **3.** SSP585:

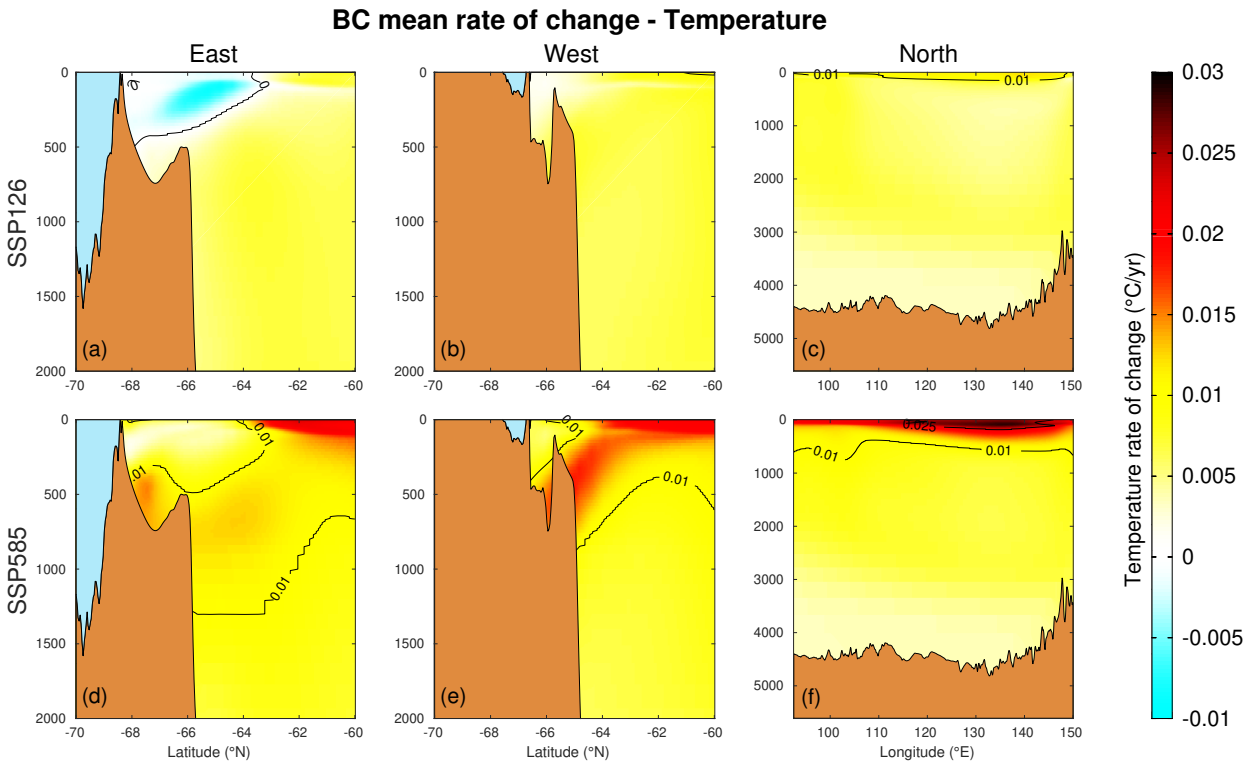

Figure 4.2: The CMIP6 derived linear rate of change of ocean potential temperature (°C/yr) at the east (a,d), west (b,e), and north (c,f) ocean boundaries are displayed for experiments SSP126 (a,b,c) and SSP585 (d,e,f). Note the different x- and y-axes (depth in meters) for the northern boundary plot. Bed topography from Morlighem et al. (2020) is shaded in brown and land-ice is shaded in light blue.

high emission anomalies applied to ocean boundaries. Lastly, we run three uncoupled simulations (denoted with a subscript "u", e.g. CTRL_u) using the PICOP basal melting rate parameterization (Pelle et al., 2019) forced with MITgcm output temperature and salinity, as to facilitate a comparison of Totten Glacier's evolution in response to simulated versus parameterized ocean forcing.

Given the large degree of uncertainty stemming from large-scale climate change projections and that we do not couple MITgcm to a dynamic atmospheric model, we do not intend to predict exact dates of change in the analysis below. Rather, our simulations stress the sensitivity of Totten Glacier to simulated changes in ocean forcing and how the system is likely to evolve in the future.

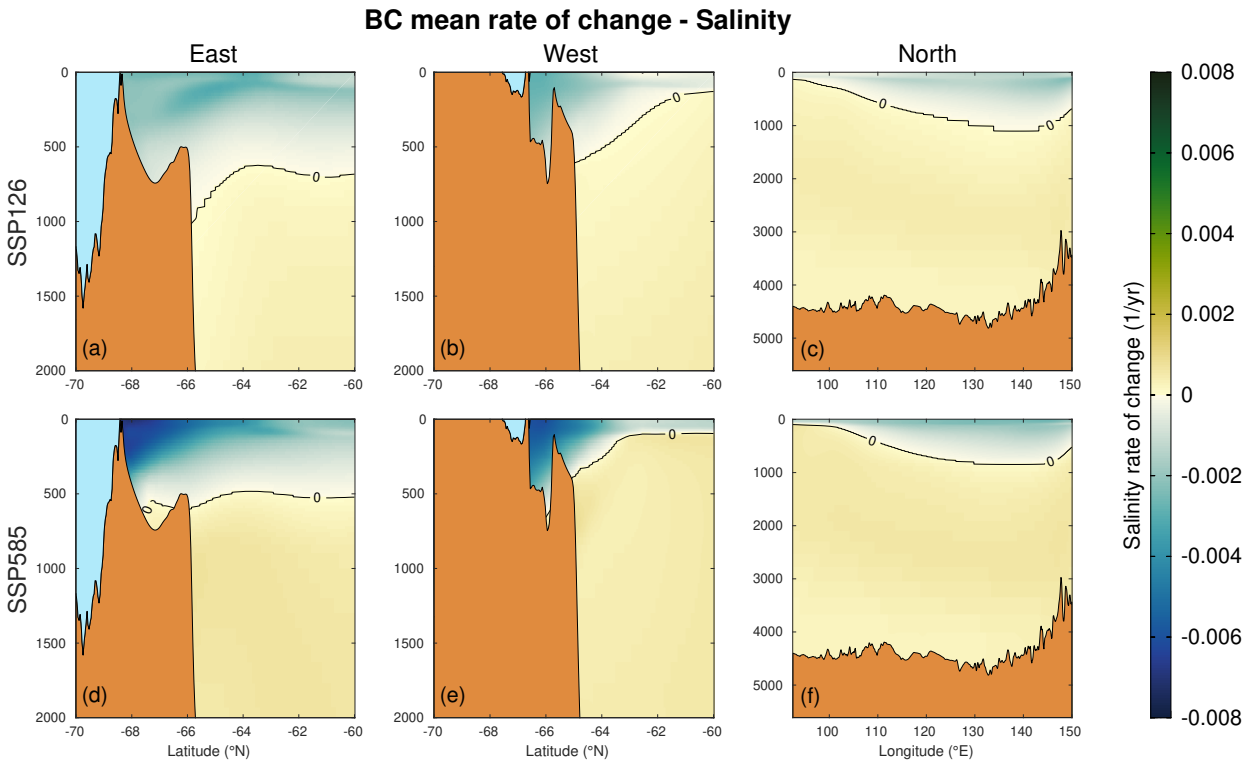

Figure 4.3: Same as figure 4.2, but showing the rate of change of ocean boundary salinity in units of yr^{-1} on the Practical Salinity Scale.

4.2 Results

Along the ocean boundaries, we observe minimal change in the CMIP6 projected ocean state under SSP126 in all CMIP6 models (figures 4.2–4.5). In contrast, under SSP585, warming of the upper 500 m of the ocean is observed at all boundaries north of 65°S (maximum of 0.025°C/yr, 2.08°C by 2100, figure 4.2). Surface warming is particularly strong in UKESM1-0-LL and CNRM-CM6-1, exceeding 0.03°C/yr at the northern model boundary. Surface ocean freshening of 0.006 yr^{-1} to a total of 0.50 by 2100 on the Practical Salinity Scale is projected under SSP585 in all CMIP6 models at the eastern and western boundaries (figure 4.3). This freshening decreases with distance away from the ice sheet, as it is a product of enhanced ice shelf melting parameterized within the CMIP6 models. In the CMIP6 projected velocity field, increased westerly flow is observed along the continental slope, demarcating weakening of the westward flowing ASC under both SSP126 and SSP585 in all CMIP6

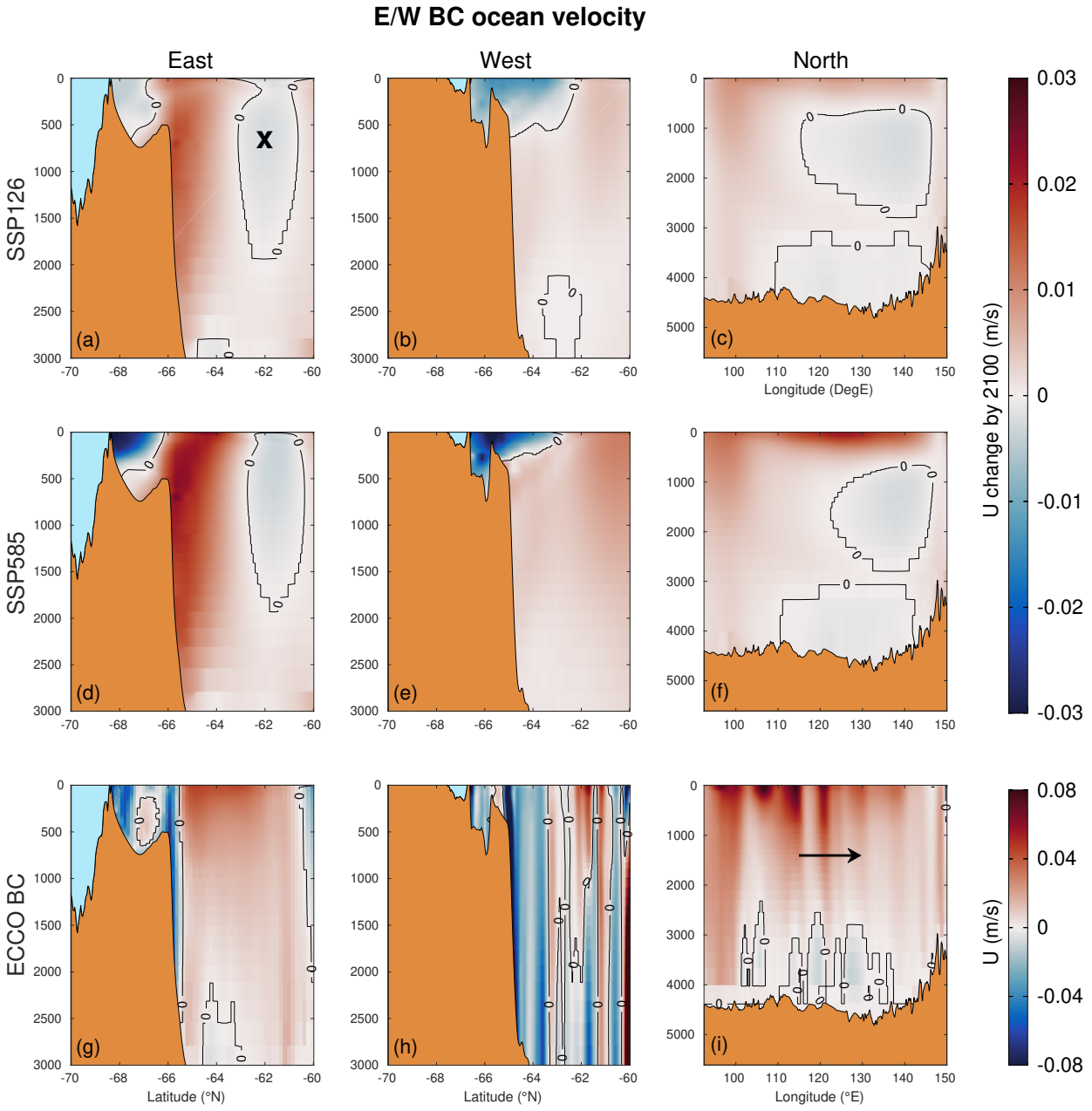

Figure 4.4: **(a-f)** Total change in CMIP6 derived eastward velocity (m/s) by 2100 at the east (a,d), west (b,e), and north (c,f) ocean boundaries are displayed for experiments SSP126 (a,b,c) and SSP585 (d,e,f). Note that the bold "x" refers to ocean flow into the page. (**g-i**) Snapshot of ECCO derived eastward ocean velocity at the start of the simulation along the east (g), west (h), and north (i) ocean boundary. The arrow in panel-i refers to the approximate direction of flow.

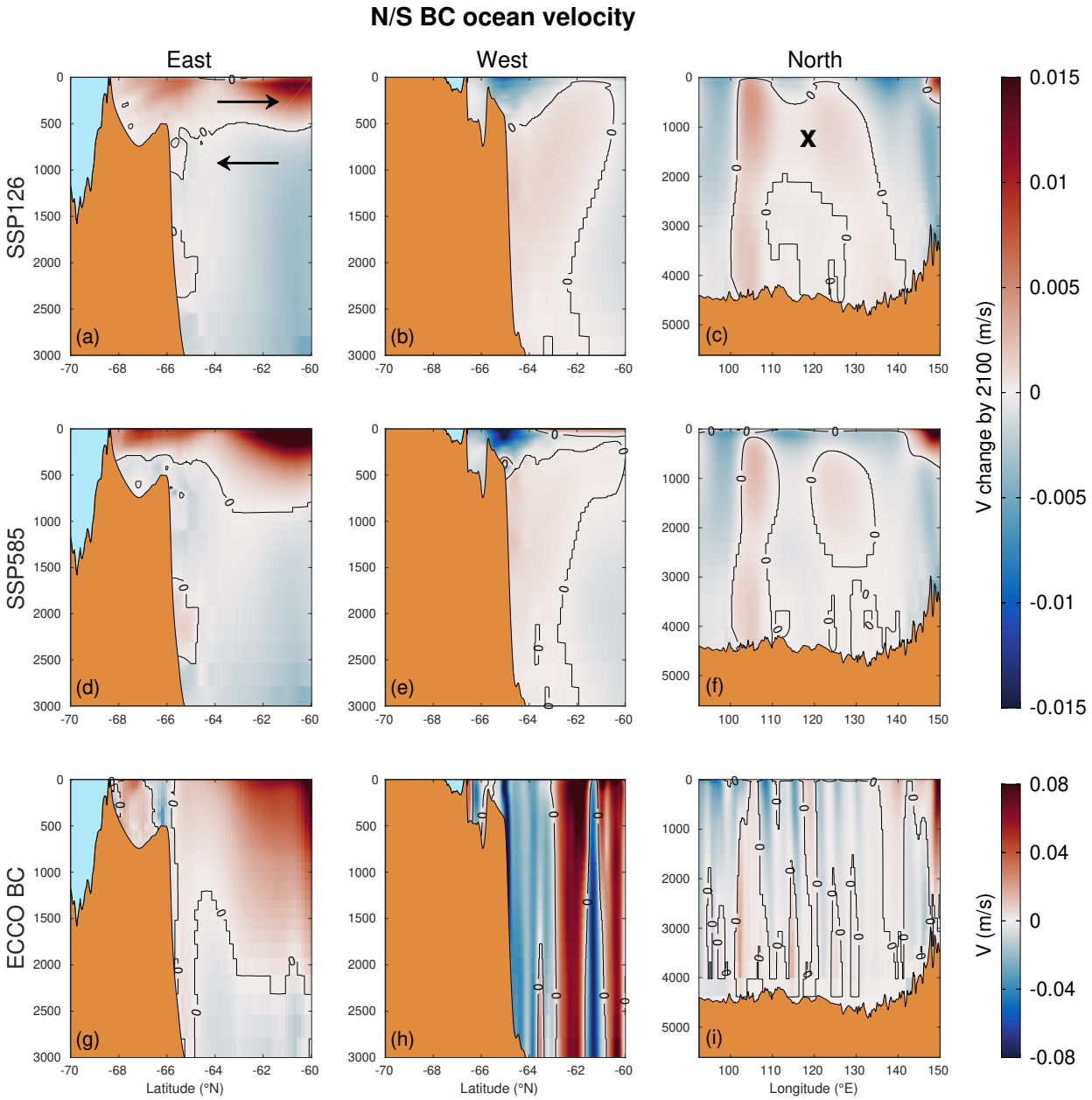

Figure 4.5: Same as figure 4.4, but showing the rate of change of northerly ocean boundary velocity (m/s). Note the change in the color bar limits from figure 4.4.

models except MIROC-ES2L (figure 4.4). By 2100 under SSP585, the ASC weakens by ∼37.5% relative to its present-day state.

In figure 4.6a, we observe that the total basal mass balance remains nearly constant at ∼75 Gt/yr in all experiments until 2040, after which the ocean forcing in SSP585 begins increasing relative to CTRL and SSP126. By 2100, the total basal mass balance in SSP585 is ∼2.3 times greater than that of SSP126, increasing from 74 Gt/yr to 169 Gt/yr. In contrast, the mean ocean forcing in CTRL and SSP126 remains nearly constant at 75 Gt/yr throughout the simulations. The magnitude of ocean forcing in all uncoupled experiments agrees well with that of the coupled runs, although the seasonal signal and extremes appear to be dampened. In figure 4.6b, we observe that the mean speed of the ASC fluctuates around -0.15 m/s in all coupled experiments until 2040, after which its speed begins to decrease at an average rate of 0.025 m/s/yr through 2100 in SSP585. By the end of the century in SSP585, the mean strength of the ASC at 118°E reduces to nearly 0 m/s as a strong eastward current develops at the surface.

The sea level contribution of Totten Glacier varies significantly between experiments and in time (figure 4.6c). In all experiments, Totten Glacier either remains in steady state or loses mass, except under $SSP126_u$. In this experiment, Totten Glacier gains approximately 0.5 mm SLRe due to mass gain from inland snowfall exceeding mass loss resulting from coastal grounded ice discharge. In the coupled experiments, ice mass loss at a rate of 10 Gt/yr is sustained between 2017–2070. This rate of mass loss does not deviate after 2070 in CTRL and SSP126, resulting in 1.32 mm SLRe loss by 2100. In SSP585, however, mass loss accelerates from 10 to 35 Gt/yr after 2070, culminating in a total mass loss of 4.41 mm SLRe by 2100. This point of rapid acceleration in mass loss at 2070 is also evident in $SSP585_u$, as the rate of mass loss between 2070 and 2100 mimics that of SSP585. However, prior to 2070, Totten Glacier does not lose mass in the uncoupled experiments.

Retreat of Totten Glacier's grounding line ensues primarily along the southern and eastern

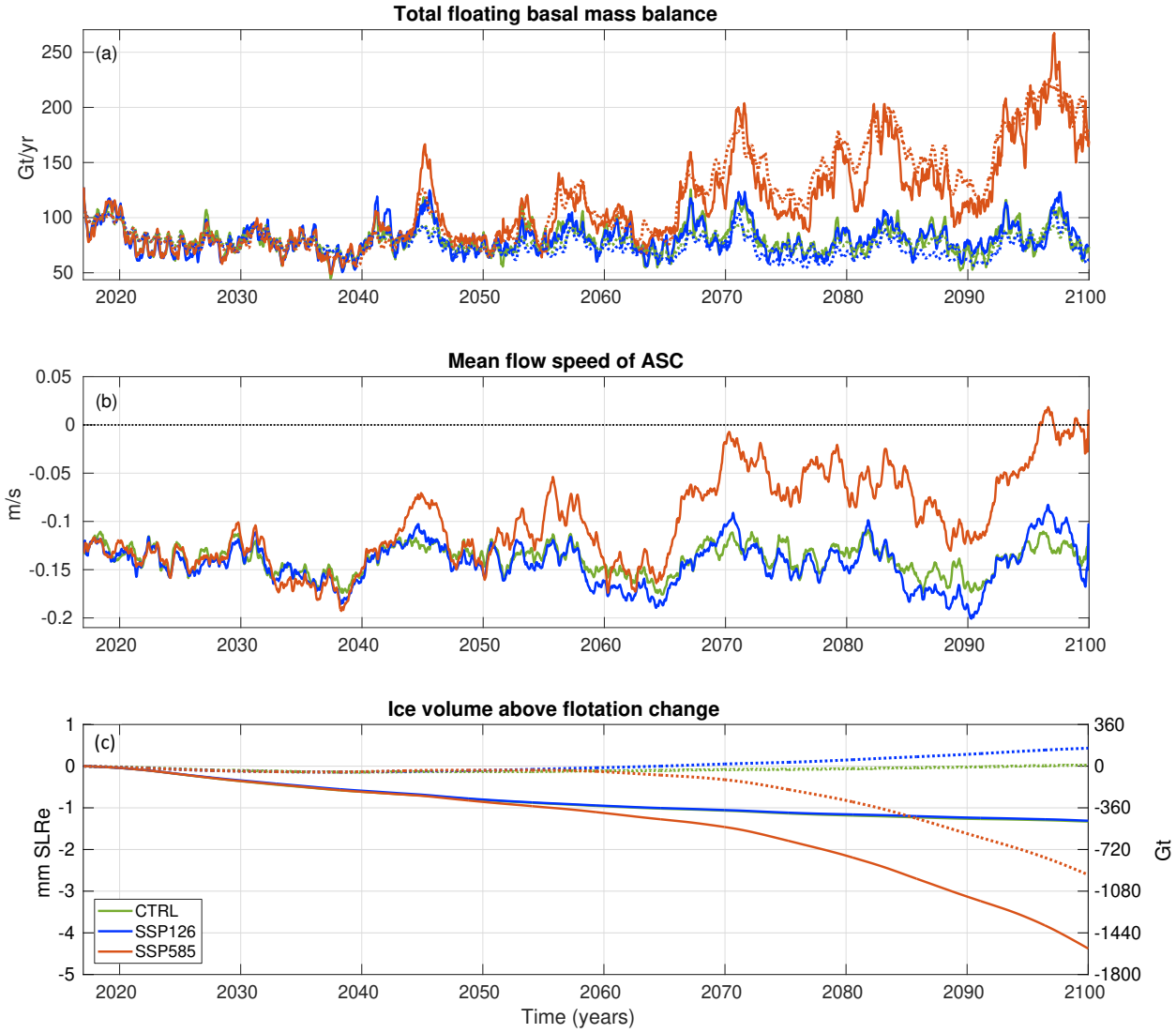

Figure 4.6: Time-series of (a) Totten Glacier total basal mass balance (Gt/yr), (b) yearly averaged strength of the ASC (m/s) computed between 270 and 820 m depth on the continental slope at 118°E (red outline in figure 4.12, negative values indicate westward flow), and (c) change in ice volume above flotation (mm SLRe and Gt, negative values indicate sea level rise). Solid lines and dotted lines correspond to coupled and uncoupled model results, respectively.

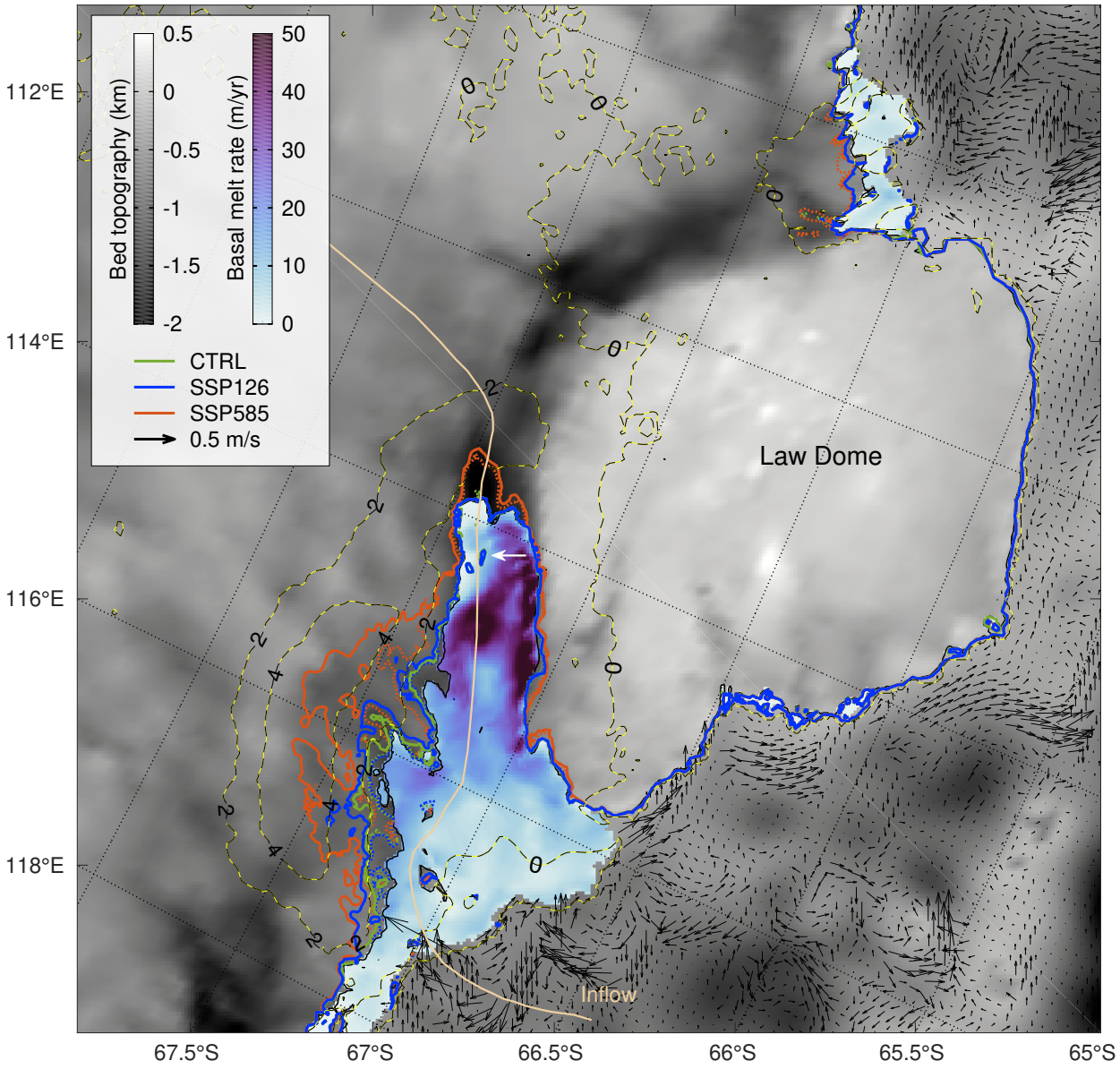

Figure 4.7: Final 2100 grounding line positions overlaid onto bed topography from Morlighem et al. (2020), with the initial grounding line overlaid in black. The SSP585 basal melting rate during the warm water intrusion of January 1, 2070 is displayed over floating ice. The SSP585 rate of change in surface elevation (m/yr) between 2017–2100 is contoured in black and yellow dashed lines (positive values indicate surface lowering). Black arrows over open ocean show the bottom ocean flow direction on January 1, 2070, and the length of the arrows are scaled to the magnitude of the velocity (max 0.5 m/s). The beige flowline labeled "Inflow" is used in figure 4.12 and the white arrow near the southern end of Totten Glacier's ice shelf denotes the location of the rumples. Solid grounding lines and dotted grounding lines correspond to coupled and uncoupled model results, respectively.

grounding zones (figure 4.7). Along Totten Glacier's eastern grounding zone, the grounding line begins retreating immediately in all projections and stabilizes along topographic highs in CTRL, SSP126, and all uncoupled simulations (figure 4.7 and 4.9). In SSP585, however, the eastern grounding zone continues retreating at a rate of ∼0.75 km/yr upstream beyond these stabilizing features through 2100 (figure 4.8). Along this region of rapid retreat, modeled thinning rates exceed 4 m/yr in SSP585, comparable to that of the most dynamic basins in West Antarctica. Along Totten Glacier's southern grounding zone, significant retreat beyond the location of the present day grounding line does not occur until 2070 in coupled and uncoupled high emission projections. Once initiated, retreat progresses rapidly at a rate between 0.65–0.8 km/yr, with thinning rates along this sector averaging 1.5–2.5 m/yr in SSP585 (figure 4.7).

This large-scale retreat of Totten Glacier is primarily driven by strong sub-shelf basal melting. In coupled simulations, basal melting reaches a maximum along Totten Glacier's western ice shelf, where melt rates exceed 80 m/yr in SSP585 (figure 4.7). In CTRL and SSP126, however, melt rates along the southern and western ice shelf are reduced to ∼40 m/yr, as ocean water within the sub-ice shelf cavity is more than 1°C cooler compared to SSP585 (figure 4.12). Along the eastern grounding zone, melting in excess of 30 m/yr results from the inflow of warm water into Totten Glacier's sub-shelf cavity, as mCDW (-0.5°C and 1°C in CTRL/SSP126 and SSP585, respectively) flows along the seafloor of the continental shelf and enters beneath Totten Glacier's ice shelf near the eastern ice front (figures 4.12 and 4.8). This strong melting is not captured in our uncoupled simulations, as melt rates computed by PICOP do not exceed 10 m/yr directly along Totten Glacier's eastern grounding line (figure 4.10). This reduced melting results in underestimated rates of eastern grounding line retreat in the uncoupled simulations.

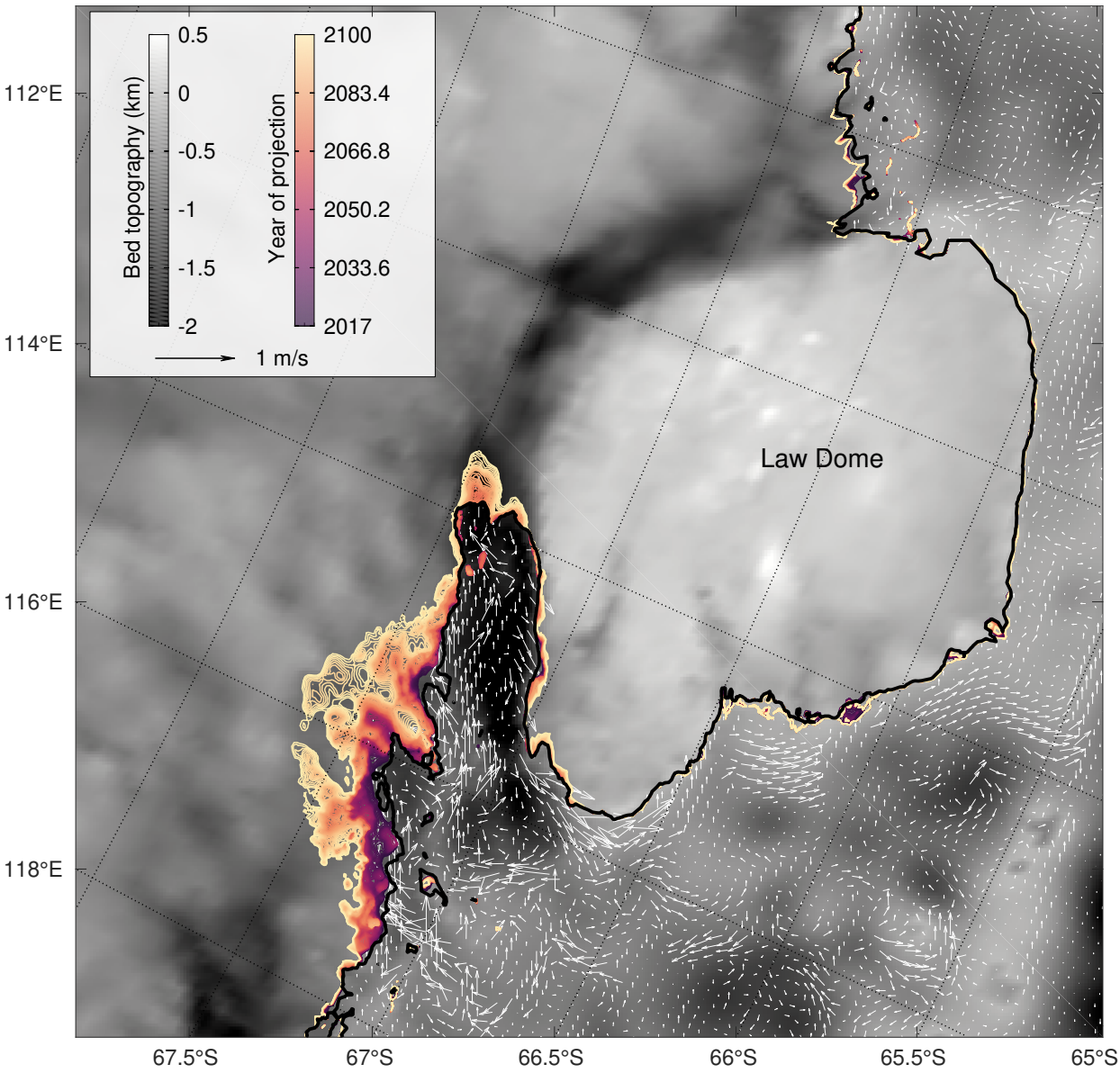

Figure 4.8: SSP585 modeled grounding lines are plotted yearly over bed topography from Morlighem et al. (2020). Over open ocean and floating ice, bottom ocean velocity vectors are plotted as white arrows (with scale beneath the colorbars).

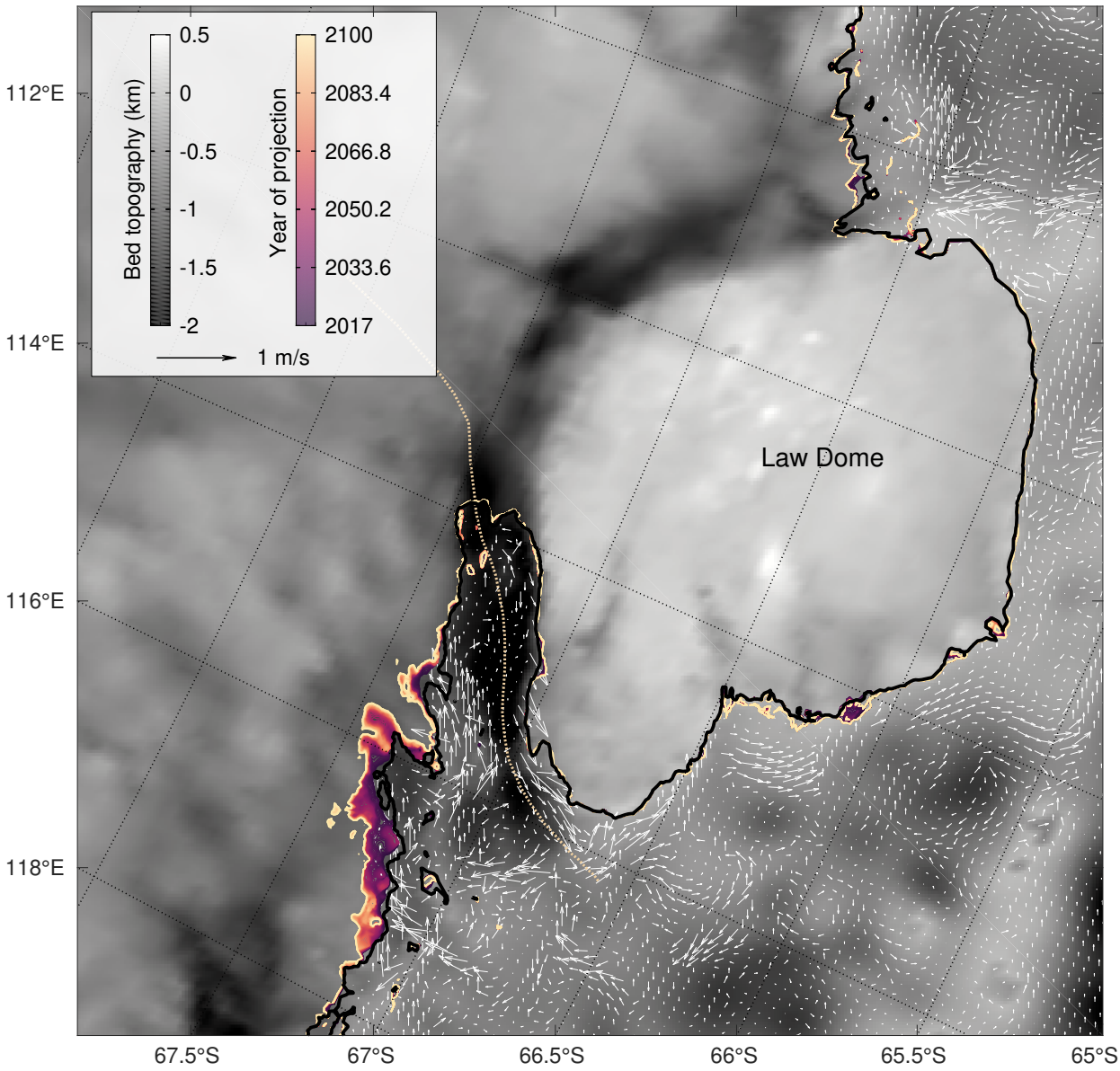

Figure 4.9: Same as figure 4.8, but with grounding lines and bottom ocean velocity vectors taken from experiment SSP126.

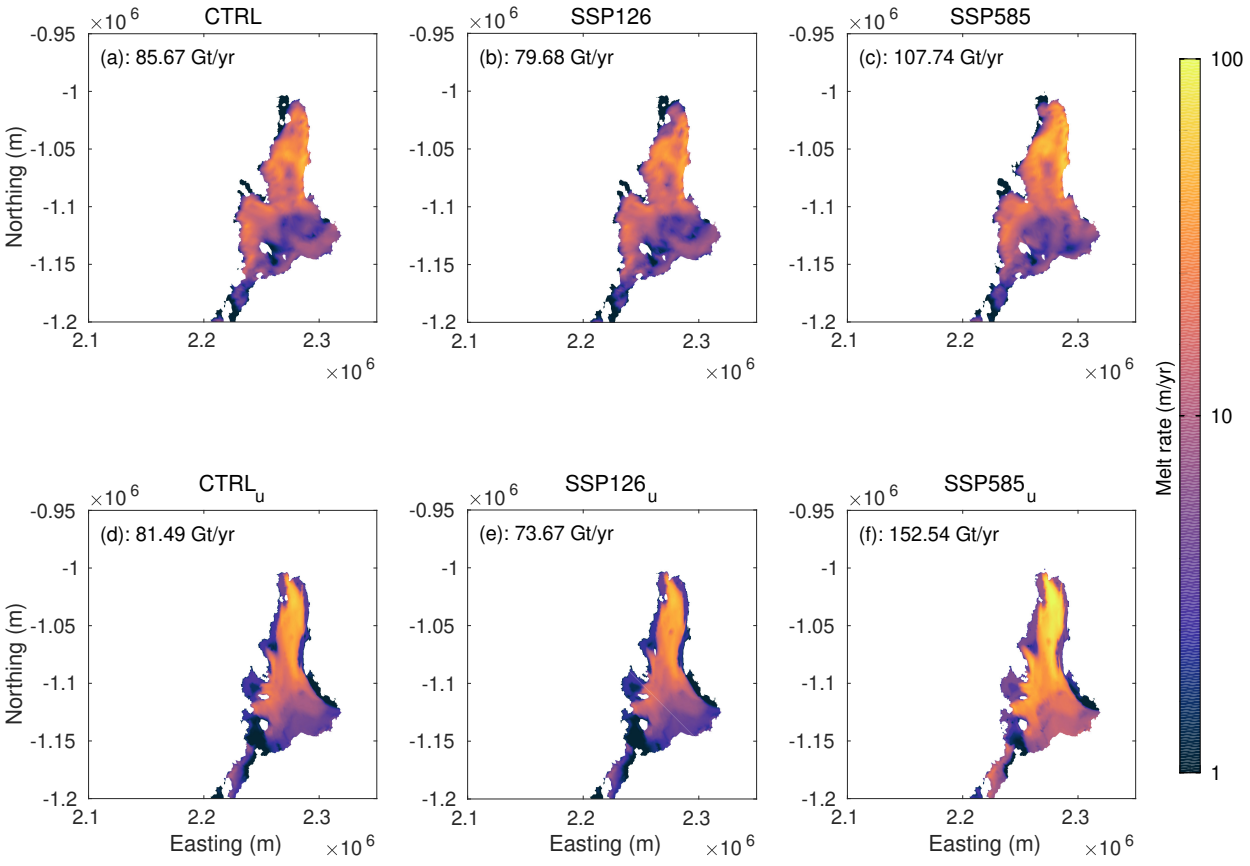

Figure 4.10: The modeled basal melt rate on January 1, 2070 is plotted for the coupled (a,b,c,) and uncoupled (d,e,f) experiments under CTRL (a,d), SSP126 (b,e), and SSP585 (c,f). The total basal mass balance in Gt/yr is displayed in the top left corner of each panel.

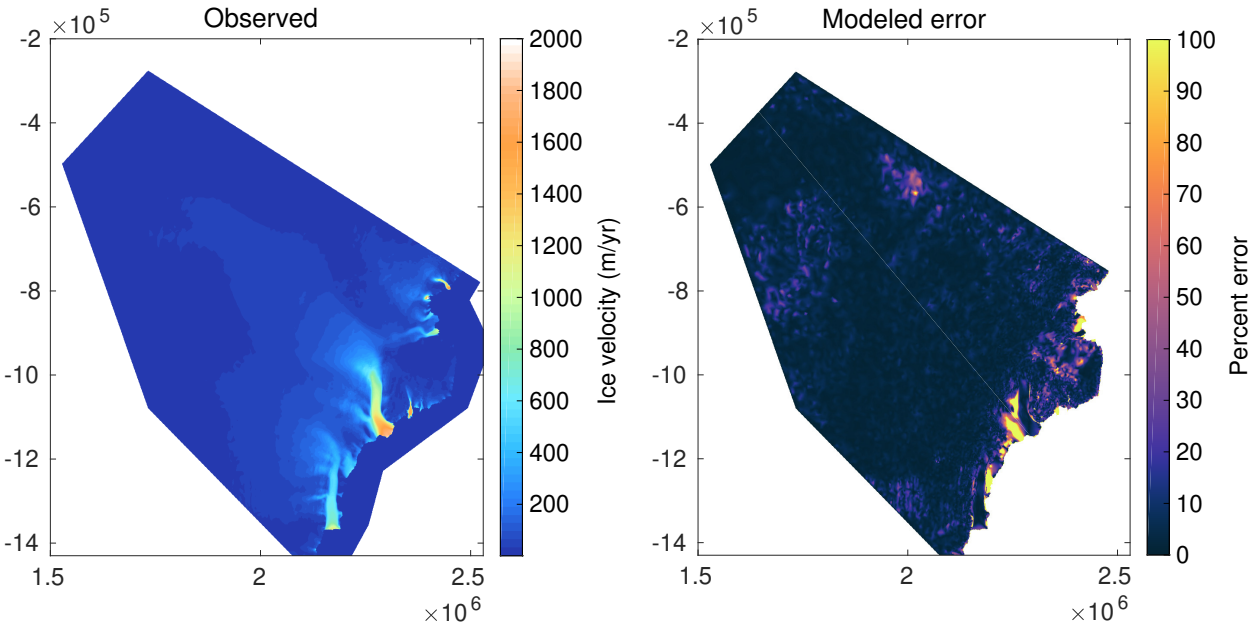

Figure 4.11: Observed (left) and modeled percent error ((modeled-observed)/observed·100%, right) January 1, 2017 surface ice velocities. Observations are taken from Mouginot et al. (2019b).

4.3 Discussion

The simulated ocean forcing and evolution of Totten Glacier in the coupled projections are consistent with contemporary observations. The modeled initial surface ice velocity of Totten Glacier displays excellent agreement with Mouginot et al. (2019b), suggesting that we are properly capturing the glacier's stress-regime (figure 4.11). In CTRL, the modeled velocity displays no long-term trend, agreeing with observations of Totten Glacier that reveal counteracting increases and decreases in surface ice speed between 1990–2017 (Rignot et al., 2019). Simulated rates of mass loss in the coupled experiments between 2017–2050 remain steady at 10 Gt/yr. Rignot et al. (2019) observed that Totten Glacier lost 7.3 Gt/yr between 2003–2017 and that this rate of mass loss is increasing. The simulated melt water flux from Totten Glacier's ice shelf averages 80.56 Gt/yr in CTRL, agreeing with satellite estimates of 64.0 ± 11.0 Gt/yr between 1994-2018 (Adusumilli et al., 2020). For a complete validation of the ocean model, see Nakayama et al. (submitted).

Strong melting evident in the basal mass balance time-series in figure 4.6a reveals that recurrent intrusions of mCDW are reaching Totten Glacier's sub-ice shelf cavity in the coupled simulations. In their standalone ocean simulations, Nakayama et al. (submitted) found that weakening of the ASC always accompanies on-shelf warming, signifying that the strength of the ASC modulates warm water intrusions towards Totten Glacier. The results from our future experiments are consistent; increases in the fresh water flux from Totten Glacier's ice shelf are correlated with decreases in the strength of the ASC in SSP585 with an R-squared value of 0.82 (figure 4.6a and 4.6b). During the warm water intrusion event of 2070, the ASC retains its strength and acts as a barrier to on-shelf oceanic heat transport in CTRL and SSP126. In contrast, under SSP585, weakening of the ASC allows mCDW (1–1.5°C) to spill onto the continental shelf and circulate towards Totten Glacier, where it promotes strong basal melting (figure 4.12 and 4.10). Nakayama et al. (submitted) found that variability in the strength of the ASC is primarily attributed to fluctuations in ASC strength at the eastern model boundary, implying that large-scale atmospheric and oceanic circulations outside the model domain control this current. Additionally, freshening at the eastern model boundary by 0.1 and 0.2 on the Practical Salinity Scale results in a 11% and 36% reduction in ASC strength, respectively (Nakayama et al., submitted). That is, the timing of cross-slope mCDW transport is largely controlled by the ASC as defined at the eastern ocean boundary; however, density reduction of on-shelf ocean properties promotes more frequent and intensified mCDW intrusion events. This finding is consistent with Gwyther et al. (2014) and Khazendar et al. (2013), who found that reductions in the formation of dense shelf water produced by the Dalton polynya allow for on-shelf transport of mCDW towards Totten Glacier's ice shelf. Our findings remain consistent, as a freshening of 0.50 on the Practical Salinity Scale at the eastern ocean model boundary results in a 83% weakening in the strength of the ASC and a 56% increase in melt of Totten Glacier's ice shelf in SSP585 relative to CTRL (figure 4.6).

This ocean forcing drives rapid retreat of Totten Glacier's eastern grounding zone in all

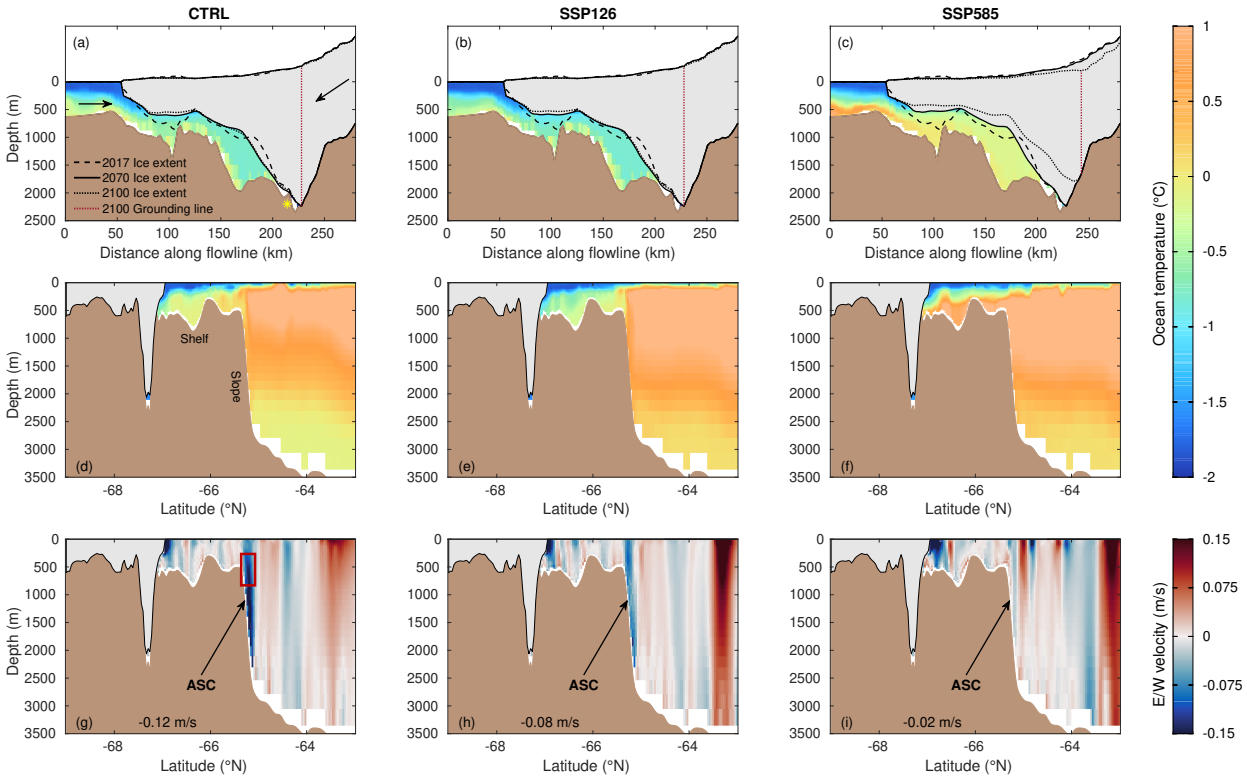

Figure 4.12: Cross-sections of ocean temperature (a–f) and east/west velocity (positive is eastward flow, g–i) on January 1, 2070. Ice is shaded in gray and bed topography is shaded in tan. In panels a–c, cross-sections are taken along the beige flowline in figure 4.7. The 2017, 2070, and 2100 ice shelf geometries are plotted as the dashed, solid, and dotted black lines, respectively. The final 2100 grounding line position is plotted as the red dotted line. In panel-a, the yellow star denotes the location of the "rumples" and arrows show the estimated directions of ice and ocean flow. In panels d–i, cross-sections are taken along 118°E. In panels g–i, the average strength of the ASC on January 1, 2070 is given and the red outline in panel g denote the area in which the strength of the ASC was averaged (figure 4.6b).

coupled experiments, accounting for the sustained mass loss of 10 Gt/yr between 2017–2070 (figures 4.6c, 4.8, and 4.9). Retreat along the southern grounding zone, however, only occurs in high emission scenarios and is synchronous with rapid acceleration in mass loss after 2070. Near Totten Glacier's southern grounding zone, topographic highs referred to as "rumples" remain grounded in CTRL and SSP126 through 2100, acting as a barrier that prevents warm water from reaching the southern grounding zone (figures 4.7 and 4.9). In SSP585, these rumples unground during the strong warm water intrusion event of 2045 (figures 4.6a and 4.8). This both reduces backstress applied to the upstream grounded ice and opens a new pathway for mCDW to reach the southern grounding zone and induce strong melting. In figure 4.12, we observe that warm water is present upstream of the rumples (yellow star in figure 4.12a) in SSP585 but not in CTRL and SSP126. In the latter experiments, water is diverted west towards the region of outflow and does not induce melting directly at the grounding line (figure 4.9). These rumples have been cited as a pinning point of Totten Glacier in both observational and modeling studies (Li et al., 2015; Pelle et al., 2020; Roberts et al., 2018); however, the findings presented here suggest that these topographic highs serve the dual-purpose of acting as both a pinning point and barrier to warm water inflow.

In $SSP585_u$, retreat of Totten Glacier's southern grounding zone agrees well with the corresponding coupled simulation because PICOP computes strong melting in this region. The location of the parameterized plume of strong melting along Totten Glacier's western ice shelf is similar to the spatial distribution of melt rates produced by the coupled models, resulting in rates of retreat of the southern grounding zone that agrees with that of SSP585. In contrast, retreat along the eastern grounding zone is underestimated in our uncoupled simulations because PICOP cannot capture the inflow of warm ocean water along the grounding line through this region (figures 4.12 and 4.10). The box model used in PICOP disperses ocean-heat across Totten Glacier's entire grounding line, rather than concentrating it along the zone of warm water inflow. This, combined with the shallow grounding line depths that are used in the computation of melting rates in PICOP, results in limited eastern retreat and

mass loss prior to 2070 (figure 4.6c and 4.7). In the coupled experiments, warm ocean water flows south directly along the eastern grounding line, resulting in melting rates exceeding 30 m/yr. Due to the gently sloping bed in this region, minimal forcing is needed to dislodge the eastern grounding line, resulting in sustained retreat and mass loss through 2100.

The difference in retreat between our coupled and uncoupled simulations contrasts with previous modeling studies, which find that uncoupled models tend to overestimate grounding line retreat because parameterized melting is too strong in confined sub-shelf cavities (Seroussi et al., 2017; De Rydt and Gudmundsson, 2016). Such studies simulated ocean forcing with the use of a depth-dependent melting rate parameterization, which disperses oceanic-heat directly along the grounding line. This type of melt parameterization was used by Sun et al. (2016), who simulated the Aurora Basin through the 22$^{\text{nd}}$ century and found that widespread grounding line retreat occurred principally through Totten Glacier's eastern flank, agreeing with our coupled model simulations. In contrast, PICOP computes a plume of high melt rates along the central ice shelf that follows the advection of deep grounding line heights and steep basal slopes, resulting in delayed retreat away from this plume (figure 4.10). Contrasting with uncoupled studies, our coupled ice-ocean model represents the details of the spatial distribution of melting that are important for dynamic retreat. Yet, the excellent agreement in the magnitude of basal melting between PICOP and the fully coupled ice-ocean model highlights that PICOP is still a valuable tool to simulate ice-ocean processes in continental-scale ice sheet projections.

In terms of model limitations, we used the SSA stress balance approximation; however, a three-dimensional approximation (Pattyn, 2003) that captures longitudinal and transverse stress gradients would possibly better resolve small-scale grounding line features. Additionally, basal friction in our ice sheet model was computed assuming a Budd friction law (Budd et al., 1979) and the friction coefficient is held constant over time (as is the ice stiffness parameter). Basal friction remains an active area of research and our results are dependent

on this choice of sliding law (Brondex et al., 2017, 2019; Joughin et al., 2019). We also assume a fixed ice front, whereas ice velocity accelerations have been corroborated with calving events over other East Antarctic glaciers (Rignot et al., 2019). Lastly, we do not include the impacts of subglacial hydrology in our coupled system; yet, Dow et al. (2020) found that several channels transporting substantial volumes of subglacial water cross Totten Glacier's southern grounding line. The presence of the channels near Totten Glacier's grounding line could influence grounding line migration patterns and sub-ice shelf basal melting rates, as the fresh water discharge into the sub-ice shelf cavity would increase the buoyancy of the ocean water. In our ocean model, 4–5 km horizontal resolution is too coarse to resolve eddies, which are a primary control of flow across the continental shelf, along the shelf break, and in the vicinity of grounding zones. Lastly, there is limited knowledge of bathymetry on the continental shelf and beneath Totten Glacier's ice shelf. However, our ocean model can reproduce the modeled interannual variability in mCDW near Totten Glacier's ice shelf (Gwyther et al., 2014) and the location of mCDW inflow to Totten Glacier's sub-shelf cavity is consistent with observations from Rintoul et al. (2016).

Overall, the coupled simulations presented here paint a coherent picture of the sensitivity of Totten Glacier to future changes in ocean forcing. By pinpointing the location and magnitude of retreat of vulnerable sectors of Totten Glacier, as well as potential pathways of warm water that will drive this retreat, we can help steer observational focus and guide resource distribution in future scientific missions.

4.4 Summary

In this study, we investigate the dynamic response of Totten Glacier to 21st century ocean forcing in a coupled ice-ocean model. Anomalies in potential temperature, salinity, and velocity from CMIP6 emission scenarios are used to force an ocean model (Nakayama et al.,

submitted) coupled with an ice sheet model of Totten Glacier over the 21st century. Consistent with Nakayama et al. (submitted), future intrusions of mCDW towards Totten Glacier's ice shelf are modulated by the strength of the ASC, which is primarily controlled by velocity and salinity fluctuations at the eastern boundary. Widespread grounding line retreat is observed along Totten Glacier's eastern grounding zone in all coupled simulations, driven by the inflow of warm ocean water against the eastern grounding line. This retreat accounts for the sustained mass loss of 10 Gt/yr through 2070. In contrast, modeled retreat of Totten Glacier's southern grounding zone occurs exclusively in high emission scenarios, as warm ocean water can only access the southern grounding line after topographic highs unground. After 2070, Totten Glacier's rate of mass loss increases 3.5-fold (from 10 to 35 Gt/yr), resulting in a total sea level contribution of 4.40 mm SLRe by 2100 in SSP585. Uncoupled simulations forced with the PICOP melt parameterization resolve the timing and spatial pattern of retreat of Totten Glacier's southern grounding zone. Retreat of the eastern grounding zone, however, cannot be captured in the uncoupled models because a simplified melt parameterization cannot resolve the spatial distribution and horizontal circulation of warm, sub-shelf ocean water.

Overall, the asymmetric and asynchronous patterns of grounding line retreat projected in this study result from complex interplay between Totten Glacier and the Southern Ocean. As downstream freshening was found to promote enhanced thermal forcing from the Southern Ocean, the looming threat of rapid freshening from collapse of the West Antarctic Ice Sheet could set off a chain reaction that results in rapid melting of Antarctica's most vulnerable ice shelves. Therefore, systemic monitoring of both oceanic conditions at the shelf break (e.g. deploying moorings for state-of-change monitoring) and ice dynamics in the vicinity of such vulnerable glaciers should be prioritized by the scientific community for the future welfare of coastal communities.

Chapter 5

Conclusions

5.1 Summary of major results

Totten Glacier, located in the East Antarctic Ice Sheet, contains a sea level potential comparable to that of the entire West Antarctic Ice Sheet. Over the past two decades, Totten Glacier has displayed dynamic behavior that is primarily attributed to fluctuations in thermal forcing from the Southern Ocean. Yet, efforts to model this glacier in transient ice flow models have been limited due in part to their incomplete representation of ocean forcing. In this dissertation, we improved the representation of ice-ocean processes in transient ice flow models through the development of a new ice shelf basal meting rate parameterization. We then estimated the future sea level rise contribution and dynamic evolution of Totten Glacier and dynamic basins of the East Antarctic Ice Sheet using a hierarchy of ice-ocean coupled numerical models. Below, we summarize the results and conclusions of the three main chapters of this dissertation:

In chapter 2, we derived a novel basal melting rate parameterization (PICOP) by combining the sub-ice shelf ocean box model, PICO, to a buoyant plume melt rate parameterization.

By combining these two existing parameterizations, we are able to reduce inputs into the parameterization to basin-averaged values while maintaining the proper ice shelf geometry dependence. We tested PICOP on the Amundsen Sea sector of West Antarctica, Totten, and Moscow University ice shelves in East Antarctica and the Filchner-Ronne Ice Shelf and compare the results to PICO. We find that PICOP is able to reproduce the inferred high melt rates beneath Pine Island, Thwaites, and Totten Glaciers (on the order of 100 m/yr) and removes the "banding" pattern observed in melt rates produced by PICO over the Filchner-Ronne Ice Shelf. In all, the spatial distribution and magnitude of melt rates produced by PICOP are in excellent agreement with observations from both warm and cold water ice shelves. As such, PICOP is a valuable tool for those looking to make large- (century- and continental-) scale ice sheet model projections.

In chapter 3, we modeled the evolution of six dynamic EAIS catchments to 2100 using three basal melt rate parameterizations (including PICOP) and force our model with surface mass balance and ocean thermal anomalies from ten CMIP5 and CMIP6 global climate models. While the domain loses mass under low-emission scenarios, it gains $\sim$10 mm SLRe under high-emission scenarios as inland snowfall offsets coastal grounded ice discharge. The primary region of thinning is within 50 km upstream of Totten Glacier's southern grounding zone. Glacial discharge from Totten Glacier is modulated by the migration of its grounding line, which is sensitive to brief intrusions of ocean water at temperatures higher than present. Once the southern-most portion of Totten Glacier's grounding line is dislodged, ice velocity increases by up to 70% of its present-day configuration, resulting in $\sim$6 mm SLRe loss from this sector.

In chapter 4, we projected Totten Glacier's evolution through 2100 in a fully coupled ice-ocean model, forced at the ocean boundaries with anomalies in CMIP6 projected temperature, salinity, and velocity. Consistent with previous studies, the Antarctic Slope Current continues to modulate warm water inflow towards Totten Glacier in future simulations.

Warm water (-0.5–1°C) accesses Totten Glacier's sub-ice shelf cavity through depressions along the eastern ice front, driving sustained retreat of the eastern grounding zone that cannot be captured in uncoupled models. In high emission scenarios, warm water overcomes topographic barriers and dislodges the southern grounding zone around 2070, increasing the rate of grounded ice loss 3.5-fold (10 to 35 Gt/yr) and resulting in a total 4.40 mm SLRe loss by 2100.

From these projections, a coherent picture of Totten Glacier's possible future evolution over the 21st century emerges. Warm modified circumpolar deep water (-1 – 0°C) has already been observed on the continental shelf just downstream of Totten Glacier's ice shelf, promoting strong sub-ice shelf basal melting that has been inferred from satellite observations. Ocean freshening to the east has the potential to drive enhanced intrusion of mCDW to Totten Glacier's ice shelf through the weakening of the Antarctic Slope Current, which acts as a barrier to the transport of mCDW onto the continental shelf. Warm water accesses Totten Glacier's ice shelf through two topographic depressions located along the central and eastern ice front, circulating cyclonically and driving ongoing retreat along the eastern grounding zone. Basal melting reaches a maximum along Totten Glacier's western ice shelf (due to vertical overturning and faster ocean velocities along the sub-shelf western boundary current), which is protected by increases in bed topography called "rumples". If the cyclonic sub-shelf ocean circulation becomes strong enough to overcome these topographic barriers, strong melting along the southern grounding line will drive retreat across a 7 km long by 8 km wide ice plain. This ice plain supplies buttress to upstream grounded ice and if ungrounded, ice velocity and grounded ice discharge will increase and drive grounded ice thinning rates that are comparable to the most dynamic WAIS glaciers. Grounding line retreat beyond the ice plain is dependent on the applied ocean forcing, meaning that Totten Glacier's southern grounding zone is not conducive to marine ice sheet instability in its current configuration. By 2100, Totten Glacier is expected to contribute anywhere from 2 to 7 mm to global sea level rise, with the majority of grounded ice loss occurring after 2070.

On the distinction between representing ice-ocean interactions with parameterizations verses model coupling, the choice boils down to the availability of oceanographic data and the purpose of the study. While the work presented in chapters 3 and 4 confirms that model coupling is the most accurate manner to represent ice-ocean process in ice sheet models, it is not feasible to implement in large-scale projections due to the high computational cost. In addition, ice-ocean modeling of Antarctic glaciers is still in its infancy due to limited ocean state and bathymetry observations, especially along the East Antarctic coast. The decreased reliability of ocean models in sparely monitored regions defeats the purpose of coupling, as the simulated ocean state and circulation cannot be validated. In such instances, it is best to use a parameterization of basal melting in which inputs are reduced to either basin averaged ocean state values (e.g. PICO, PICOP, and the non-local quadratic parameterization) or inferred melt rates (e.g. depth dependent parameterization). However, as shown in chapter 4, simplified parameterizations cannot resolve small-scale ocean circulation features that drive complex patterns of grounding line retreat. As such, if one seeks to understand how ocean forcing drives dynamic change of a glacial system (or vice versa), it is only appropriate to do so in a coupled model framework.

5.2 Future perspectives

While the work presented in this dissertation provides major advances in our understanding of both ice-ocean processes and the future evolution of Totten Glacier, there remain many scientific barriers and outstanding questions that need to be addressed. To begin, the only feasible way to simulate ice-ocean interactions in large-scale ice sheet projections is through the implementation of a basal melting rate parameterization, as ice-ocean model coupling at such scales is too computationally expensive. Yet, the simplifications made to derive such efficient parameterizations often comes at the cost of omitting more complex ocean

circulation physics, such as horizontal ocean circulation, the spatial distribution of vertical over turning, etc. As such, large scale ice sheet projections that utilize such parameterizations often suffer from high degrees of uncertainty that stem from these simplifications (e.g. ISMIP6, Seroussi et al., 2020). In order to improve these continental-scale mass balance projections, we need to begin developing melt rate parameterizations that can resolve more complex ocean circulation.

Jenkins and Nost (2017) began investigating this problem through the development of a diagnostic model of the depth-dependent horizontal ocean circulation that results from an imposed ice-shelf cavity geometry and density distribution. The equations of motion and heat transfer have been simplified by assuming a steady state ocean stratification, resulting in a computationally efficient model. The resulting patterns of along and across-slope heat transport agree well with more complex ocean circulation models, suggesting that this reduced-physics model can be tuned to approximate ocean circulation model solutions at a fraction of the computational cost. The physics used to derive this simplified model of horizontal ocean circulation can be used as a starting point to address the contemporary limitations of existing basal melting rate parameterizations. If implemented in standalone ice sheet models, this improvement would bridge a critical gap, which has existed in the ice-ocean modeling community for 25 years, between overly simplified basal melting rate parameterizations and expensive fully coupled ocean circulation models.

In addition, the observational record of Totten Glacier and surrounding regions is far from complete due to the glacier's remoteness and harsh surface conditions that prohibit systematic monitoring. Observations, such as ice thickness, velocity, and grounding line measurements, are used to initialize our ice sheet model and validate the output of our projections. For example, Totten Glacier's grounding line has only been completely mapped in 1996, and the southern grounding zone remapped in 2013 (Rignot and Jacobs, 2002; Li et al., 2015). The eastern grounding zone, downstream of which Greenbaum et al. (2015) observed a sub-

glacial trough that offers an access point of mCDW to eastern side of Totten Glacier's sub-ice shelf cavity, has not been remapped since 1996. As our coupled models have shown that Totten Glacier's eastern grounding zone is vulnerable to retreat under present day forcing, it is vital that future scientific missions prioritize monitoring this dynamic glacier. It is equally important to observe the near-shelf ocean bathymetry and state that supply the forcing driving Totten Glacier's observed changes (i.e. Rintoul et al., 2016), as these observations can serve to validate the ocean component of ice-ocean coupled models.

Aside from oceanic forcing driving change of Totten Glacier, recent evidence points to the possibility of subglacial discharge impacting the stability of Totten Glacier's ice shelf. Using the GlaDS subglacial hydrology model, Dow et al. (2020) inferred the presence of several large subglacial water channels draining across the southern end of Totten Glacier's grounding line. The location of these channels corresponds to both the location of Totten Glacier's ice stream as well as peak melt rates observed in Adusumilli et al. (2020). Fresh subglacial discharge can enhance basal melting by further decreasing the density of water along the ice shelf-ocean interface, promoting acceleration of the density-driven overturning circulation. As this process influences sub-shelf ocean circulation (thereby impacting ice shelf stability), it should be included in transient model simulations. One could accomplish this through three way ice-ocean-hydrological model coupling, or by using output from a subglacial hydrology model as input into the ocean model (making the assumption that the subglacial discharge remains constant over the model simulation period). Regardless of the approach, resolving the subglacial hydrological system that underlays Totten Glacier in transient ice sheet models could further improve the accuracy of transient model simulations.

Mass balance estimates of Totten Glacier and surrounding regions are largely dependent on the surface mass balance contribution, which displayed significant uncertainty in ISMIP6 (Seroussi et al., 2020). Over East Antarctica under high emission scenarios, the surface mass balance contribution varied between 2.5 and 28.5 mm SLRe, whereas the glacial discharge

contribution varied between 2 and 14 mm SLRe (Pelle et al., 2020; Seroussi et al., 2020). Although diagnosing and reducing uncertainty in AOGMC surface mass balance output is beyond the scope of this dissertation, the reliability of Antarctic mass balance projections will suffer until we can constrain this important model input.

Furthermore, aside from Totten Glacier, there exist other dynamic glaciers along the East Antarctic coast that need to be closely monitored by in situ and remote observations, as well as studied via numerical modeling. One such "sleeping giant" is Denman Glacier, which contains 1.5 m SLRe and has retreated 5.4 ± 0.3 km in 22 years towards the deepest marine basin in Antarctica (Brancato et al., 2020; Rignot et al., 2019; Morlighem et al., 2020). Adusumilli et al. (2020) inferred the highest melt rates across Antarctica (>100 m/yr) right along the grounding line that rests at the crux of this deeply entrenched valley, forced in part by warm ocean waters observed on the continental shelf close to Denman Glacier's floating ice tongue (Roquet et al., 2018). As Totten Glacier was not susceptible to marine ice sheet instability, further migration of Denman Glacier's grounding line might result in irreversible retreat that would have drastic implications on its future sea level rise contribution.

Bibliography

Adusumilli, S., Fricker, H. A., Medley, B., Padman, L., and Siegfried, M. R. (2020). Interannual variations in meltwater input to the Southern Ocean from Antarctic ice shelves. *Nat. Geosci.*, 13(9):616–620.

Aitken, A. R. A., Roberts, J. L., Ommen, T. D. v., Young, D. A., Golledge, N. R., Greenbaum, J. S., Blankenship, D. D., and Siegert, M. J. (2016). Repeated large-scale retreat and advance of Totten Glacier indicated by inland bed erosion. *Nature*, 533(7603):385–389.

Antonov, J. I., Seidov, T. P., Boyer, R. A., Locarnini, A. V., Mishonov, H. E., Garcia, O. K., Baranova, M. M., Zweng, M. M., and Johnson, D. R. (2010). *World Ocean Atlas, Volume 2: Salinity*. NOAA Atlas NESDIS 69. U.S. Government Printing Office, Washington, D.C.

Asay-Davis, X. S., Cornford, S. L., Durand, G., Galton-Fenzi, B. K., Gladstone, R. M., Gudmundsson, G. H., Hattermann, T., Holland, D. M., Holland, D., Holland, P. R., Martin, D. F., Mathiot, P., Pattyn, F., and Seroussi, H. (2016). Experimental design for three interrelated Marine Ice-Sheet and Ocean Model Intercomparison Projects. *Geosci. Model Dev.*, 9:2471–2497.

Barthel, A., Agosta, C., Little, C. M., Hatterman, T., Jourdain, N. C., Goelzer, H., Nowicki, S., Seroussi, H., Straneo, F., and Bracegirdle, T. J. (2019). CMIP5 model selection for ISMIP6 ice sheet model forcing: Greenland and Antarctica. *The Cryosphere Discussions*, 2019(191):1–34.

Beckmann, A. and Goosse, H. (2003). A parameterization of ice shelf–ocean interaction for climate models. *Ocean Modelling*, 5:157–170.

Blatter, H. (1995). Velocity And Stress-Fields In Grounded Glaciers: A Simple Algorithm For Including Deviatoric Stress Gradients. *J. Glaciol.*, 41(138):333–344.

Brancato, V., Rignot, E., Milillo, P., Morlighem, M., Mouginot, J., An, L., Scheuchl, B., Jeong, S., Rizzoli, P., Bueso Bello, J. L., and Prats-Iraola, P. (2020). Grounding line retreat of Denman Glacier, East Antarctica, measured with COSMO-SkyMed radar interferometry data. *Geophys. Res. Lett.*, 47(7):e2019GL086291.

Brondex, J., Gagliardini, O., Gillet-Chaulet, F., and Durand, G. (2017). Sensitivity of grounding line dynamics to the choice of the friction law. *J. Glaciol.*, 63(241):854–866.

Brondex, J., Gillet-Chaulet, F., and Gagliardini, O. (2019). Sensitivity of centennial mass loss projections of the Amundsen basin to the friction law. *Cryosphere*, 13(1):177–195.

Budd, W. F., Keage, P. L., and Blundy, N. A. (1979). Empirical studies of ice sliding. *J. Glaciol.*, 23(89):157–170.

Cook, C. P., van de Flierdt, T., Williams, T., Hemming, S. R., Iwai, M., Kobayashi, M., Jimenez, Escutia, C., Gonzalez, J. J., Khim, B., McKay, R. M., Passchier, S., Bohaty, S. M., Riesselman, C. R., Tauxe, L., Sugisaki, S., Galindo, A. L., Patterson, M. O., Sangiorgi, F., Pierce, E. L., Brinkhuis, H., Klaus, A., Fehr, A., Bendle, J. A. P., Bijl, P. K., Carr, S. A., Dunbar, R. B., Flores, J. A., Hayden, T. G., Katsuki, K., Kong, G. S., Nakai, M., Olney, M. P., Pekar, S. F., Pross, J., Rohl, U., Sakai, T., Shrivastava, P. K., Stickley, C. E., Tuo, S., Welsh, K., and Yamane, M. (2013). Dynamic behaviour of the East Antarctic ice sheet during Pliocene warmth. *Nat. Geosci.*, 6(9):765–769.

Cuffey, K. M. and Paterson, W. S. B. (2010). *The Physics of Glaciers, 4th Edition*. Elsevier, Oxford.

De Angelis, H. and Skvarca, P. (2003). Glacier surge after ice shelf collapse. *Science*, 299(5612):1560–1562.

De Rydt, J. and Gudmundsson, G. (2016). Coupled ice shelf-ocean modeling and complex grounding line retreat from a seabed ridge. *J. Geophys. Res.*, 121(5):865–880.

DeConto, R. M. and Pollard, D. (2016). Contribution of Antarctica to past and future sea-level rise. *Nature*, 531:591–597.

Dee, D. P., Uppala, S. M., Simmons, A. J., Berrisford, P., Poli, P., Kobayashi, S., and Vitart, F. (2011). The ERA-Interim reanalysis: configuration and performance of the data assimilation system. *Quarterly Journal of the Royal Meteorological Society*, 137(656):553–597.

Dinniman, M., Asay-Davis, X., Galton-Fenzi, B., Holland, P., Jenkins, A., and Timmermann, R. (2016). Modeling ice shelf/ocean interaction in antarctica: A review. *Oceanography*, 29:144–153.

Dinniman, M. S., Klinck, J. M., and Hofmann, E. E. (2012). Sensitivity of circumpolar deep water transport and ice shelf basal melt along the west Antarctic Peninsula to changes in the winds. *J. Oceanogr.*, 25:4799–4816.

dos Santos, T. D., Morlighem, M., Seroussi, H., Devloo, P. R. B., and Simões, J. C. (2019). Implementation and performance of adaptive mesh refinement in the Ice Sheet System Model (ISSM v4.14). *Geosci. Model Dev.*, 12(1):215–232.

Dow, C., McCormack, F., Young, D., Greenbaum, J., Roberts, J., and Blankenship, D. (2020). Totten Glacier subglacial hydrology determined from geophysics and modeling. *Earth and Planetary Science Letters*, 531:115961.

Dupont, T. K. and Alley, R. B. (2005). Assessment of the importance of ice-shelf buttressing to ice-sheet flow. *Geophys. Res. Lett.*, 32(4):1–4.

Dupont, T. K. and Alley, R. B. (2006). Role of small ice shelves in sea-level rise. *Geophys. Res. Lett.*, 33(9):1–4.

Dutrieux, P., Vaughan, D. G., Corr, H. F. J., Jenkins, A., Holland, P. R., Joughin, I., and Fleming, A. H. (2013). Pine Island glacier ice shelf melt distributed at kilometre scales. *Cryosphere*, 7(5):1543–1555.

Eyring, V., Bony, S., Meehl, G. A., Senior, C. A., Stevens, B., Stouffer, R. J., and Taylor, K. E. (2016). Overview of the Coupled Model Intercomparison Project Phase 6 (CMIP6) experimental design and organization. *Geoscientific Model Development*, 9(5):1937–1958.

Flament, T. and Remy, F. (2012). Dynamic thinning of Antarctic Glaciers from along-track repeat radar altimetry. *J. Glaciol.*, 58(211):830–840.

Fretwell, P., Pritchard, H. D., Vaughan, D. G., Bamber, J. L., Barrand, N. E., Bell, R., Bianchi, C., Bingham, R. G., Blankenship, D. D., Casassa, G., Catania, G., Callens, D., Conway, H., Cook, A. J., Corr, H. F. J., Damaske, D., Damm, V., Ferraccioli, F., Forsberg, R., Fujita, S., Gim, Y., Gogineni, P., Griggs, J. A., Hindmarsh, R. C. A., Holmlund, P., Holt, J. W., Jacobel, R. W., Jenkins, A., Jokat, W., Jordan, T., King, E. C., Kohler, J., Krabill, W., Riger-Kusk, M., Langley, K. A., Leitchenkov, G., Leuschen, C., Luyendyk, B. P., Matsuoka, K., Mouginot, J., Nitsche, F. O., Nogi, Y., Nost, O. A., Popov, S. V., Rignot, E., Rippin, D. M., Rivera, A., Roberts, J., Ross, N., Siegert, M. J., Smith, A. M., Steinhage, D., Studinger, M., Sun, B., Tinto, B. K., Welch, B. C., Wilson, D., Young, D. A., Xiangbin, C., and Zirizzotti, A. (2013). Bedmap2: improved ice bed, surface and thickness datasets for Antarctica. *Cryosphere*, 7(1):375–393.

Glen, J. (1958). The flow law of ice: A discussion of the assumptions made in glacier theory, their experimental foundations and consequences. *IASH Publ*, 47:171–183.

Good, S. A., Martin, M. J., and Rayner, N. A. (2013). EN4: Quality controlled ocean temperature and salinity profiles and monthly objective analyses with uncertainty estimates. *Journal of Geophysical Research: Oceans*, 118(12):6704–6716.

Greenbaum, J. S., Blankenship, D. D., Young, D. A., Richter, T. G., Roberts, J. L., Aitken, A. R. A., Legresy, B., Schroeder, D. M., Warner, R. C., van Ommen, T. D., and Siegert, M. J. (2015). Ocean access to a cavity beneath Totten Glacier in East Antarctica. *Nat. Geosci.*, 8:294–298.

Greene, C. A., Young, D. A., Gwyther, D. E., Galton-Fenzi, B. K., and Blankenship, D. D. (2018). Seasonal dynamics of totten ice shelf controlled by sea ice buttressing. *The Cryosphere*, 12(9):2869–2882.

Gudmundsson, G. H. (2013). Ice-shelf buttressing and the stability of marine ice sheets. *Cryosphere*, 7(2):647–655.

Gwyther, D. E., Galton-Fenzi, B. K., Hunter, J. R., and Roberts, J. L. (2014). Simulated melt rates for the totten and dalton ice shelves. *Ocean Science*, 10(3):267–279.

Gwyther, D. E., O'Kane, T. J., Galton-Fenzi, B. K., Monselesan, D. P., and Greenbaum, J. S. (2018). Intrinsic processes drive variability in basal melting of the Totten Glacier Ice Shelf. *Nat. Commun.*, 9(3141).

Hellmer, H. and Olber, D. (1989). A two-dimensional model for the thermohaline circulation under an ice shelf. *Antarct. Sci.*, 1(4):325–336.

Holland, D. M. and Jenkins, A. (1999). Modeling Thermodynamic Ice–Ocean Interactions at the Base of an Ice Shelf. *J. Phys. Oceanogr.*, 29(8):1787–1800.

Hutter, K. (1982). Dynamics of glaciers and large ice masses. *Ann. Rev. Fluid Mech.*, 14:87–130.

IPCC (2019). *IPCC Special Report on the Ocean and Cryosphere in a Changing Climate*. Geneva: IPCC.

Jacobs, S. S. and Giulivi, C. F. (2010). Large Multidecadal Salinity Trends near the Pacific–Antarctic Continental Margin. *J. Climate*, 23:4508–4524.

Jenkins, A. (1991). A one-dimensional model of ice shelf-ocean interaction. *J. Geophys. Res.*, 96(C11):20671–20677.

Jenkins, A., Nicholls, K. W., and Coor, H. F. J. (2010). Observation and Parameterization of Ablation at the Base of Ronne Ice Shelf, Antarctica. *J. Phys. Oceanogr.*, 40:2298 – 2312.

Jenkins, A. and Nost, O. A. (2017). A simple diagnostic model of the circulation beneath an ice shelf. In *EGU General Assembly Conference Abstracts*, EGU General Assembly Conference Abstracts, page 10364.

Joughin, I., Smith, B. E., and Schoof, C. G. (2019). Regularized Coulomb friction laws for ice sheet sliding: Application to Pine Island Glacier, Antarctica. *Geophys. Res. Lett.*, 46(9):4764–4771.

Jourdain, N. C., Asay-Davis, X., Hattermann, T., Straneo, F., Seroussi, H., Little, C. M., , and Nowicki, S. (2020). A protocol for calculating basal melt rates in the ISMIP6 Antarctic ice sheet projections. *The Cryosphere*, 14:3111–3134.

Jourdain, N. C., Asay-Davis, X. S., Hattermann, T., Straneo, F., Seroussi, H., Little, C. M., and Nowicki, S. M. J. (in review). Ocean forcing for the ISMIP6 Antarctic ice sheet projections. *The Cryosphere Discuss.*

Jourdain, N. C., Mathiot, P., Merino, N., Durand, G., Le Sommer, J., Spence, P., Dutrieux, P., and Madec, G. (2017). Ocean circulation and sea-ice thinning induced by melting ice shelves in the Amundsen Sea. *J. Geophys. Res. - Oceans*, 122:2550 – 2573.

Khazendar, A., Schodlok, M. P., Fenty, I., Ligtenberg, S. R. M., Rignot, E., and van den Broeke, M. R. (2013). Observed thinning of Totten Glacier is linked to coastal polynya variability. *Nat. Communications*, 4(1):2857.

Larour, E., Seroussi, H., Morlighem, M., and Rignot, E. (2012). Continental scale, high order, high spatial resolution, ice sheet modeling using the ice sheet system model (issm). *J. Geophys. Res.*, 117(F1):1–20.

Lazeroms, W. M. J., Jenkins, A., Gudmundsson, G. H., and van de Wal, R. S. W. (2018). Modelling present-day basal melt rates for Antarctic ice shelves using a parametrization of buoyant meltwater plumes. *Cryosphere*, 12:49–70.

Lenaerts, J. T. M., van den Broeke, M. R., van de Berg, W. J., van Meijgaard, E., and Munneke, P. K. (2012). A new, high-resolution surface mass balance map of Antarctica (1979-2010) based on regional atmospheric climate modeling. *Geophys. Res. Lett.*, 39:1–5.

Lewis, E. L. and Perkin, R. G. (1986). Ice Pumps And Their Rates. *J. Geophys. Res.*, 91(C10):1756–1762.

Li, X., Rignot, E., Morlighem, M., Mouginot, J., and Scheuchl, B. (2015). Grounding line retreat of Totten Glacier, East Antarctica, 1996 to 2013. *Geophys. Res. Lett.*, 42(19):8049–8056.

Li, X., Rignot, E., Mouginot, J., and Scheuchl, B. (2016). Ice flow dynamics and mass loss of Totten Glacier, East Antarctica, from 1989 to 2015. *Geophys. Res. Lett.*, 43(12):6366–6373.

Ligtenberg, S. R. M., van de Berg, W. J., van den Broeke, M. R., Rae, J. G. L., and van Meijgaard, E. (2013). Future surface mass balance of the Antarctic ice sheet and its influence on sea level change, simulated by a regional atmospheric climate model. *Clim. Dynam.*, 41:867–884.

Little, C., Gnanadesikan, A., and Oppenheimer, M. (2009). How ice shelf morphology controls basal melting. *J. Geophys. Res.*, 114:1–14.

Little, C. M., Goldberg, D., Gnanadesikan, A., and Oppenheimer, M. (2012). On the coupled response to ice-shelf basal melting. *J. Glaciol.*, 58.

Locarnini, R. A., Mishonov, A. V., Antonov, J. I., Boyer, T. P., Garcia, H. E., Baranova, O. K., Zweng, M. M., and Johnson, D. R. (2010). *World Ocean Atlas 2009, Volume 1: Temperature*. NOAA Atlas NESDIS 68. U.S. Government Printing Office, Washington, D.C.

Locarnini, R. A., Mishonov, A. V., Baranova, O. K., Boyer, T. P., Zweng, M. M., Garcia, H. E., Reagan, J. R., Seidov, D., Weathers, K. W., Paver, C. R., and Smolyar, I. (2019). World Ocean Atlas 2018, Volume 1: Temperature. NOAA Atlas NESDIS 81.

Losch, M. (2008). Modeling ice shelf cavities in a z coordinate ocean general circulation model. *J. Geophys. Res.*, 113(C8).

Losch, M., Menemenlis, D., Campin, J.-M., Heimbach, P., and Hill, C. (2010). On the formulation of sea-ice models. Part 1: Effects of different solver implementations and parameterizations. *Ocean Model.*, 33(1-2):129–144.

Lovell, A. M., Stokes, C. R., and Jamieson, S. S. R. (2017). Sub-decadal variations in outlet glacier terminus positions in victoria land, oates land and george v land, east antarctica (1972–2013). *Antarct. Sci.*, 29(5):468–483.

MacAyeal, D. R. (1989). Large-scale ice flow over a viscous basal sediment: Theory and application to Ice Stream B, Antarctica. *J. Geophys. Res.*, 94(B4):4071–4087.

Marshall, S. J. and Clarke, G. K. C. (1997). A continuum mixture model of ice stream thermomechanics in the Laurentide Ice Sheet .2. Application to the Hudson Strait Ice Stream. *J. Geophys. Res. - Solid Earth*, 102(B9):20615–20637.

Maule, C., Purucker, M. E., Olsen, N., and Mosegaard, K. (2005). Heat flux anomalies in antarctica revealed by satellite magnetic data. *Science*, 309:464–467.

Morlighem, M., Rignot, E., Binder, T., Blankenship, D., Drews, R., Eagles, G., Eisen, O., Ferraccioli, F., Forsberg, R., Fretwell, P., Goel, V., Greenbaum, J. S., Gudmundsson, H., Guo, J., Helm, V., Hofstede, C., Howat, I., Humbert, A., Jokat, W., Karlsson, N. B., Lee, W. S., Matsuoka, K., Millan, R., Mouginot, J., Paden, J., Pattyn, F., Roberts, J., Rosier, S., Ruppel, A., Seroussi, H., Smith, E. C., Steinhage, D., Sun, B., Broeke, M. R. v. d., Ommen, T. D. v., Wessem, M. v., and Young, D. A. (2020). Deep glacial troughs and stabilizing ridges unveiled beneath the margins of the Antarctic ice sheet. *Nat. Geosci.*, 13(2):132–137.

Morlighem, M., Rignot, E., Seroussi, H., Larour, E., Dhia, H. B., and Aubry, D. (2011). A mass conservation approach for mapping glacier ice thickness. *Geophys. Res. Lett.*, 38.

Morlighem, M., Seroussi, H., Larour, E., and Rignot, E. (2013). Inversion of basal friction in Antarctica using exact and incomplete adjoints of a higher-order model. *J. Geophys. Res.*, 118(3):1746–1753.

Morlighem, M., Williams, C. N., Rignot, E., An, L., Arndt, J. E., Bamber, J. L., Catania, G., Chauché, N., Dowdeswell, J. A., Dorschel, B., Fenty, I., Hogan, K., Howat, I., Hubbard, A., Jakobsson, M., Jordan, T. M., Kjeldsen, K. K., Millan, R., Mayer, L., Mouginot, J., Noël, B. P. Y., O'Cofaigh, C., Palmer, S., Rysgaard, S., Seroussi, H., Siegert, M. J., Slabon, P., Straneo, F., van den Broeke, M. R., Weinrebe, W., Wood, M., and Zinglersen, K. B. (2017). BedMachine v3: Complete bed topography and ocean bathymetry mapping of Greenland from multi-beam echo sounding combined with mass conservation. *Geophys. Res. Lett.*, 44(21):11,051–11,061. 2017GL074954.

Morlighem, M., Wood, M., Seroussi, H., Choi, Y., and Rignot, E. (2019). Modeling the response of northwest Greenland to enhanced ocean thermal forcing and subglacial discharge. *Cryosphere*, 13:723–734.

Mouginot, J., Rignot, E., Bjørk, A. A., van den Broeke, M., Millan, R., Morlighem, M., Noël, B., Scheuchl, B., and Wood, M. (2019a). Forty-six years of greenland ice sheet mass balance from 1972 to 2018. *Proc. Natl. Acad. Sci.*

Mouginot, J., Rignot, E., and Scheuchl, B. (2019b). Continent-wide, interferometric SAR phase, mapping of Antarctic ice velocity. *Geophys. Res. Lett.*, 46(16):9710–9718.

Nakayama, Y., Greene, C. A., Paolo, F. S., Mensah, V., Zhang, H., Kashiwase, H., Simizu, d., Greenbaum, J. S., Blankenship, D. D., Abe-Ouchi, A., and Aoki, S. (submitted). Antarctic Slope Current controls warm ocean intrusions towards Totten Glacier. *Geophys. Res. Lett.*

National Geophysical Data Center, NESDIS, NOAA, U.S. Department of Commerce (2011). Etopo1, global 1 arc-minute ocean depth and land elevation from the us national geophysical data center (ngdc).

Nowicki, S., Goelzer, H., Seroussi, H., Payne, A. J., Lipscomb, W. H., Abe-Ouchi, A., Agosta, C., Alexander, P., Asay-Davis, X. S., Barthel, A., Bracegirdle, T. J., Cullather, R., Felikson, D., Fettweis, X., Gregory, J. M., Hattermann, T., Jourdain, N. C., Kuipers Munneke, P., Larour, E., Little, C. M., Morlighem, M., Nias, I., Shepherd, A., Simon, E., Slater, D., Smith, R. S., Straneo, F., Trusel, L. D., van den Broeke, M. R., and van de Wal, R. (2020). Experimental protocol for sea level projections from ISMIP6 stand-alone ice sheet models. *The Cryosphere*, 14(7):2331–2368.

Nowicki, S. M. J., Payne, A. J., Larour, E., Seroussi, H., Goelzer, H., Lipscomb, W. H., Gregory, J., Abe-Ouchi, A., and Shepherd, A. (2016). Ice Sheet Model Intercomparison Project (ISMIP6) contribution to CMIP6 . *Geosci. Model Dev.*, 9:4521–4545.

Nye, J. F. (1953). The flow law of ice from measurements in glacier tunnels, laboratory experiments and the Jungfraufirn borehole experiment. *Proc. R. Soc. A*, 219(1193):477–489.
Comparison of Glen 1952 compression tests, Gerrard 1952 vertical borehole on Jungfraufirn, and behavior of cylindrical tunnel closure. Equations for 3D slow flow of ice mass: general flow law.

Pachauri, R. K., Allen, M. R., Barros, V. R., Broome, J., Cramer, W., Christ, R., Church, J. A., Clarke, L., Dahe, Q., Dasgupta, P., Dubash, N. K., Edenhofer, O., Elgizouli, I., Field, C. B., Forster, P., Friedlingstein, P., Fuglestvedt, J., Gomez-Echeverri, L., Hallegatte, S., Hegerl, G., Howden, M., Jiang, K., Jimenez Cisneroz, B., Kattsov, V., Lee, H., Mach, K. J., Marotzke, J., Mastrandrea, M. D., Meyer, L., Minx, J., Mulugetta, Y., O'Brien, K., Oppenheimer, M., Pereira, J. J., Pichs-Madruga, R., Plattner, G. K., Pörtner, H.-O., Power, S. B., Preston, B., Ravindranath, N. H., Reisinger, A., Riahi, K., Rusticucci, M., Scholes, R., Seyboth, K., Sokona, Y., Stavins, R., Stocker, T. F., Tschakert, P., van Vuuren, D., and van Ypserle, J. P. (2014). Climate Change 2014: Synthesis Report. Contribution of Working Groups I, II and III to the Fifth Assessment Report of the Intergovernmental Panel on Climate Change. *EPIC3Geneva, Switzerland, IPCC, 151 p., pp. 151, ISBN: 978-92-9169-143-2.*

Paolo, F., Fricker, H. A., and Padman, L. (2015). Volume loss from Antarctic ice shelves is accelerating. *Science*, 348.

Pattyn, F. (2003). A new three-dimensional higher-order thermomechanical ice sheet model: Basic sensitivity, ice stream development, and ice flow across subglacial lakes. *J. Geophys. Res.*, 108(B8):1–15.

Pelle, T., Morlighem, M., and Bondzio, J. H. (2019). Brief communication: PICOP, a new ocean melt parameterization under ice shelves combining PICO and a plume model. *Cryosphere*, 13(3):1043–1049.

Pelle, T., Morlighem, M., and McCormack, F. S. (2020). Aurora Basin, the Weak Underbelly of East Antarctica. *Geophys. Res. Lett.*, 47(9):e2019GL086821.

Petty, A. A., Feltham, D. L., and Holland, P. R. (2013). Impact of Atmospheric Forcing on Antarctic Continental Shelf Water Masses. *Journal of Physical Oceanography*, 43(5):920–940.

Pritchard, H. D., Ligtenberg, S. R. M., Fricker, H. A., Vaughan, D. G., van den Broeke, M. R., and Padman, L. (2012). Antarctic ice-sheet loss driven by basal melting of ice shelves. *Nature*, 484(7395):502–505.

Reese, R., Albrecht, T., Mengel, M., Asay-Davis, X., and Winkelmann, R. (2018). Antarctic sub-shelf melt rates via PICO. *The Cryosphere*, 12:1969–1985.

Rignot, E., Jacobs, S., Mouginot, J., and Scheuchl, B. (2013). Ice shelf melting around Antarctica. *Science*, 341(6143):266–270.

Rignot, E. and Jacobs, S. S. (2002). Rapid bottom melting widespread near Antarctic ice sheet grounding lines. *Science*, 296(5575):2020–2023.

Rignot, E., Mouginot, J., and Scheuchl, B. (2011). Ice Flow of the Antarctic Ice Sheet. *Science*, 333(6048):1427–1430.

Rignot, E., Mouginot, J., Scheuchl, B., van den Broeke, M., van Wessem, M. J., and Morlighem, M. (2019). Four decades of Antarctic Ice Sheet mass balance from 1979–2017. *Proc. Natl. Acad. Sci.*, 116(4):1095–1103.

Rintoul, S. R., Silvano, A., Pena-Molino, B., van Wijk, E., Rosenberg, M., Greenbaum, J. S., and Blankenship, D. D. (2016). Ocean heat drives rapid basal melt of the Totten Ice Shelf. *Sci. Adv.*, 2(12).

Roberts, J., Galton-Fenzi, B. K., Paolo, F. S., Donnelly, C., Gwyther, D. E., Padman, L., Young, D., Warner, R., Greenbaum, J., Fricker, H. A., Payne, A. J., Cornford, S., Le Brocq, A., van Ommen, T., Blankenship, D., and Siegert, M. J. (2018). Ocean forced variability of totten glacier mass loss. *Geological Society, London, Special Publications*, 461(1):175–186.

Roquet, F., Guinet, C., Charrassin, J.-B., Costa, D. P., Kovacs, K. M., Lydersen, C., Bornemann, H., Bester, M. N., Muelbert, M. C., Hindell, M. A., McMahon, C. R., Harcourt, R., Boehme, L., and Fedak, M. A. (2018). MEOP-CTD in-situ data collection: a Southern ocean Marine-mammals calibrated sea water temperatures and salinities observations.

Schmidtko, S., Heywood, K. J., Thompson, A. F., and Aoki, S. (2014). Multidecadal warming of Antarctic waters. *Science*, 346(6214).

Schoof, C. (2007). Ice sheet grounding line dynamics: Steady states, stability, and hysteresis. *J. Geophys. Res.*, 112(F03S28):1–19.

Seroussi, H. (2011). *Modeling ice flow dynamics with advanced multi-model formulations*. PhD thesis, Ecole Centrale Paris.

Seroussi, H. and Morlighem, M. (2018). Representation of basal melting at the grounding line in ice flow models. *Cryosphere*, 12(10):3085–3096.

Seroussi, H., Morlighem, M., Larour, E., Rignot, E., and Khazendar, A. (2014). Hydrostatic grounding line parameterization in ice sheet models. *Cryosphere*, 8(6):2075–2087.

Seroussi, H., Morlighem, M., Rignot, E., Khazendar, A., Larour, E., and Mouginot, J. (2013). Dependence of century-scale projections of the Greenland ice sheet on its thermal regime. *J. Glaciol.*, 59(218):1024–1034.

Seroussi, H., Nakayama, Y., Larour, E., Menemenlis, D., Morlighem, M., Rignot, E., and Khazendar, A. (2017). Continued retreat of Thwaites Glacier, West Antarctica, controlled by bed topography and ocean circulation. *Geophys. Res. Lett.*, 44(12):6191–6199.

Seroussi, H., Nowicki, S., Payne, A. J., Goelzer, H., Lipscomb, W. H., Abe-Ouchi, A., Agosta, C., Albrecht, T., Asay-Davis, X., Barthel, A., Calov, R., Cullather, R., Dumas, C., Galton-Fenzi, B. K., Gladstone, R., Golledge, N. R., Gregory, J. M., Greve, R., Hattermann, T., Hoffman, M. J., Humbert, A., Huybrechts, P., Jourdain, N. C., Kleiner, T., Larour, E., Leguy, G. R., Lowry, D. P., Little, C. M., Morlighem, M., Pattyn, F., Pelle, T., Price, S. F., Quiquet, A., Reese, R., Schlegel, N.-J., Shepherd, A., Simon, E., Smith, R. S., Straneo, F., Sun, S., Trusel, L. D., Van Breedam, J., van de Wal, R. S. W., Winkelmann, R., Zhao, C., Zhang, T., and Zwinger, T. (2020). ISMIP6 Antarctica: a multi-model ensemble of the Antarctic ice sheet evolution over the 21st century. *The Cryosphere*, 14:3033–3070.

Shepherd, A., Ivins, E., Rignot, E., Smith, B., van den Broeke, M., Velicogna, I., Whitehouse, P., Briggs, K., Joughin, I., Krinner, G., Nowicki, S., Payne, T., Scambos, T., Schlegel, N., Geruo, A., Agosta, C., Ahlstrom, A., Babonis, G., Barletta, V., Blazquez, A., Bonin, J., Csatho, B., Cullather, R., Felikson, D., Fettweis, X., Forsberg, R., Gallee, H., Gardner, A., Gilbert, L., Groh, A., Gunter, B., Hanna, E., Harig, C., Helm, V., Horvath, A., Horwath, M., Khan, S., Kjeldsen, K. K., Konrad, H., Langen, P., Lecavalier, B., Loomis, B., Luthcke, S., McMillan, M., Melini, D., Mernild, S., Mohajerani, Y., Moore, P., Mouginot, J., Moyano, G., Muir, A., Nagler, T., Nield, G., Nilsson, J., Noel, B., Otosaka, I., Pattle, M. E., Peltier, W. R., Pie, N., Rietbroek, R., Rott, H., Sandberg-Sorensen, L., Sasgen, I., Save, H., Scheuchl, B., Schrama, E., Schroeder, L., Seo, K.-W., Simonsen, S., Slater, T.,

Spada, G., Sutterley, T., Talpe, M., Tarasov, L., van de Berg, W. J., van der Wal, W., van Wessem, M., Vishwakarma, B. D., Wiese, D., Wouters, B., and Team, I. (2018). Mass balance of the Antarctic ice sheet from 1992 to 2017. *Nature*, 558(7709):219+.

Sun, S., Conford, S. L., Gwyther, D. E., and Gladstone, R. M. (2016). Impact of ocean forcing on the Aurora Basin in the 21st and 22nd centuries. *Ann. Glaciol.*, 57(73):79–86.

Taylor, K. E., Stouffer, R. J., and Meehl, G. A. (2012). An Overview of CMIP5 and the experiment design. *Bull. Amer. Meteor. Soc.*, 93:485–498.

Timmermann, R., Wang, Q., and Hellmer, H. H. (2012). Ice-shelf basal melting in a global finite-element sea-ice/ice-shelf/ocean model. *Ann. Glaciol.*, 53(60):303–314.

van den Broeke, M. R. (2019). RACMO2.3p1 annual surface mass balance Antarctica (1979-2014).

van den Broeke, M. R., Enderlin, E. M., Howat, I. M., Munneke, P. K., Noel, B. P. Y., van de Berg, W. J., van Meijgaard, E., and Wouters, B. (2016). On the recent contribution of the Greenland ice sheet to sea level change. *Cryosphere*, 10(5):1933–1946.

van der Veen, C. J. and Whillans, I. M. (1989). Force budget: I. Theory and numerical methods. *J. Glaciol.*, 35:53–60.

van Wessem, J. M., Reijmer, C. H., Morlighem, M., Mouginot, J., Rignot, E., Medley, B., Joughin, I., Wouters, B., Depoorter, M. A., Bamber, J. L., Lenaerts, J. T. M., van de Berg, W. J., van den Broeke, M. R., and van Meijgaard, E. (2014). Improved representation of East Antarctic surface mass balance in a regional atmospheric climate model. *J. Glaciol.*, 60(222):761–770.

Weertman, J. (1974). Stability of the junction of an ice sheet and an ice shelf. *J. Glaciol.*, 13(67):3–11.

Zhang, H., Menemenlis, D., and Fenty, I. (2018). ECCO LLC270 Ocean-Ice State Estimate (ECCO Consortium). http://doi.org/1721.1/119821.

Zwally, H. J., Giovinetto, M. B., Beckley, M. A., and Saba, J. L. (2012). Antarctic and greenland drainage systems. *GSFC Cryospheric Sciences Laboratory*.

Appendix A

Ice flow modeling: A mathematical formalism

In general, models in the physical sciences are approximations of physical processes that are described through the language of mathematics. As approximations, these models will always be an incomplete representation of a real system. When utilized to investigate relevant problems and when derived with appropriate assumptions, however, such models can provide scientists with insights into processes that are difficult to observe and/or quantify. In particular, glacier and ice sheet models result from the mathematical representation of two fundamental processes, ice sheet mass balance and glacial flow. Expressing these two processes in an ice sheet model requires an understanding of the broad range of processes that drive their evolution (i.e. firn compaction, iceberg calving, ocean induced ice shelf basal melting, basal properties, etc). At present, the broad range of existing ice sheet models reflects the diverse nature of processes they are used to investigate; yet, each model is rooted in the same underlying physics. In order to interpret the behavior and output of ice sheet models, it is key to first understand the mathematical building-blocks that are used to represent the flow of ice.

In this appendix, we detail the mechanical equations that govern the flow of glaciers and ice sheets. Next, we provide insight into the hierarchy of existing ice flow models, starting from the most complex, three-dimensional model and working down to a simplified two-dimensional approximation.

A.1 Mechanical equations of ice flow

Coming as a surprise to many, ice is a moving fluid, so we are able to describe its motion with a velocity field $\mathbf{v}$(x,y,z,t). Now liquids with a lower viscosity, such as water, are "typical" incompressible fluids (i.e. flow of a fluid in which the divergence of the flow velocity is zero). To model such flow, we use the Navier-Stokes equations:

$$\begin{aligned} \nabla \cdot \mathbf{v} &= 0 && \text{Incompressibility} \\ \rho\left(\mathbf{v_t} + \mathbf{v} \cdot \nabla \mathbf{v}\right) &= \nabla \cdot (\nu \nabla \mathbf{v}) - \nabla P + \rho \boldsymbol{g} && \text{Stress Balance} \end{aligned} \tag{A.1}$$

where ρ is the density of ice, ν is the fluid's viscosity, P is the pressure field, and g is Earth's gravitational constant. The first equation is the definition of incompressibility, while the second equation describes the stress balance of the incompressible fluid. In the second equation, the term $\mathbf{v_t} + \mathbf{v} \cdot \nabla \mathbf{v}$ is an acceleration, while the right hand side is the total stress. That is, the second equation is a restructuring of Newton's second law, *Force* = *Mass* $\times$ *Acceleration*. As a slow fluid, the flow of ice is not impacted by accelerations as readily as typical imcompressible fluids (e.g. the Coriolis force). This means that in the second equation above, we can make the assumption that $\rho\left(\mathbf{v_t} + \mathbf{v} \cdot \nabla \mathbf{v}\right) \approx \mathbf{0}$. In addition, ice is also a sheer-thinning fluid with a nonlinear-viscous behavior. As such, a separate flow law must be derived to describe this nonlinear behavior.

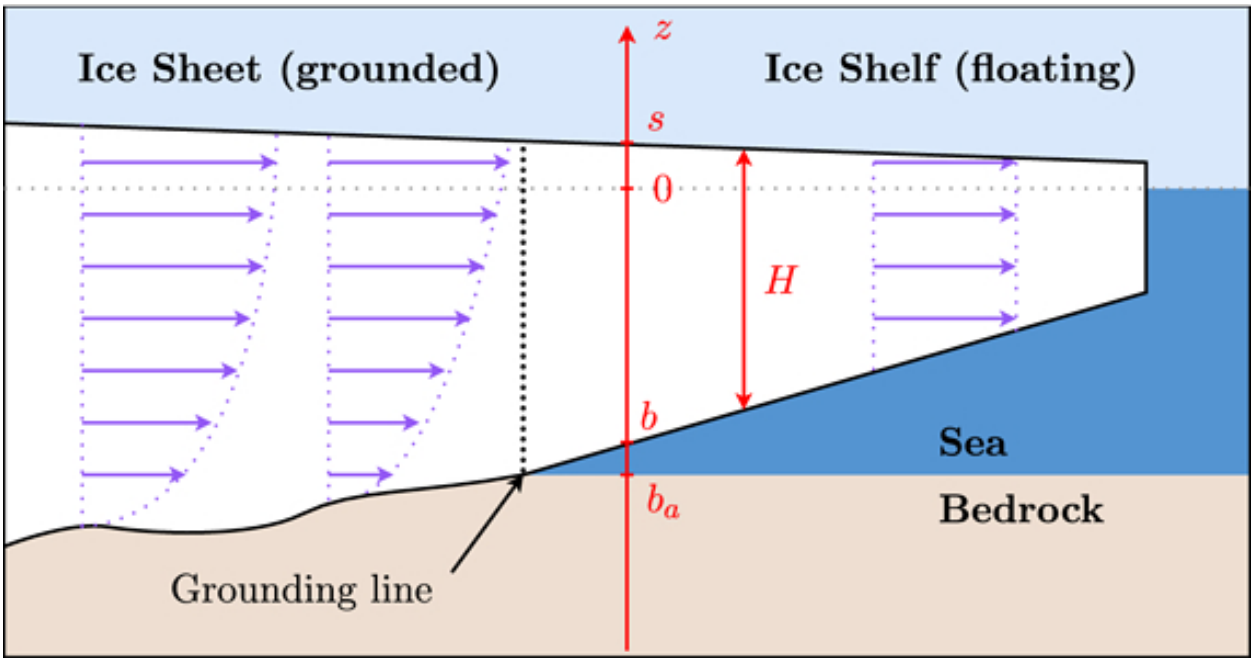

Figure A.1: Schematic diagram showing a glacial cross section with purple arrows depicting a simplified representation of ice flow near the grounding line. Ice geometry reference variables are labeled in red. This figure was adapted from Larour et al. (2012).

With these changes in mind, we give the mechanical equations describing ice flow below:

$$\begin{aligned}
\nabla \cdot \mathbf{v} = Tr\left(\dot{\boldsymbol{\varepsilon}}\right) &= 0 && \text{Incompressibilty} \\
\nabla \cdot \boldsymbol{\sigma'} - \nabla P + \rho \boldsymbol{g} &= \mathbf{0} && \text{Stress Balance} \\
\boldsymbol{\sigma'} &= 2\mu\dot{\boldsymbol{\varepsilon}} && \text{Ice constitutive law} \\
\mu &= \frac{\mathrm{B}}{2\,\dot{\varepsilon}_e^{\frac{n-1}{n}}} && \text{Glen's flow law,}
\end{aligned} \tag{A.2}$$

where $\boldsymbol{\sigma'} = \boldsymbol{\sigma} + p\mathbf{I}$ is the Cauchy deviatoric stress tensor, $\mathbf{I}$ is the identity matrix, Tr is the trace operator, $\dot{\varepsilon}$ is the strain rate tensor, μ is the ice effective viscosity, B is the ice hardness, and n is Glen's flow law coefficient (typically n = 3). Together, the ice constitutive law and generalized form of Glen's flow law describe the nonlinear viscous flow of ice (Glen, 1958; Nye, 1953).

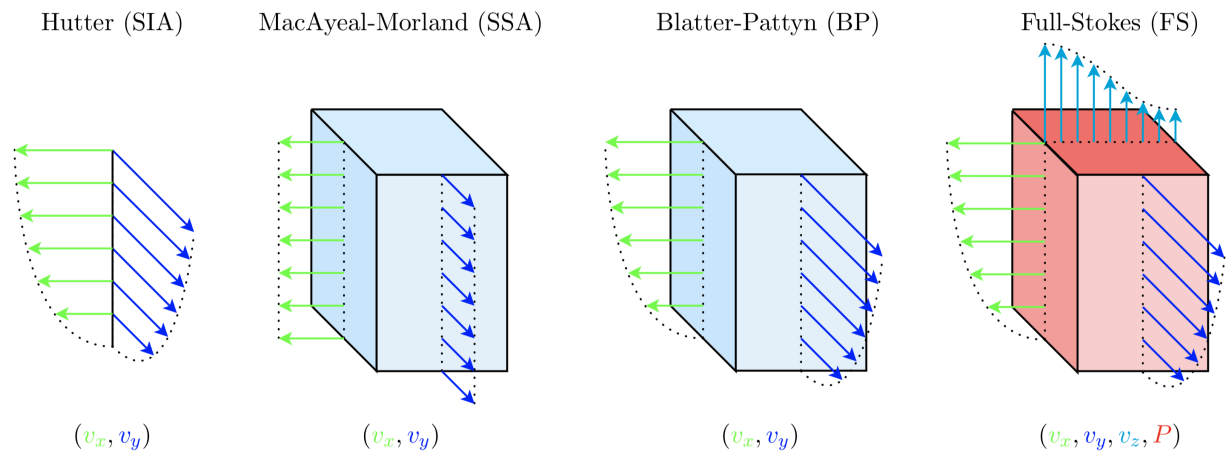

Figure A.2: Schematic diagram showing unknown variables for the Full Stokes, Higher order, and Shelfy-Stream approximation, and shallow ice approximation ice flow models.

A.2 Ice Flow Models

Numerical ice flow models solve the system of equations given in equation 2.2 for select components of the ice velocity and/or pressure fields, depending on the level of complexity of the model (see figure A.2). We begin our analysis with the most complex plan-view ice flow model, the full-Stokes solution. From there, we describe the assumptions that are made in order to derive more efficient, simplified approximations to the full solution.

A.2.1 Full-Stokes

The full-Stokes ice sheet model is a three-dimensional ice flow model that solves the complete set of partial differential equations given in equation 2.2 for four unknown variables (v_x, v_y, v_z, P, see figure A.2). By using the ice constitutive law and Glen's flow law, the stress

balance equation can be rewritten in terms of its velocity components and pressure field:

$$\begin{cases} \dfrac{\partial}{\partial \mathrm{x}}\left(2\mu\dfrac{\partial \mathrm{v_x}}{\partial \mathrm{x}}\right)+\dfrac{\partial}{\partial \mathrm{y}}\left(\mu\dfrac{\partial \mathrm{v_x}}{\partial \mathrm{y}}+\mu\dfrac{\partial \mathrm{v_y}}{\partial \mathrm{x}}\right)+\dfrac{\partial}{\partial \mathrm{z}}\left(\mu\dfrac{\partial \mathrm{v_x}}{\partial \mathrm{z}}+\mu\dfrac{\partial \mathrm{v_z}}{\partial \mathrm{x}}\right)-\dfrac{\partial \mathrm{p}}{\partial \mathrm{x}}=0 \\ \dfrac{\partial}{\partial \mathrm{x}}\left(\mu\dfrac{\partial \mathrm{v_x}}{\partial \mathrm{y}}+\mu\dfrac{\partial \mathrm{v_y}}{\partial \mathrm{x}}\right)+\dfrac{\partial}{\partial \mathrm{y}}\left(2\mu\dfrac{\partial \mathrm{v_y}}{\partial \mathrm{y}}\right)+\dfrac{\partial}{\partial \mathrm{z}}\left(\mu\dfrac{\partial \mathrm{v_y}}{\partial \mathrm{z}}+\mu\dfrac{\partial \mathrm{v_z}}{\partial \mathrm{y}}\right)-\dfrac{\partial \mathrm{p}}{\partial \mathrm{y}}=0 \\ \dfrac{\partial}{\partial \mathrm{x}}\left(\mu\dfrac{\partial \mathrm{v_x}}{\partial \mathrm{z}}+\mu\dfrac{\partial \mathrm{v_z}}{\partial \mathrm{x}}\right)+\dfrac{\partial}{\partial \mathrm{y}}\left(\mu\dfrac{\partial \mathrm{v_y}}{\partial \mathrm{z}}+\mu\dfrac{\partial \mathrm{v_z}}{\partial \mathrm{y}}\right)+\dfrac{\partial}{\partial \mathrm{z}}\left(2\mu\dfrac{\partial \mathrm{v_z}}{\partial \mathrm{z}}\right)-\dfrac{\partial \mathrm{p}}{\partial \mathrm{z}}-\rho g=0 \\ \dfrac{\partial \mathrm{v_x}}{\partial \mathrm{x}}+\dfrac{\partial \mathrm{v_y}}{\partial \mathrm{y}}+\dfrac{\partial \mathrm{v_z}}{\partial \mathrm{z}}=0, \end{cases} \tag{A.3}$$

where z is the vertical coordinate. As the full-Stokes model solves for all nine stress tensors, it is computationally expensive and virtually impossible to implement in continental-scale ice sheet simulations. However, it has been shown that the simulated evolution of a glacier can be sensitive to changes in the *complete* stress field within the vicinity of the grounding line (Larour et al., 2012). That is, accurate modeling of the evolution of a glacier's grounding line might require use of the full-Stokes solution.

A.2.2 Higher order

The next step down in complexity from the full-Stokes solution is the higher-order model from Blatter (1995) and Pattyn (2003), in which two assumptions are made: **(1)** horizontal gradients in vertical velocity are negligible compared to vertical gradients of horizontal velocity:

$$\dot{\varepsilon}_{xz}=\frac{1}{2}\frac{\partial \mathrm{v_x}}{\partial \mathrm{z}} \qquad \dot{\varepsilon}_{yz}=\frac{1}{2}\frac{\partial \mathrm{v_y}}{\partial \mathrm{z}}\ ,$$

and **(2)** bridging effects are negligible (i.e. vertical sheer stresses can be assumed to be negligable when compared to horizontal sheer stresses, van der Veen and Whillans, 1989).

These two simplifying assumptions allow us to neglect the red terms in equation A.3, effectively reducing the number of unknown variables to v_x and v_y (v_z is recovered through the imcompressibility equation, figure A.2). This, in turn, reduces the full-Stokes model to the following:

$$\begin{cases} \dfrac{\partial}{\partial x}\left(4\mu\dfrac{\partial v_x}{\partial x}+2\mu\dfrac{\partial v_y}{\partial y}\right)+\dfrac{\partial}{\partial y}\left(\mu\dfrac{\partial v_x}{\partial y}+\mu\dfrac{\partial v_y}{\partial x}\right)+\dfrac{\partial}{\partial z}\left(\mu\dfrac{\partial v_x}{\partial z}\right)-\rho g\dfrac{\partial s}{\partial x}=0 \\ \dfrac{\partial}{\partial x}\left(\mu\dfrac{\partial v_x}{\partial y}+\mu\dfrac{\partial v_y}{\partial x}\right)+\dfrac{\partial}{\partial y}\left(4\mu\dfrac{\partial v_y}{\partial y}+2\mu\dfrac{\partial v_x}{\partial x}\right)+\dfrac{\partial}{\partial z}\left(\mu\dfrac{\partial v_y}{\partial z}\right)-\rho g\dfrac{\partial s}{\partial y}=0 \\ \dfrac{\partial}{\partial z}\left(2\mu\dfrac{\partial v_z}{\partial z}\right)-\dfrac{\partial p}{\partial z}-\rho g=0 \end{cases} \quad \text{(A.4)}$$

While the higher-order model is computationally more efficient than the full-Stokes model, it is still a three-dimensional model, making it less suitable for full continental-scale projections.

A.2.3 Shelfy-Stream approximation

Simplifying further from the higher-order model brings us to the Shallow-Shelf or Shelfy-Stream Approximation (SSA, MacAyeal, 1989), in which longitudinal stresses dominate and vertical shear is assumed to be negligible:

$$\dot{\varepsilon}_{xz}=0 \qquad \dot{\varepsilon}_{yz}=0.$$

This renders the first two equations in equation A.4 independent of z, leaving us with two unknowns (v_x and v_y, figure A.2). This allows us to neglect the blue and red terms in

equation A.3 and by depth averaging, we obtain:

$$\begin{cases} \dfrac{\partial}{\partial \mathrm{x}}\left(4\mathrm{H}\bar{\mu}\dfrac{\partial \mathrm{v_x}}{\partial \mathrm{x}} + 2\mathrm{H}\bar{\mu}\dfrac{\partial \mathrm{v_y}}{\partial \mathrm{y}}\right) + \dfrac{\partial}{\partial \mathrm{y}}\left(\mathrm{H}\bar{\mu}\dfrac{\partial \mathrm{v_x}}{\partial \mathrm{y}} + \mathrm{H}\bar{\mu}\dfrac{\partial \mathrm{v_y}}{\partial \mathrm{x}}\right) - \rho g \mathrm{H}\dfrac{\partial \mathrm{s}}{\partial \mathrm{x}} = 0 \\ \dfrac{\partial}{\partial \mathrm{x}}\left(\mathrm{H}\bar{\mu}\dfrac{\partial \mathrm{v_x}}{\partial \mathrm{y}} + \mathrm{H}\bar{\mu}\dfrac{\partial \mathrm{v_y}}{\partial \mathrm{x}}\right) + \dfrac{\partial}{\partial \mathrm{y}}\left(4\mathrm{H}\bar{\mu}\dfrac{\partial \mathrm{v_y}}{\partial \mathrm{y}} + 2\mathrm{H}\bar{\mu}\dfrac{\partial \mathrm{v_x}}{\partial \mathrm{x}}\right) - \rho g \mathrm{H}\dfrac{\partial \mathrm{s}}{\partial \mathrm{y}} = 0, \end{cases} \tag{A.5}$$

where $\bar{\mu}$ is the depth averaged ice viscosity, H is the local ice thickness, and s is the upper surface elevation (see figure A.1). This model was originally developed to model ice shelves, as basal sheer stresses are minimal along the ice/ocean interface. Near grounding lines and ice divides, however, where basal shear stresses increase, this model becomes less applicable. In non-idealized applications, there is typically little difference in output between SSA and HO solutions, making this approximation especially useful in longer-duration and larger-scale ice sheet simulations (Larour et al., 2012). In chapters 3 and 4, the century-scale ice sheet projections that were presented have been made using the Shelfy-Stream approximation to the Full-Stokes model (see sections 3.1.1 and 4.1.1 for complete numerical model descriptions).

A.2.4 Shallow ice approximation

The simplest ice flow model we will derive is the Shallow Ice Approximation (SIA, Hutter, 1982), in which only the deviatoric stress components $\sigma_{\mathrm{xz}'}$ and $\sigma_{\mathrm{yz}'}$ are included. That is, the SIA model neglects longitudinal (along flow stretching and compressing) and transverse (drag against slower ice or bedrock) stresses, as well as vertical stress gradients, reducing the full-Stokes equations to:

$$\begin{cases} \dfrac{\partial}{\partial \mathrm{z}}\left(\mu\dfrac{\partial \mathrm{v_x}}{\partial \mathrm{z}}\right) - \rho g \dfrac{\partial \mathrm{s}}{\partial \mathrm{x}} = 0 \\ \dfrac{\partial}{\partial \mathrm{z}}\left(\mu\dfrac{\partial \mathrm{v_y}}{\partial \mathrm{z}}\right) - \rho g \dfrac{\partial \mathrm{s}}{\partial \mathrm{y}} = 0 \end{cases} \tag{A.6}$$

The SIA ice flow model is computationally efficient and is primarily used to model ice in slower regions of flow (e.g. near interior sectors of an ice sheet), but quickly loses accuracy in regions of fast flow (e.g. ice streams). Typically, this model is used in large-scale ice sheet model projections (e.g. ice sheet reconstructions of past epochs).

A.2.5 Boundary conditions

In addition to the primary equations that govern the flow of ice, prescribing conditions that occur at the lateral boundaries of our ice flow model is key in developing a stable numerical model (see table 2.1). The ice sheet model boundary Γ is typically partitioned into parts that represent the surface (ice-air interface, Γ_s), ice that is resting on bedrock (ice-bedrock interface, Γ_b), parts of the ice sheet that are submerge in water (ice-ocean interface, Γ_w), and lateral ice boundaries (Γ_u), such that $\Gamma = \Gamma_s \bigcup \Gamma_b \bigcup \Gamma_w \bigcup \Gamma_u$. The ice-air interface is assumed to be a "free surface", in which the atmosphere does not exert any pressure on the underlying ice. That is, it is typically assumed that the stresses exerted by atmospheric pressure and winds, as well as the impacts of accumulation and ablation, are negligible. Similarly, along the ice-ocean boundary, it is assumed that stresses that act parallel to the ice-ocean interface are insignificant and that melt and refreezing processes do not significantly impact the stress regime of the ice sheet system. However, the stresses acting normal to the ice-ocean interface (i.e. hydrostatic water pressure) are significant and act as the boundary condition for Γ_w.

Along the ice-bedrock interface, we assume the ice cannot penetrate the bedrock. This is especially true if the ice sheet is sliding along a hard bed. This amounts to assuming that the velocity component normal to the ice-bedrock interface is zero. In the tangential direction, stresses applied to the ice sheet are related to the basal velocity through a "sliding law". That is, the tangential basal ice velocity $v_{||}$ is translated to lateral friction by a spatially varying coefficient of basal drag β. Most often, β is inferred from observational data through

inverse modelling techniques (Morlighem et al., 2011). Along the side boundaries of the ice sheet model domain, we specify that the ice velocity solution must be taken from available observations, which is defined as a "Dirichlet" boundary condition. We synthesize these ice flow model boundary conditions in table A.1:

Boundary	**Condition**	**Symbol**	**Mathematical Expression**
Ice/Air interface	free surface	Γ_s	$\boldsymbol{\sigma} \cdot \mathbf{n} = \mathrm{P}_{\mathrm{atm}}\mathbf{n} \simeq \mathbf{0}$
Ice/Ocean interface	water pressure	Γ_w	$\boldsymbol{\sigma} \cdot \mathbf{n} = \mathrm{P}_{\mathrm{w}}\mathbf{n}$
Ice/Bedrock interface	lateral friction	Γ_b	$(\boldsymbol{\sigma} \cdot \mathbf{n} + \boldsymbol{\beta}\mathbf{v})_{\|\|} = 0$
Ice/Bedrock interface	impenetrability	Γ_b	$\mathbf{v} \cdot \mathbf{n} = 0$
Side boundaries	Dirichlet	Γ_v	$\mathbf{v} = \mathbf{v_{obs}}$

Table A.1: Ice flow model boundary condition descriptions

A.3 Inversions for unknown fields

In the system of partial differential equations given in equation A.2 and the boundary conditions in table A.1, there exist unmeasurable fields that have a major impact on the calculated stress regime of the glacial system. In Glen's flow law, the depth averaged ice hardness (or rigidity) field B is used in the computation of the ice effective viscosity, which is then used to solve for the stress tensors that drive ice flow. In addition, the coefficient of basal drag, β, is used in setting the lateral friction boundary condition at the ice/bedrock interface. Parameterizing basal sliding in ice sheet models is still an active area of research and has been shown to produce a wide range of ice sheet behavior (Joughin et al., 2019). These parameters are key controls on ice sheet mechanics and yet, cannot be systematically measured. To surmount this hurdle, inverse methods that combine ice sheet modeling with surface ice sheet observations have been developed to infer both B and β in ISSM (Seroussi, 2011; Larour et al., 2012; Morlighem et al., 2013).

Simply put, the spatial patterns of the basal friction coefficient and the depth averaged ice hardness are computed such that they minimize the misfit between modeled and measured

surface ice velocity (or thickness) (Morlighem et al., 2013). Following the methodology outlined in Morlighem et al. (2013), we first construct a cost function $\mathcal{J}$ that minimizes the misfit between the modeled $\boldsymbol{v} = (v_x, v_y)$ and observed $\boldsymbol{v^{obs}} = \left(v_x^{\text{obs}}, v_y^{\text{obs}}\right)$ surface ice velocity field. The ice sheet model configurations presented in chapters 3 and 4 were initialized with both B and β that were inferred using the following cost function:

$$\begin{aligned}
\mathcal{J}(\boldsymbol{v}, \alpha) = \quad & \gamma_1 \quad \frac{1}{2}\int_{\Gamma_s} \left(v_x - v_x^{\text{obs}}\right)^2 + \left(v_y - v_y^{\text{obs}}\right)^2 \, \mathrm{d}\Gamma_s && \text{Absolute Misfit} \\
+ \quad & \gamma_2 \quad \frac{1}{2}\int_{\Gamma_s} \ln\left(\frac{\sqrt{v_x^2 + v_y^2} + \varepsilon}{\sqrt{v_x^{obs2} + v_y^{obs2}} + \varepsilon}\right)^2 \, \mathrm{d}\Gamma_s && \text{Logarithmic Misfit} \\
+ \quad & \gamma_3 \quad \frac{1}{2}\int_{\Gamma_b} \nabla\alpha \cdot \nabla\alpha \, \mathrm{d}\Gamma_b \, , && \text{Regularization}
\end{aligned} \tag{A.7}$$

where $\alpha \in (B, \beta)$, ε is the minimum velocity needed to avoid the observed velocity being equal to zero (avoids singularities), Γ_s and Γ_b are the respective ice/air and ice/bedrock interfaces, and γ_i where $i \in [1, 2, 3]$ are nondimensionalizing constants used to weigh each term in $\mathcal{J}$. The three terms in the cost function above allow us to infer the parameters of interest across a wide range of ice flow patterns. For instance, term 1 (the absolute misfit) measures the square of the difference between the modeled and observed ice velocity. This term is standard and particularly efficient for the treatment of fast-flowing regions, like ice streams. Term 2 (the logarithmic misfit) measures the square of the logarithmic difference between modeled and observed ice velocity and accounts for slower ice flow (i.e. upstream near ice divides where flow is nearly stagnant) (Morlighem et al., 2013). The last term is a Tikhonov regularization term which penalizes oscillations of α, stabilizing the inversion. In addition to the individual terms used to define $\mathcal{J}$ above, there exist other cost functions based on the misfit of modeled and measured ice thickness.

As seen in figure A.3, the spatial distribution of β features higher friction coefficient values along the ice divides and in regions of slower flow. Along ice streams, such as those located along the Amundsen Sea (i.e. Pine Island Glacier and Thwaites Glacier), computed values

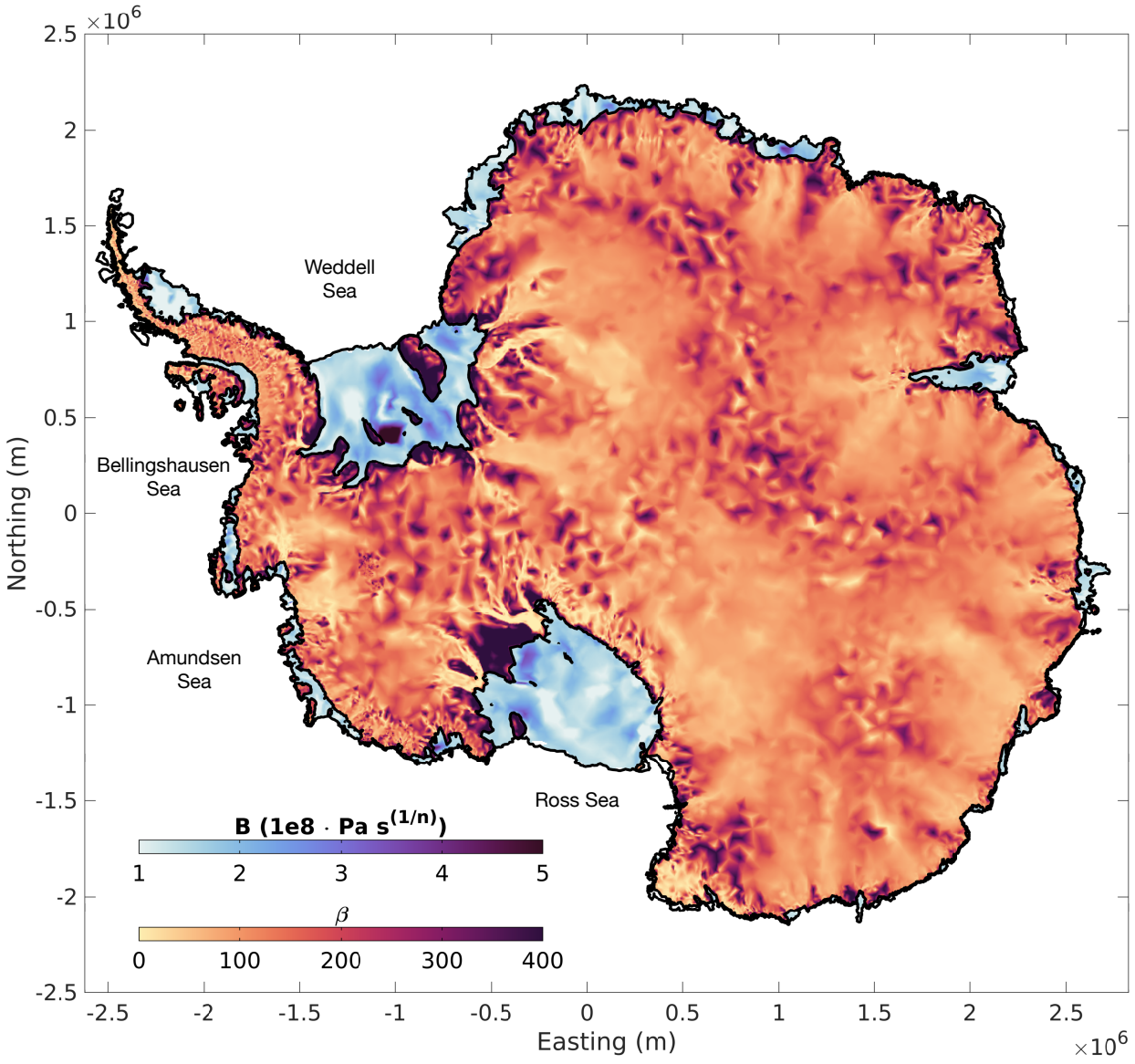

Figure A.3: The coefficient of basal friction (kPa) and the ice hardness parameter (B, $\mathrm{PaS}^{1/\mathrm{n}}$) are plotted over AIS grounded and floating ice, respectively. Note the colorbar ticks associated with B are multiplied by 10^8. Major seas are names along the Antarctic Coast.

of the friction coefficient remain low. This is also the case in low laying and fast flowing sectors of the East Antarctic Ice Sheet, such as in the Aurora and Wilkes Subglacial Basins. As faster flowing regions of ice typically slide on the underlying bedrock more readily than in slower flowing regions, the inferred patterns of β appear consistent. In addition, the ice hardness parameter (B) increases in the vicinity of large-scale topographic pinning points (e.g. islands along the Filchner-Ronne ice shelf). Overall, the inverse methods that have been integrated into ISSM to solve for the coefficient of basal friction and the depth integrated ice hardness parameter are efficient and produce spatial patterns that are consistent with the modern understanding of these fields. With both of these fields solved for, the system of mechanical ice flow equations can now be solved for using the finite element method.

A.4 Unstructured mesh generation

In order to solve the above systems of partial differential equations for the stress balance of a glacial system, the finite element method is invoked. The finite element method is widely used to model the flow of fluids and begins with the system of interest being subdivided into small pieces, called "finite elements". Discritization of a system requires the use of a "mesh", which is essentially the numerical domain of the solution that contains a finite number of points (or vertices). Once the mesh is defined, the original boundary value problem is broken down into a system of algebraic equations in which a solution is approximated through minimization of an associated error function. That is, the finite element method provides an approximation of the true solution over the domain that is defined on a mesh.

In the ice sheet modeling community, specific focus has been paid to develop methods to construct appropriate model grids and meshes, as element size has been found to influence the accuracy of the modeled solution (Larour et al., 2012). For instance, Seroussi et al. (2014) found that in ice sheet models that employ a sub-element grounding line parameterization (a

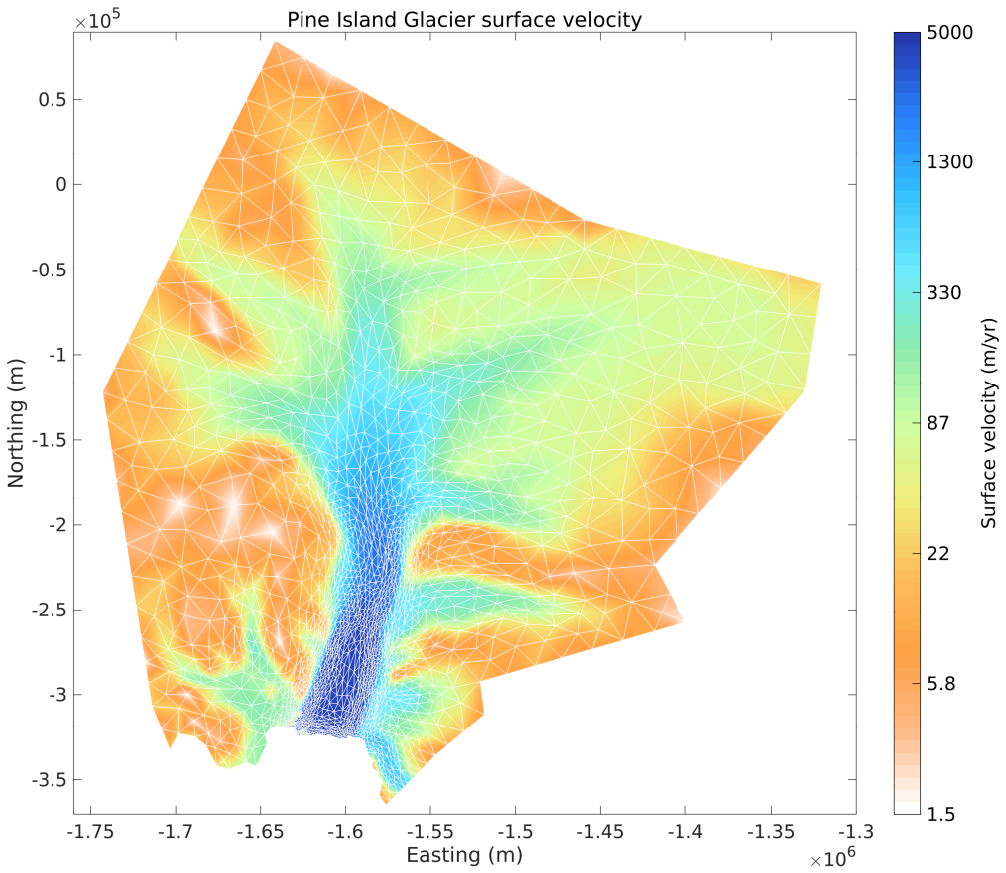

Figure A.4: Computational unstructured mesh defined over Pine Island Glacier, West Antarctica. Surface ice velocities from Mouginot et al. (2019a) are interpolated onto the mesh, and mesh element boundaries are denoted by white lines.

method of tracking the migration of the grounding line within individual mesh elements), the maximum mesh resolution needed to provide accurate estimates of grounding line dynamics is 2 km. As we are limited by computational power, it is not typically feasible to discritize an entire ice sheet domain into 2km elements, which would be necessary if a structured grid were employed. To avoid these computational limitations, many ice sheet models, including ISSM, employ the use of unstructured meshes.

In particular, ISSM relies on static anisotropic mesh adaption in order to construct the computational domain used by the ice sheet model. Here, the goal is to minimize interpolation error for a given field, which is typically the observed surface ice velocity. Smaller elements are partitioned to regions in which variations in velocity are high (e.g. in ice streams), while

large elements are defined over regions where the flow of ice is relatively homogeneous. Unlike a structured grid, in which computational resources are partitioned equally across the entire domain, dynamic regions of ice flow are prioritized in order minimize the number of elements while preserving precision (see figure A.4). The implementation of unstructured meshes within transient ice flow models allows scientists to solve the complex system of ice flow equations given in equation A2 across spatially large (continental-scale) domains; however, these static meshes are unable to adapt to the changing location and structure of a migrating grounding line. Recently, dos Santos et al. (2019) implemented adaptive mesh refinement in ISSM, which allows the static anisotropic mesh to evolve in time following migration of the grounding line (or interface of choice). While still under development and not used in this dissertation, the adaptive mesh refinement procedure is a promising next step in the development of ISSM.

A.5 Ice sheet modules

Ice sheets are not isolated systems, meaning that they are acted upon and influenced by outside forces and processes that are not taken into account in the equations of mechanical ice flow (equation A.2). In order to accurately model the dynamic evolution of an ice sheet, it is necessary to either develop parameterizations (modules) of these processes that can be implemented in standalone ice sheet models, or develop model coupling schemes to address these processes. Ice shelf basal melting rate modules were employed throughout this dissertation to translate the uptake of oceanic heat into a basal melt rate field that could be used by the ice sheet model. In addition, in chapter 4 we coupled ISSM to a dynamic ocean general circulation model to simulate ocean forcing in our ice sheet model. Aside from ocean forced processes, there exist various other ice sheet modules that address numerous outside processes, including but not limited to: iceberg calving, glacio-isostatic rebound, sea level

rise, ice sheet surface melting, subglacial hydrology, rift propagation, and sea ice processes. Many of the entries in this list comprise their own sub-fields within the ice sheet modeling community, highlighting the tremendous effort being undertaken to push advancement of these dynamic models forward.